

ZZ PRODUKTION UND SUCHE
NACH BOSONISCHEN HIGGS
ZERFÄLLEN MIT DEM DELPHI
DETEKTOR BEI LEP

Jens Rehn

Zur Erlangung des akademischen Grades eines
DOKTORS DER NATURWISSENSCHAFTEN
von der Fakultät für Physik der Universität (TH)
Karlsruhe

genehmigte

DISSERTATION

Tag der mündlichen Prüfung: *13.06.2003*

Referent: *Prof. Dr. W. de Boer*

Korreferent: *Prof. Dr. G. Quast*

Zusammenfassung in deutscher Sprache

Eine Frage, der schon die Menschen in der Antike nachgingen, beschäftigt sich mit dem Ursprung und der Zusammensetzung der Materie. Dieses zum damaligen Zeitpunkt eher philosophische Problem wird heute mit großer Systematik im Rahmen von internationalen Großprojekten unter Einsatz von viel wissenschaftlichem Personal angegangen. Ein solches Großprojekt wurde am CERN¹ in der Nähe von Genf durchgeführt: Der LEP²-Beschleuniger.

Während seiner 11-jährigen Laufzeit produzierte dieser Beschleuniger eine riesige Menge Daten, deren Auswertung parallel zur Datennahme begonnen wurde und heute noch andauert. Insgesamt wurde mit dem DELPHI-Detektor (einem der vier Detektoren bei LEP) eine integrierte Gesamtluminosität von rund 1000 pb^{-1} gesammelt. Für diese Dissertation wurden die Daten des DELPHI-Detektors aus der sogenannten LEP II-Phase (1996 – 2000) verwendet, bei der mit Schwerpunktsenergien oberhalb der Z^0 -Resonanz gearbeitet wurde. In den Jahren davor (1989 – 1995) lief die Maschine während der LEP I-Ära ausschließlich auf dem Z^0 -Pol.

Gegenstand der vorliegenden Arbeit ist zum einen die Messung des Produktionsquerschnittes der Z^0 -Paarbildung, zum anderen die Suche nach dem Higgs Boson in Kanälen mit bosonischem Higgs Zerfall. Für die Durchführung der Such-Analysen stellt der bei der Messung untersuchte Kanal einen schwer zu unterdrückenden Untergrund dar. Daher konnte die Variablenselektion und die bei der Messung gewonnene Erfahrung gewinnbringend für die Higgs Suche eingesetzt werden.

Ein weiterer Schwerpunkt dieser Dissertation besteht in der Entwicklung und eingehenden Überprüfung eines Werkzeuges zur Abschätzung systematischer Fehler bedingt durch die Energie-Rekonstruktion des Teilchenstromes durch den Detektor. Diese Unsicherheit trägt nicht unerheblich zum systematischen Gesamtfehler von Messungen und Suchen bei und wird in der Zwischenzeit auch von

¹Conseil Européenne pour la Recherche Nucléaire

²Large Electron Positron Collider

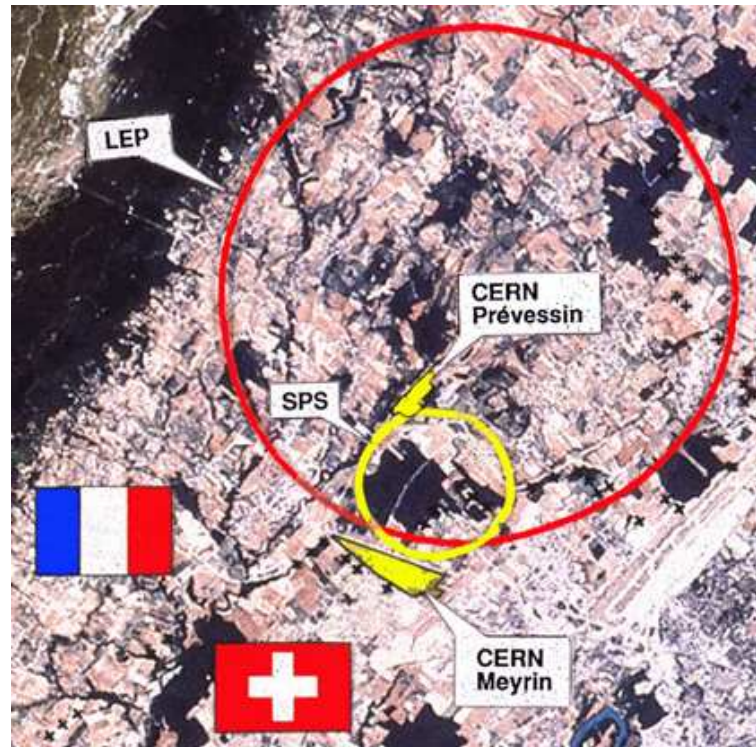


Abbildung 1: CERN und der LEP-Ring in der Nähe der französisch-schweizerischen Grenze.

einigen anderen Analysen der DELPHI-Kollaboration benutzt.

Das Standardmodell

Das Standardmodell stellt die tragende Säule unseres Verständnisses der Teilchenphysik dar und bildet den Ausgangspunkt vieler erweiterter Theorien. Seine Vorhersagen werden im Rahmen von Messungen in den verschiedensten Bereichen eingehend überprüft. Einer dieser Bereiche ist die Bestimmung des Wirkungsquerschnittes der Z^0 Paarproduktion, zu der die in dieser Arbeit durchgeführte Messung einen wichtigen Beitrag geliefert hat.

Im Standardmodell werden die Massen der Bosonen und Fermionen mit Hilfe des Higgs Mechanismus eingeführt, was zur Vorhersage eines massiven skalaren Higgs Bosons führt. Dieses Teilchen konnte bisher noch nicht experimentell nachgewiesen werden und bildet daher Grundlage und Motivation für die in dieser Arbeit durchgeführten Suchen.

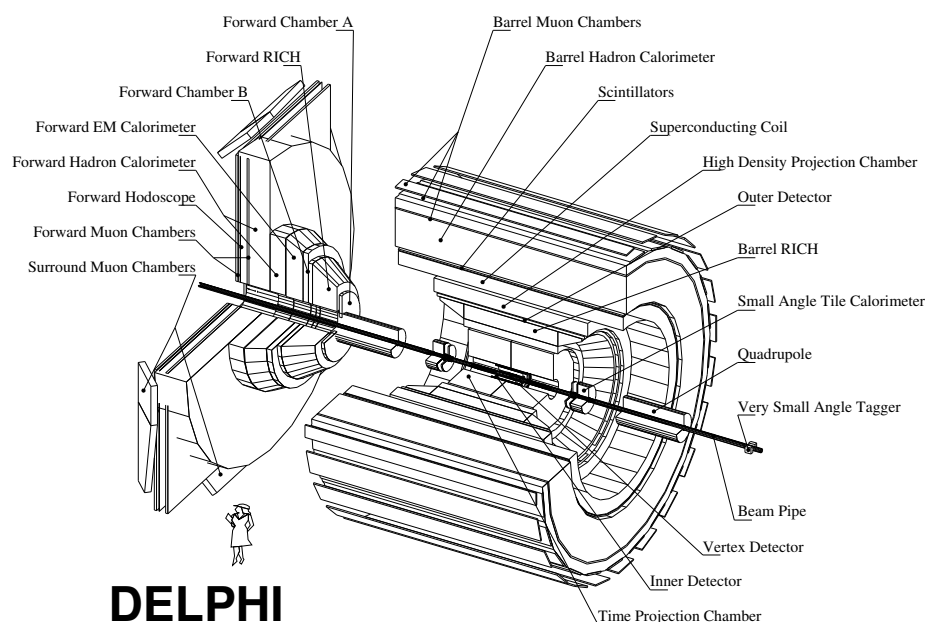


Abbildung 2: Der DELPHI-Detektor und seine Subdetektoren.

Das Experiment

In dem im Jahre 1989 erbauten LEP-Speicherring wurden Elektronen und ihre Antiteilchen, die Positronen, auf hohe Energien beschleunigt, um sie dann schließlich in einem Kollisionsprozeß paarweise zu vernichten. Dabei entstanden eine Vielzahl von neuen Teilchen, die mit Hilfe von Detektoren nachgewiesen und klassifiziert werden konnten. Der LEP-Beschleuniger besaß vier solcher Detektoren, nämlich ALEPH³, DELPHI⁴, L3⁵ und OPAL⁶. Dem LEP-Ring waren noch einige kleinere Ringe vorgeschaltet, die historischen Ursprungs sind und als Vorbeschleuniger für LEP fungierten. Mit seinen 26,7 km Gesamtumfang stellte er den größten Beschleuniger seiner Art dar. Das Tunnelsystem befindet sich zwischen 50 und 175 m tief unter der Erde. Der Tunnel selbst hat einen Durchmesser von 3,8 bis 5,5 m und erstreckt sich über die schweizerisch-französische Grenze hinweg (siehe Abbildung 1). Die Errichtung des Tunnels und des LEP-Beschleunigers dauerten zusammen 6 Jahre (1983 – 1989) und kosteten insgesamt 1,3 Milliarden Schweizer Franken, die von den damals 14 Mitgliedstaaten getragen wurden. Das noch existierende Tunnelsystem dient dem Nachfolgebeschleuniger LHC⁷ nun als

³Apparatus for **LEP** Physics

⁴**D**etector with **L**epton, **P**hoton and **H**adron **I**dentification

⁵**3**rd **L**etter of intent

⁶**O**mnipurpose **A**pparatus for **LEP**

⁷**L**arge **H**adron **C**ollider

Baugrundlage.

Der DELPHI-Detektor befand sich am Wechselwirkungspunkt 8 (Pit 8) und stand somit ungefähr 100 m unter der Erdoberfläche. Er besaß eine zylindrische Form mit einer Länge von ungefähr 8 m und einem Radius von 5 m. Das Gesamtgewicht betrug etwa 3500 t. Um Wartungen zu ermöglichen, war der gesamte Detektor auf Rollschienen gelagert. Desweiteren konnten die beiden Endkappen (wie auf Abbildung 2 zu erkennen ist) mit Hilfe der Schienen herausgefahren werden, um in den Detektormantel selbst zu gelangen. Planung und Bau dieses Detektors haben sieben Jahre in Anspruch genommen.

Von den Leistungsdaten her zeichnete sich dieser Detektor durch seine gute Vertexrekonstruktion und eine ausgefeilte Teilchenidentifikation aus. Die möglichst vollständige Abdeckung des gesamten Raumwinkelbereiches stand bei der Konstruktion ebenfalls im Vordergrund und konnte auch gut realisiert werden.

Die Simulation von Ereignissen

Um die mit Hilfe des Detektors gesammelten Daten auf ihre Verträglichkeit mit den gültigen Modellvorstellungen zu untersuchen, werden die vom Modell her erwarteten Ereignisse durch Monte-Carlo⁸ Programme simuliert. Dabei unterscheidet man zwischen Untergrund- und Signal-Simulationen. Die Untergrund-Simulationen berücksichtigt (im Idealfall) alle bekannten Nicht-Signalprozesse und deren Korrekturen, die eine dem Signal ähnliche Signatur aufweisen. Zusammen mit der Signal-Simulation soll ein Eindruck darüber ermöglicht werden, in wie weit sich die untersuchte Ereignis Topologie vom Untergrund abhebt.

Die Prozesse mit der größten Bedeutung für die im Rahmen dieser Arbeit durchgeführten Analysen sollen an dieser Stelle kurz vorgestellt werden. Eine Übersicht über die entsprechenden Wirkungsquerschnitte der einzelnen Reaktionen bietet Abbildung 3.

- $e^+e^- \rightarrow Z^0/\gamma \rightarrow f\bar{f}$: Prozeß mit 2 Fermionen im Endzustand, sowie einem hochenergetischen Photon
- $e^+e^- \rightarrow ZZ$: Paarbildung von Z^0 Bosonen mit anschließendem Zerfall zu vier Fermionen. Signal-Prozeß für die Messung des NC02-Wirkungsquerschnittes und gleichzeitig schwer zu unterdrückender Untergrund bei der Higgs Suche.
- $e^+e^- \rightarrow WW$: Paarbildung von W^\pm -Bosonen mit anschließendem Zerfall zu

⁸zusammenfassender Begriff für durch Zufallsgeneratoren erzeugte Ereignisse

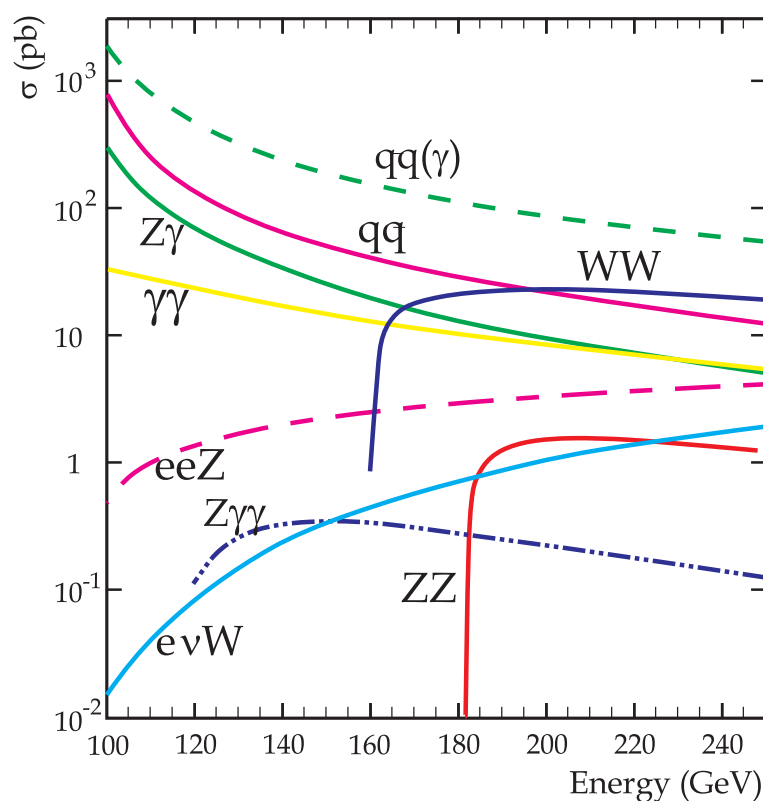


Abbildung 3: Darstellung der wichtigsten Prozesse resultierend aus der Annihilation von Elektronen und Positronen. Gezeigt ist die Abhängigkeit des jeweiligen Wirkungsquerschnittes von der verwendeten Schwerpunktsenergie.

vier Fermionen. Bedeutender Untergrund für Suchen und Messung aufgrund der Topologie und des recht hohen Wirkungsquerschnittes.

- $e^+e^- \rightarrow W e \nu$: t-Kanal-Prozeß mit hochenergetischem Elektron, das unter sehr geringem Winkel zum Strahlrohr abgestrahlt wird.

Um zusätzliche statistische Unsicherheiten aufgrund der verwendeten Simulationen zu vermeiden, wurde mindestens die 100-fache Statistik verglichen mit der Zahl der erwarteten Ereignisse generiert.

Die Analyse-Werkzeuge

Um einzelne Ereignisse mit Signaltopologie aus einem Meer von Untergrundprozessen herauszuselektieren bedarf es ausgefeilter statistischer Werkzeuge und Methoden.

Im Rahmen dieser Arbeit fand ein iteriertes nichtlineares Diskriminanzverfahren (IDA) Anwendung, bei dem aus einem Satz von neun bzw. zwölf selektierten Eingabevariablen eine quadratische Teststatistik konstruiert wurde. Das Kriterium für die Teststatistik ist definiert durch eine möglichst große Separierung von Signal und Untergrund bei gleichzeitiger Minimierung der Varianzen beider Verteilungen in dem von den Eingabevariablen aufgespannten neun bzw. zwölf dimensional Raum. Dies führt auf ein Eigenwertproblem, dessen Lösung die Teststatistik definiert. Nach einem Schnitt auf die so erhaltene Teststatistik wird der Vorgang einmal iteriert, um eine Reoptimierung der Untergrunddiskriminierung zu erreichen. Dieses Verfahren wurde sowohl für die Higgs Suchen, als auch für die Messung des Wirkungsquerschnittes resonanter Z^0 Paare verwendet.

Um eine Aussage über den Wirkungsquerschnitt treffen zu können, wurde das Signal–Monte–Carlo mit Hilfe eines sog. „Maximum Likelihood Fits“ an die Daten gefittet. Dabei wird von einer Poisson–Verteilung der Daten um die simulierte Erwartung ausgegangen, um die Likelihood–Funktion zu bestimmen. Durch Logarithmierung und anschließender Aufsummierung der Poissonfunktionen eines jeden „bins“ der IDA–Verteilung erhält man schließlich den Logarithmus der Likelihood–Funktion:

$$\ln[\mathcal{L}(x)] = \sum_{bins} [d \ln(m(x)) - m(x)] \quad (1)$$

In obiger Funktion 1 repräsentiert d die Daten–Ereignisse und m die Anzahl Ereignisse aus den Monte–Carlo Simulationen (Signal + Untergrund) in Abhängigkeit des zu bestimmenden Faktors x . Aus der Ermittlung des Extremwertes dieser Funktion resultiert der gemessenen Wirkungsquerschnitt und kann mit der Standard Modell Erwartung verglichen werden.

Bestimmung des systematischen Fehlers: Das Shaking–Verfahren

Ziel dieser Methode ist es, eine Abschätzung für den systematischen Fehler bei LEP II–Analysen bereitzustellen. Dabei konzentriert sich die Aussagekraft primär auf systematische Unsicherheiten, die aus der Ereignisrekonstruktion und der Simulation des Energieflusses durch den Detektor resultieren. Es hat sich gezeigt, daß gerade bei Analysen mit energiereichen Neutrinos im Endzustand, und damit mit einer signifikanten Menge an fehlender Energie, die Ereignisrekonstruktion eine nicht zu unterschätzende Quelle systematischer Unsicherheiten darstellt. Das Verfahren macht sich die Kalibrationsläufe auf dem Z^0 –Pol zunutze, die während der LEP II–Phase in regelmäßigen Abständen durchgeführt wurden. Aus den Diskrepanzen zwischen Simulation und genommenen Daten bezüglich der neutralen und geladenen Multiplizitäten konnten in Abhängigkeit von Impuls und

Raumwinkel Korrekturfaktoren bestimmt werden. Da die Multiplizitäten und damit auch die Korrekturfaktoren nur unwesentlich von der Schwerpunktsenergie abhängen, wurden mit deren Hilfe modifizierte LEP II-Simulationen generiert. Eingehende Tests haben gezeigt, daß der bei Verwendung dieser modifizierten Simulationen auftretende Einfluß auf das Endergebnis als Unsicherheitsband interpretiert werden kann.

Aus diesem Band wurde der systematische Fehler bedingt durch die Ereignisrekonstruktion für alle im Rahmen dieser Arbeit durchgeführten Analysen abgeleitet. Zusätzlich wurde durch umfangreiche Tests sichergestellt, daß die Interpretationen und Schlußfolgerungen aus diesem Verfahren in sich konsistent und nicht nur auf die hier vorgestellten Analysen anwendbar sind.

Messung des Wirkungsquerschnittes resonanter Z^0 -Paar-Produktion

Um den Wirkungsquerschnitt bei $e^+e^- \rightarrow ZZ$ zu bestimmen, stehen verschiedene Zerfallskanäle zur Verfügung. Bei dem im Rahmen dieser Arbeit untersuchten Kanal handelt es sich um $ZZ \rightarrow q\bar{q}\nu\bar{\nu}$. Hierbei zerfällt das eine Z^0 -Boson hadronisch und das zweite unsichtbar in zwei Neutrinos. Somit ergibt sich als typische Signatur eine mit dem Z^0 kompatible sichtbare sowie unsichtbare invariante Masse. Das Verzweigungsverhältnis beträgt in diesem Fall 28 % und stellt somit den zweit-wichtigsten Zerfallskanal der Z -Paare dar.

Der Wirkungsquerschnitt wird mit Hilfe der Analyse als Abweichung zum Standardmodell-Wert bestimmt. Hierfür werden die bei LEP II in den Jahren zwischen 1997 und 2000 gesammelten Daten bei Schwerpunktsenergien zwischen 183 GeV und 208 GeV analysiert.

Nach einer Vorselektion durch sequentielle Schnitte auf ausgesuchte Variablen, wurde mit Hilfe einer iterierten nichtlinearen Diskriminanz-Analyse (IDA) die zu messenden Signal-Ereignisse herauspräpariert. Die bei der Diskriminanz-Analyse verwendete Teststatistik ermöglichte eine optimale Diskriminierung von Untergrundereignissen und wurde benutzt, um mit Hilfe eines Maximum-Likelihood-Fits der Standardmodell Erwartung an die gemessenen Daten den Wirkungsquerschnitt zu bestimmen.

Abbildung 4 zeigt die bei unterschiedlichen Schwerpunktsenergien gemessenen Wirkungsquerschnitte, sowie auch den theoretisch vom Standardmodell her erwarteten Verlauf. Die Messung folgt der theoretischen Kurve innerhalb einer Standardabweichung und scheint diese zu bestätigen. Kombiniert man die Ergebnisse aller Energien (von 183 GeV bis 208 GeV), so findet man **173** Ereignisse in den Daten, bei einer simulierten Erwartung von **106,7** Untergrundereignissen, so-

ZZ to $q\bar{q}\nu\bar{\nu}$

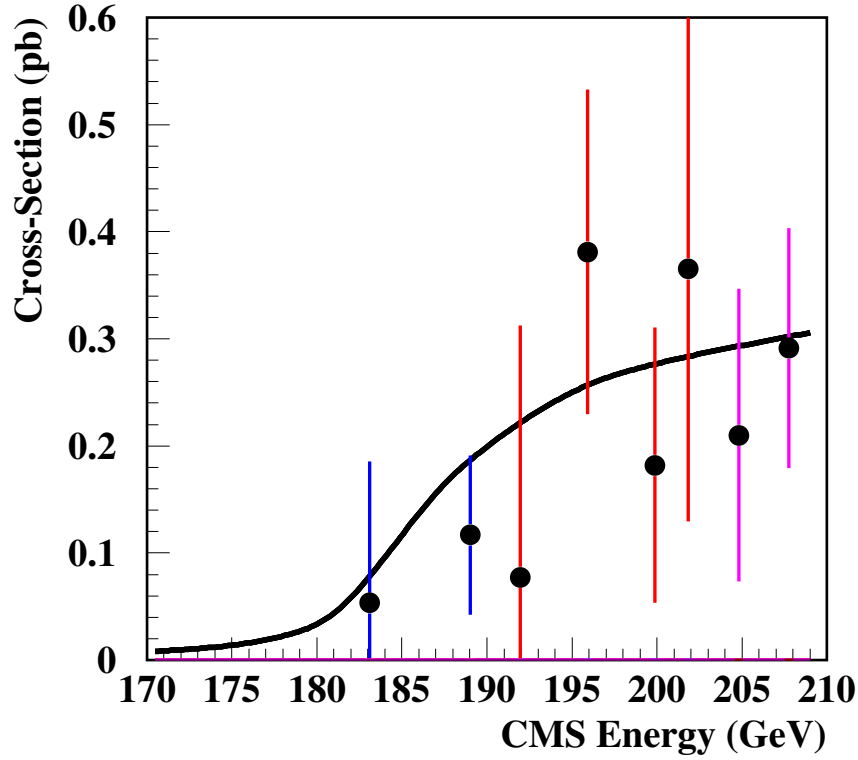


Abbildung 4: Die resultierenden Wirkungsquerschnitte des Kanals $ZZ \rightarrow q\bar{q}\nu\bar{\nu}$ pro untersuchter Schwerpunktsenergie. Die schwarze Linie kennzeichnet den vom Standardmodell erwarteten Verlauf.

wie **66.3** Signalereignissen. Der aus dem Maximum-Likelihood-Fit resultierende kombinierte Wirkungsquerschnitt ergibt

$$0,78 \pm 0,15 \text{ (stat.)} \pm 0,05 \text{ (syst.)} * \sigma_{\text{SM}}$$

bezogen auf den Standardmodell-Wirkungsquerschnitt. Dieses Ergebnis liegt $1,4\sigma$ unter dem erwarteten Wert und ist somit innerhalb statistischer und systematischer Unsicherheiten kompatibel mit dem Standardmodell.

Suche nach bosonischen Higgs Zerfällen

Dieser Teil der Arbeit beschäftigt sich mit der Suche nach bosonisch zerfallenden Higgs Bosonen nach W^+W^- , das heißt $e^+e^- \rightarrow ZH \rightarrow ZWW$. Dabei wurde

in zwei Kanälen mit unterschiedlicher Signaltopologie gesucht. Derartige Zerfälle sind in mehrerlei Hinsicht interessant. Zum einen ermöglichen sie es, die fundamentalste aller Higgs Kopplungen zu untersuchen: die Kopplung an massive Bosonen. Zum anderen ist ein solcher Zerfall sowohl im Standardmodell als auch in erweiterten Modellen, wie dem 2-Higgs-Dublett-Modell (Typ I) möglich. Gerade letzteres würde ein Verzweigungsverhältnis von etwa 90 % für $H \rightarrow W^+W^-$ aufweisen und die hier untersuchten bosonischen Zerfallskanäle wären somit bevorzugt.

Diese Analyse untersuchte DELPHI Daten aus den Jahren 1999 und 2000 bei Schwerpunktsenergien von 196 GeV bis 208 GeV, da nur bei diesen hohen Energien ein genügend großer Wirkungsquerschnitt bosonischer Higgs Zerfälle zu erwarten ist. Die verwendeten Daten entsprechen einer integrierten Luminosität von $408,9 \text{ pb}^{-1}$.

Dieser Arbeit konzentriert sich auf Kanäle, bei denen das Z^0 -Boson sowie eines der beiden W^\pm -Bosonen hadronisch zerfallen das zweite W^\pm -Boson allerdings in ein Elektron oder Muon zusammen mit dem entsprechenden Neutrino übergeht. Dabei schreibt die Kinematik vor, daß eines der Bosonen stark virtuell sein muß, was zu einer invarianten Masse von ungefähr 30 GeV führt. Daher kann man zwei Fälle unterscheiden:

- das stark virtuelle Boson zerfällt hadronisch $ZH \rightarrow ZWW \rightarrow q\bar{q}l\nu(q\bar{q})^*$
- das stark virtuelle Boson zerfällt leptonisch $ZH \rightarrow ZWW \rightarrow q\bar{q}q\bar{q}(l\nu)^*$

Beiden Fällen wurde in Form von separaten Analysen Rechnung getragen.

Kanal: $ZH \rightarrow ZWW \rightarrow q\bar{q}l\nu(q\bar{q})^*$

Dieser Kanal zeichnet sich durch zwei hochenergetische Jets, zwei sehr weiche Jets sowie ein energiereiches Lepton begleitet von fehlender Energie und fehlendem Impuls aus. Die Kombination aller verwendeter Schwerpunktsenergien führte bei einer Effizienz von 40 % zu

22 gefundenen Ereignissen in den Daten, sowie **19,44** erwarteten Untergrundereignissen.

Auffällig sind dabei besonders zwei sehr signalartige Ereignisse, die beide aufgrund eingehender Untersuchung als Beitrag von Standardmodell-Prozessen mit 6-Fermionen im Endzustand klassifiziert wurden. Für diese Prozesse standen keine Simulationen zur Verfügung, so daß lediglich eine Abschätzung der erwarteten Ereigniszahl mit Hilfe des erst kürzlich entwickelten Generators LUSIFER[DR02] durchgeführt werden konnte. Dieser sagt **2,4** Standardmodell Ereignisse in diesem Kanal vorher.

Kanal: $ZH \rightarrow ZWW \rightarrow q\bar{q}q\bar{q}(l\nu)^*$

Der zweite untersuchte Kanal bosonisch zerfallender Higgs Bosonen hat eine typische Vier-Jet Signatur mit einem niederenergetischen geladenen Lepton sowie etwas fehlender Energie und Impuls. Sowohl das geladene Lepton als auch die fehlende Energie sind allerdings aufgrund ihres niederenergetischen Charakters nur schwer von Untergrundprozessen mit vier Jets im Endzustand zu unterscheiden. Die entsprechende Kombination aller Energien ergab in diesem Fall bei einer Effizienz von 40 %

42 gefundene Ereignisse in den Daten, sowie **42,89** erwartete Untergrundereignisse.

Dieses Ergebnis bescheinigt eine sehr gute Übereinstimmung zwischen Standardmodell-Vorhersage und Daten. Erwartungsgemäß fiel die Sensitivität in diesem Kanal etwas niedriger verglichen mit dem anderen Kanal aus, was sich in der höheren Zahl an Untergrundereignissen bei gleicher Effizienz widerspiegelt.

Beide Suchanalysen wurden schließlich verwendet, um zusammen mit zwei weiteren Analysen eine kombinierte Ausschlußgrenzen für die Higgs Masse und den Wirkungsquerschnitt zu ermitteln. Die beiden zusätzlichen Analysen ergänzen dabei die von dieser Dissertation abgedeckten Higgs Zerfallskanäle um Zerfälle mit

- vollständig hadronische Endzustände $Z^0 H \rightarrow Z^0 W^+ W^- \rightarrow q\bar{q}q\bar{q}q\bar{q}$ von *Marcel Stanitzki*[Sta03], sowie
- vier hadronische Jets und fehlende Energie $Z^0 H \rightarrow Z^0 W^+ W^- \rightarrow \nu\bar{\nu}q\bar{q}q\bar{q}$ von *Jörgen Dalmau*[Dal03].

Aus der Kombination resultierte eine erwartete Ausschlußgrenze von **101,7 GeV** auf die Higgs Masse unter der Annahme eines Standard Modell Wirkungsquerschnittes, sowie einer 100 % Verzweigung von $H \rightarrow W^+ W^-$. Aufgrund eines leichten Datenüberschusses in der Analyse mit vier hadronischen Jets und fehlender Energie, konnte allerdings **keine** beobachtete Ausschlußgrenze bestimmt werden.

IEKP-KA/2003-15

ZZ PRODUCTION AND SEARCHES FOR
BOSONIC HIGGS DECAYS WITH THE
DELPHI DETECTOR AT LEP

Jens Rehn

Zur Erlangung des akademischen Grades eines
DOKTORS DER NATURWISSENSCHAFTEN
von der Fakultät für Physik der Universität (TH)
Karlsruhe

genehmigte

DISSERTATION

Tag der mündlichen Prüfung: *13.06.2003*

Referent: *Prof. Dr. W. de Boer*

Korreferent: *Prof. Dr. G. Quast*

Contents

1	Introduction	1
2	The Standard Model	5
2.1	The gauge principle	6
2.2	The strong interaction	8
2.3	The weak interaction	9
2.4	The running coupling constants	13
2.5	The Higgs mechanism in the standard model	15
2.5.1	Giving mass to W^\pm and Z^0 bosons	17
2.5.2	Giving mass to fermions	18
3	The experiment	21
3.1	The LEP accelerator	21
3.2	The DELPHI detector	25
3.2.1	The tracking system	27
3.2.2	Calorimetric detectors	30
3.2.3	Particle identification	30
3.2.4	The offline system	32
4	Event simulation using Monte Carlo generators	35
4.1	Simulation of two-fermion processes	36
4.1.1	$e^+e^- \rightarrow q\bar{q}$ (phase I)	37
4.1.2	Building of final partons (phase II)	38
4.1.3	Hadronisation (phase III)	44
4.1.4	Decay of unstable hadrons (phase IV)	47

4.2	Simulation of four-fermion processes	48
4.2.1	$e^+e^- \rightarrow Z^0 Z^0$	49
4.2.2	$e^+e^- \rightarrow W^+W^-$	49
4.2.3	$e^+e^- \rightarrow We\nu$	49
4.3	Simulation of two-photon and Bhabha processes	49
4.4	Detector simulation	51
5	Analysis tools and techniques	53
5.1	Jet clustering	53
5.1.1	LUCLUS	54
5.1.2	JADE	54
5.1.3	DURHAM	55
5.2	Discriminant analyses techniques	55
5.2.1	Fisher discriminant analysis	56
5.2.2	Non-linear and Iterated Discriminant Analyses	58
5.3	Artificial neural networks	60
5.4	Binned maximum Likelihood fit	62
5.5	Kinematic fits with constraints	65
6	Systematic errors: the shaking technique	67
6.1	The reweighting technique	68
6.1.1	Determination of weight factors	68
6.1.2	Application of the weight factors	70
6.2	Applications for the shaking method	73
6.2.1	Cross-checks by shaking 91 GeV MC samples	73
6.2.2	Checks using LEP II samples	75
6.2.3	Conclusions	81
6.3	Scaling and boosting technique	81
6.3.1	Analysis with invisible Higgs decays at 207 GeV	83
6.3.2	Analysis with $Z \rightarrow \nu\bar{\nu}$ and $h \rightarrow b\bar{b}$ at 207 GeV	83
6.3.3	$ZZ \rightarrow q\bar{q}\nu\bar{\nu}$ at 183 GeV	84
6.3.4	$ZZ \rightarrow q\bar{q}\nu\bar{\nu}$ at 207 GeV	84

6.3.5	Conclusion	84
6.4	Interpretation and outlook	84
7	Cross-section measurement of doubly resonant Z^0 pairs	91
7.1	Data and simulation samples	92
7.2	Track selection and pre-selection	94
7.2.1	Data quality cuts	94
7.2.2	Anti-two-photon and anti-Bhabha cuts	95
7.2.3	Anti-two-fermion and anti- WW cuts	96
7.3	Selection variables and tail cuts	97
7.4	The iterated discriminant analysis	99
7.5	Systematic errors and working point	101
7.6	The resulting cross-sections	103
8	Search for bosonic Higgs decays	107
8.1	Signal topologies	109
8.2	Data and simulation samples	110
8.3	Track selection and pre-selection	111
8.3.1	Anti-two-fermion and anti-four-fermion cuts	111
8.4	Channel with on-shell W decaying leptonically	112
8.4.1	Selection variables	113
8.4.2	Iterated discriminant analysis	113
8.5	Channel with off-shell W decaying leptonically	117
8.5.1	Selection variables	117
8.5.2	Iterated discriminant analysis	119
8.6	Systematic errors	120
8.6.1	Luminosity	120
8.6.2	Simulation cross-sections	120
8.6.3	Description of gluon radiation at parton level	120
8.6.4	Energy flow reconstruction	121
8.7	Results overview	121
8.8	Confidence limits on bosonic Higgs decays	122

8.8.1	Limits on the Higgs mass	126
8.8.2	Cross-section limits	128
9	Summary and outlook	133
9.1	Cross-section measurement of doubly resonant Z^0 pairs	133
9.2	Search for bosonic Higgs decays	134
9.2.1	Channel with on-shell W decaying leptonically	134
9.2.2	Channel with off-shell W decaying leptonically	134
	Bibliography	137
A	Performance plots ZZ cross-section analysis	141
	Acknowledgements	147

List of Figures

2.1	The gluon interactions	9
2.2	The coupling triangle	11
2.3	Running coupling constants	13
2.4	Screening of an electric charge	14
2.5	The Higgs potential	16
3.1	Map of CERN and LEP	22
3.2	The acceleration steps of LEP	23
3.3	The cross-section at Z^0 energy	24
3.4	Integrated luminosity	25
3.5	The DELPHI detector	26
3.6	The vertex detector	27
3.7	The time projection chamber	29
3.8	The RICH principle	31
3.9	Data processing	33
4.1	Cross-section overview	36
4.2	Steps of Monte Carlo modelling	37
4.3	Partonisation: ME method	41
4.4	Partonisation: colour dipole method	43
4.5	String fragmentation	45
4.6	Fragmentation functions	46
4.7	four-fermion diagrams	48
4.8	Bhabha and di-photon diagrams	50

5.1	Discrimination techniques	58
5.2	Iterated discriminant analysis	59
5.3	Typical artificial neural net topologies	61
5.4	Sample Likelihood distribution	64
6.1	Shaking: multiplicity mean values	71
6.2	Shaking: correction coefficients	72
6.3	Shaking effect on multiplicities at 91 GeV	74
6.4	Shaking effect on variable distributions at 91 GeV	75
6.5	Shaking effect on multiplicities at LEP II energies	76
6.6	Shaking effect on variable distributions at LEP II energies	78
6.7	Shaking effect on final discriminant variables	80
6.8	Shaking: performance plot invisible Higgs analysis	86
6.9	Shaking: performance plot Higgs analysis with invisible Z^0 decay	87
6.10	Shaking: performance plot ZZ analysis at 183 GeV	88
6.11	Shaking: performance plot ZZ analysis at 207 GeV	89
7.1	$ZZ \rightarrow q\bar{q}\nu\bar{\nu}$ topology	91
7.2	NC02 Feynman graphs	93
7.3	Matrix element ratio	95
7.4	ZZ: input variables at 189 GeV	99
7.5	ZZ: IDA output distributions	100
7.6	Overview of statistical and systematic errors for ZZ analysis	102
7.7	$ZZ \rightarrow q\bar{q}\nu\bar{\nu}$ cross-sections	104
7.8	Overview of NC02 cross-section results	105
8.1	$ZWW \rightarrow q\bar{q}q\bar{q}l\bar{\nu}$ topology	107
8.2	SM Higgs production process	108
8.3	Higgs branching ratio	109
8.4	ZWW: input variables combining 196 – 207 GeV (on-shell)	114
8.5	ZWW: IDA and Higgs mass distributions (on-shell)	115
8.6	ZWW: examples of 6-fermion final state processes	116
8.7	ZWW: input variables combining 196 – 207 GeV (off-shell)	118

8.8	ZWW : IDA and Higgs mass distributions (off-shell)	119
8.9	ZWW : combined limit	125
8.10	ZWW : combined CL_b	127
8.11	ZWW : expected CL_s per channel	128
8.12	ZWW : cross-section limits	129
8.13	ZWW : First highly significant candidate	130
8.14	ZWW : Second highly significant candidate	131
A.1	performance plot at 183 GeV and 186 GeV	142
A.2	performance plot at 192 GeV and 196 GeV	143
A.3	performance plot at 200 GeV and 202 GeV	144
A.4	performance plot at 205 GeV and 207 GeV	145
A.5	performance plot at 207 GeV during the period with partially damaged main tracking chamber (S6)	146

List of Tables

2.1	The three main interactions	5
2.2	The fermions, an overview	6
4.1	Branching ratio of Z^0 -bosons	36
6.1	Shaking: mean correction coefficients per year	70
6.2	Shaking: expected background for ZZ analysis	77
6.3	Radiative return contributions to two-fermion final state processes	81
7.1	Overview of the possible ZZ decay channels and their correspond- ing branching ratios. Here ll denotes electrons and muons only. . .	92
7.2	Systematic uncertainties for ZZ analysis	101
7.3	$ZZ \rightarrow q\bar{q}\nu\bar{\nu}$ results overview	103
8.1	ZWW: background suppression at preselection level	112
8.2	ZWW: summary of results	122

Chapter 1

Introduction

For more than 2000 years mankind has been searching for answers to the fundamental questions which arise from studying nature. One of the most puzzling riddles among these is the question of the origin and composition of matter. What initially started as a philosophical problem in ancient Greece, has today resulted in a wide spectrum of scientific research programs involving huge experiments and a lot of manpower.

One of the biggest research centers in Europe is CERN¹. Here a vast variety of accelerator-related research projects are dealt with, among which the LEP² accelerator with its four experiments was the biggest project. During its 11 years of operation (from 1989 until 2000) a huge amount of data was accumulated, leaving a legacy which will take several years to fully analyse and exploit relevant physics.

Basically one can distinguish two main streams of analyses performed with this data: the searches for new particles or phenomena and the measurements of particle properties and their compatibility with a theoretical model. Currently, the so-called “Standard Model” is the main reference model, that all results in high energy physics are compared with. It is more the result of combining Quantum Electro Dynamics, Quantum Chromo Dynamics and the electroweak theory of Glashow[Gla61], Salam[Sva68] and Weinberg[Wei67] than a theory on its own. One particle predicted by this model could not be found up to now: the so-called “Higgs boson”. This particle plays a very important role, since it provides an explanation for the origin of mass, one of the fundamental questions in physics. Hence most search analyses focus on this missing piece in nature’s puzzle. Apart from the Standard Model several extended models exist, which also predict at least one Higgs boson. Among these, the so-called MSSM³ is one

¹Conseil Européenne pour la Recherche Nucléaire

²Large Electron Positron collider

³Minimal Supersymmetric Standard Model

of the most favoured within the community.

One important issue of the work presented in this thesis deals with a measurement of the production cross-section of doubly resonant Z^0 pairs. The Z^0 and W^\pm bosons are mediators of the electroweak force and were discovered at CERN in 1983. A precise measurement of their cross-sections is used to cross-check the standard model predictions and can give a clue to new physics beyond. Since the Z^0 pair production is one of the main background processes when searching for the Higgs boson, these analyses can also benefit from the development of tools to select these processes with high efficiency.

In this context, the sensitivity of the analysis to uncertainties in the energy reconstruction of the detector was studied. Since this measurement has to deal with particles escaping detection, it is relying heavily on the energy measured with the detector. Consequently it is vital to determine a proper estimator for this source of systematic error. For this task, a special tool was developed, which will be presented in detail: the shaking technique.

The second analysis performed and described in this thesis focuses on a Higgs search. The analysis was optimised to be sensitive to a Higgs boson decaying into a pair of W bosons. This decay probes the most fundamental processes of the Higgs mechanism: its coupling to bosons. Since the branching fraction of the Standard Model Higgs boson to bosonic final states is expected to be very low at present energies, it was essential to achieve a high signal sensitivity by exploiting modern statistical techniques.

This thesis begins with an introduction to the Standard Model in chapter 2, focusing on the elements important to understand the motivations for the analyses performed. It provides an overview only and should be regarded as such. The following part deals with the e^+e^- particle accelerator and the detector used to record the data analysed. The most important parts of the DELPHI detector are introduced along with a description of purpose and function principle. Since Monte Carlo simulations were used to identify and extract relevant physics from data, chapter 4 provides an overview of the typical event topologies and the Monte Carlo packages used to simulate them. In addition, the different simulation steps are explained together with the underlying models. Chapter 5 focuses on the description of analyses methods and tools which help to identify and extract the relevant processes.

The development and cross-checking of the "shaking" tool is described in detail in chapter 6. It provided useful estimates for the systematic uncertainties encountered in search and measurement. The latter is covered by chapter 7, which deals with the extraction of the cross-section for resonant Z^0 pair production. The second analysis, searching for bosonic Higgs decays for two different decay channels, is described in chapter 8 along with the extraction of limits on Higgs mass and cross-section. Final conclusions and a summary can be found in

chapter 9.

Chapter 2

The Standard Model

This chapter is meant as an introduction only. Its purpose is to provide the theoretical background necessary to understand the work presented in this thesis. However it cannot cover this topic to its full extend. For further details, please refer to common literature[Sch95, Gri87].

The theoretical models which try to approximately describe the processes and interactions in nature, categorize all elementary particles in two classes: fermions and bosons. Both classes are characterised by their spin. Fermions carry spin $n+\frac{1}{2}$ with n being a positive integer including zero. Basically all matter surrounding us is made up of fermions. Bosons have an integer spin and mediate one of the three fundamental forces described by the Standard Model, which interacting with fermions (see table 2.1).

Today we know of 4 different fundamental interactions: the strong and the weak interaction, electromagnetism and gravitation. For the first three of these forces, there exists a renormalizable theory. But not for the last one. Since gravitation is the weakest of all four forces, it does not play an important role in particle physics because of the small masses involved. Hence it will not be considered any further. The standard model describes the strong interaction using

interaction	boson	el. charge	mass (GeV)
el. magn.	photon	0	0
weak interaction	Z^0	0	91.2
	W^\pm	± 1	80.4
strong interaction	gluon	0	0

Table 2.1: Interactions in the standard model and their mediators.

	family			weak isospin	el. charge	weak hypercharge
	1.	2.	3.			
quarks	$\begin{pmatrix} u \\ d' \end{pmatrix}_L$	$\begin{pmatrix} c \\ s' \end{pmatrix}_L$	$\begin{pmatrix} t \\ b' \end{pmatrix}_L$	$\begin{pmatrix} +\frac{1}{2} \\ -\frac{1}{2} \end{pmatrix}$	$\begin{pmatrix} +\frac{2}{3} \\ -\frac{1}{3} \end{pmatrix}$	$+\frac{1}{3}$
	u_R d_R	c_R s_R	t_R b_R	0 0	$+\frac{2}{3}$ $-\frac{1}{3}$	$+\frac{4}{3}$ $-\frac{2}{3}$
leptons	$\begin{pmatrix} e \\ \nu_e \end{pmatrix}_L$	$\begin{pmatrix} \mu \\ \nu_\mu \end{pmatrix}_L$	$\begin{pmatrix} \tau \\ \nu_\tau \end{pmatrix}_L$	$\begin{pmatrix} -\frac{1}{2} \\ +\frac{1}{2} \end{pmatrix}$	$\begin{pmatrix} -1 \\ 0 \end{pmatrix}$	-1
	e_R	μ_R	τ_R	0	-1	-2

Table 2.2: Fermions and their characteristic properties.

QCD¹ and the weak interaction as part of a unification with electromagnetism (the electroweak theory by Glashow, Salam and Weinberg).

Within the class of fermions there exists another subdivision which groups together particles of similar characteristics and behavior. Each of these families contains a pair of quarks and leptons. Table 2.2 gives an overview of all fermions and some of their characteristic properties. Along with the electric charge the weak isospin is given, which groups together fermions participating in the weak interaction to lefthanded doublets (denoted by $()_L$) with weak isospin $\pm\frac{1}{2}$. The other fermions form righthanded singlets with weak isospin 0.

2.1 The gauge principle

One of the main concepts of the standard model is local gauge invariance. This requires the wave-function to be invariant under a local phase transition. Such a local phase transition depends on space and time, whereas a global phase transition does not. In QED² such a transformation has the following form:

$$\Psi' = e^{iq\chi(x)}\Psi; \quad x = (t, \vec{x}) \quad (2.1)$$

¹Quantum ChromoDynamics

²Quantum ElectroDynamics

Applying this to the Dirac equation for a particle in vacuum

$$(i\gamma^\mu \partial_\mu - m)\Psi(x) = 0 \quad (2.2)$$

yields the Dirac equation for a particle in an electromagnetic field with A'_μ being the negative gradient of the scalar function $\chi(x)$. The four-vector A'_μ is thus representing the photon field:

$$(i\gamma^\mu \partial_\mu - m)\Psi'(x) = q\gamma^\mu A'_\mu \Psi'(x) \quad (2.3)$$

This expression is not equivalent to equation 2.2 and therefore the Dirac equation is not invariant under a local phase transition. On the other hand, if a phase transition causes the change of an electromagnetic field, a change of an electromagnetic field should consequently lead to a transition in phase (Aharonov-Bohm effect). This effect was indeed observed by Möllensted and Bayh in 1962[MB62].

In order to achieve an invariance under local phase transition one has to replace the derivative ∂_μ by a covariant derivative D_μ :

$$D_\mu = \partial_\mu + iqA_\mu \quad (2.4)$$

As a consequence, the definition of vector potential A'_μ changes to:

$$A'_\mu = A_\mu - \partial_\mu \chi(x) \quad (2.5)$$

Expressing the Dirac equation 2.2 using the covariant derivative D_μ yields a modified Dirac equation, which now is invariant under local phase transition:

$$(i\gamma^\mu D_\mu - m)\Psi(x) = 0 \Leftrightarrow (i\gamma^\mu \partial_\mu - m)\Psi(x) = q\gamma^\mu A_\mu \Psi(x) \quad (2.6)$$

Since we studied QED in this example, vector field A_μ was massless. It is hence possible to achieve local phase invariance for a massless vector field. The question is, what happens for massive vector fields ?

Vector fields with spin 1 are described by the Proca equation. If a massive vector field is assumed, a corresponding mass term enters and the equation reads:

$$(\square + M^2)S_\mu - \partial_\mu \partial^\nu S_\nu = j_\mu \quad (2.7)$$

By applying expression 2.5 this Proca equation is not invariant under local gauge transition. This is an example for the fact, that local gauge invariance does not exist for massive vector fields. As will be shown in chapter 2.5, one can conserve gauge invariance by using spontaneous symmetry breaking, which creates an effective mass for those vector fields.

2.2 The strong interaction

The strong interaction is described by **Q**uantum **C**hromo **D**ynamics (QCD). In this theory the charge has three possible states in contrast to an electrical charge with only two. Since the superposition of all three charge states together yield a neutral state, one has chosen the colours red, green and blue as representations of the states. The mediators for this interaction (the gluons) carry colour charge themselves and can hence also interact with each other.

In QCD the Lagrangian for a free quark can be expressed in the following form:

$$\mathcal{L} = \bar{q}_j(i\gamma^\mu\partial_\mu - m)q_j \quad (2.8)$$

Here q_j (with $j = 1, 2, 3$) represent the three quark colour fields. This Lagrangian has to be invariant under the non-abelian local gauge transformation $SU(3)$, which has the following structure:

$$q_j(x) \rightarrow e^{\alpha^a(x)T_a}q_j(x) \quad (2.9)$$

In the upper equation $\alpha^a(x)$ (with $a = 1, \dots, 8$) represent group-parameters, while T_a are the eight generators of this group. These are linearly independent, hermit 3x3 matrices with trace equal to zero. Due to the non-abelian character of $SU(3)$, the elements of this matrix do not commute. In order to conserve gauge invariance, a covariant substitute for the derivative ∂_μ has to be introduced in equation 2.8 as discussed in the previous section:

$$D_\mu = \partial_\mu + ig_s T_a G_\mu^a \quad (2.10)$$

This results in eight gauge fields G_μ^a , which are closely related to the eight mediators (gluons) of the strong interaction. Applying 2.10 results in the following transformation of G_μ^a :

$$G_\mu^a \rightarrow G_\mu^{a'} = G_\mu^a - \frac{1}{g_s} \partial_\mu \alpha^a - f_{bc}^a \alpha^b G_\mu^c \quad (2.11)$$

The gauge invariant form of G_μ^a is very similar to its QED equivalent (2.5) except for the term $-f_{bc}^a \alpha^b G_\mu^c$ including the structure constant f_{bc}^a . This last term expresses the non-abelian character of $SU(3)$, since it prevents the gauge field from not commuting.

Finally the additional term $-\frac{1}{4}G_{\mu\nu}^a G_a^{\mu\nu}$ is added to the Lagrangian in order to take into account gluon interactions and gluon kinematics. Applying all previous steps leads to the following, now gauge invariant, Lagrangian:

$$\begin{aligned} \mathcal{L} &= \bar{q}_j(i\gamma^\mu\partial_\mu - m)q_j - g(\bar{q}_j\gamma^\mu T_a q_j)G_\mu^a - \frac{1}{4}G_{\mu\nu}^a G_a^{\mu\nu} \\ G_{\mu\nu}^a &= \partial_\mu G_\nu^a - \partial_\nu G_\mu^a - gf_{bc}^a G_\mu^b G_\nu^c \end{aligned} \quad (2.12)$$

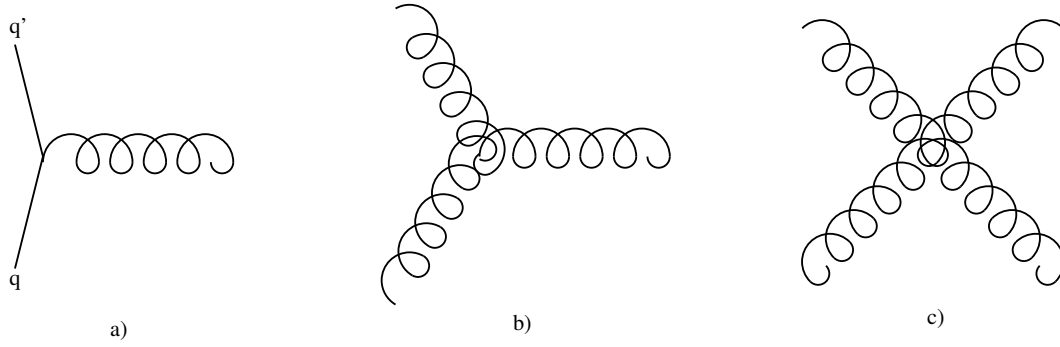


Figure 2.1: The three possible gluon interactions in QCD: a) quark–gluon coupling b) triple–gluon vertex c) four–gluon vertex.

This equation does not only describe the fundamental interaction between quarks, it also takes into account couplings to gluons and their self interactions (see Fig. 2.1). This self interaction term is responsible for the so called “quark confinement”, which restricts free colour-charged particles. Details on this particular property of the strong interaction will be given in section 2.4.

Equation 2.12 can be also expressed in a more elegant way using symbolic short cuts, which put a stress on the different couplings and their contribution to the Lagrangian:

$$\mathcal{L} = \bar{q}q + g_s \bar{q}q G + G^2 + g_s G^3 + g_s^2 G^4 \quad (2.13)$$

The different terms of equation 2.13 have the following meaning:

- $\bar{q}q$: kinematics of free quarks
- G^2 : kinematics of free gluons
- $g_s \bar{q}q G$: quark–gluon coupling
- $g_s G^3$: triple–gluon vertex (gluon self interaction)
- $g_s^2 G^4$: four–gluon vertex (gluon self interaction)

2.3 The weak interaction

The weak interaction requires the existence of charged mediators. Here the β -decay with a neutron decaying to a proton, a charged lepton and a neutrino gives a typical example. Another requirement for the mediating bosons is mass in

order to explain the limited range of this fundamental force. This again brings up the topic “gauge invariance of massive vector bosons”, which will be discussed in detail in chapter 2.5. For the moment massless mediators are assumed.

First a generalized form of the phase transition known from chapter 2.1 will be introduced. Charge as a measure for the strength of an electromagnetic coupling is replaced in this case by “g”, the coupling for weak interactions. Additionally the Pauli matrices (represented by τ) are chosen, since the transformation is asked to be unitary and hermitian with a trace equals to zero.

$$\Psi'(x) = e^{i\frac{g}{2}\tau\beta(x)}\Psi(x) \quad (2.14)$$

Equation 2.14 stands for a local SU(2) phase transition. Both SU(2) and SU(3) discussed in the previous section are non-abelian groups, since they do not commute.

In order to achieve local gauge invariance for SU(2), one has to introduce once again a covariant derivative, which takes this time the following form:

$$D_\mu = \partial_\mu + i\frac{g}{2}W_\mu^a \tau_a \quad (2.15)$$

Analogous to the previous sections, the weak field W^μ changes by introducing the covariant derivative and transforms by applying local phase transition in the following way:

$$W_\mu^a \rightarrow W'^a_\mu = W_\mu^a - \partial_\mu\beta^a - g(\epsilon_{abc}\beta^b W_\mu^c) \quad (2.16)$$

This equation is very similar to the one found in the previous section, except for the cross-product $-g(\epsilon_{abc}\beta^b W_\mu^c)$. This is due to the non-abelian character of SU(2) and prevents 2.16 from commuting.

Focusing on the electroweak theory introduced by Glashow, Salam and Weinberg, one needs a new group in order to provide a unification of QED and weak interaction. This new group is called $SU(2)_L \otimes U(1)_Y$ group. Concerning the weak interaction, fermions are divided up in two groups: left-handed doublets and right-handed singlets (see table 2.2). This distinction originates from the observation, that the charged current of the weak interaction is only coupling to left-handed particles – that is the reason for the L in $SU(2)_L$. Experimentally this property of the weak interaction was first discovered by Wu[Wu57] in 1957. Chirality³ is defined by the two chiral components Ψ_L and Ψ_R :

$$\Psi_L = \frac{1 - \gamma^5}{2}\Psi \quad (2.17)$$

$$\Psi_R = \frac{1 + \gamma^5}{2}\Psi \quad (2.18)$$

³handedness

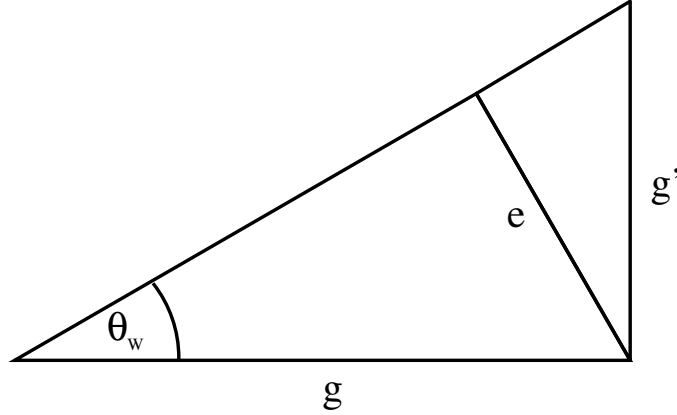


Figure 2.2: Geometrical representation of the three coupling constants e , g and g' via the coupling angle θ_W (Weinberg angle).

Concerning QED, one cannot use the $U(1)_{QED}$ group, since this would lead to doublets with same charge. Consequently a charged lepton and its neutrino would have the same charge, what contradicts to experimental observations. Therefore charge is replaced by another quantity named hypercharge Y . This is closely related to the charge Q (generator of $U(1)_{QED}$) and the third component of the weak isospin I_3 (generator of $SU(2)_L$) via the so-called Gell-Mann–Nishijima relation.

$$Q = I_3 + \frac{Y}{2} \quad (2.19)$$

The corresponding covariant derivative of this $SU(2)_L \otimes U(1)_Y$ group is extended by B_μ with respect to equation 2.16 and hence leads to:

$$D_\mu = \partial_\mu + i\frac{g'}{2}B_\mu Y + i\frac{g}{2}W_\mu^a \tau_a \quad (2.20)$$

Here g and g' represent the coupling constant for $SU(2)_L$ and $U(1)_Y$ respectively. Fig. 2.2 gives a nice and clear representation of the relation between the three coupling constants of $SU(2)_L$, $U(1)_Y$ and $U(1)_{QED}$.

Now all presuppositions are fulfilled to construct the invariant Lagrangian with respect to local phase transition, with the fermions and bosons assumed massless for the moment. This is necessary to assure gauge invariance. The masses will be provided by the Higgs-mechanism described in chapter 2.5.

$$\mathcal{L} = \bar{\Psi} \gamma^\mu (i\partial_\mu - \frac{g}{2}W_\mu^a \tau_a - g'\frac{Y}{2}B_\mu) \Psi \quad (2.21)$$

$$- \frac{1}{4}W_a^{\mu\nu} W_{\mu\nu}^a - \frac{1}{4}B^{\mu\nu} B_{\mu\nu} \quad (2.22)$$

The tensors $W_{\mu\nu}^a$ and $B_{\mu\nu}$ can be rewritten in the following way:

$$W_{\mu\nu}^a = \partial_\mu W_\nu^a - \partial_\nu W_\mu^a - g\epsilon_{abc}W_\mu^b W_\nu^c \quad (2.23)$$

$$B_{\mu\nu} = \partial_\mu B_\nu - \partial_\nu B_\mu \quad (2.24)$$

The first part of the Lagrangian (see 2.21) deals with the kinematics of fermions and their coupling to the gauge bosons, while the second part (see 2.22) describes the kinematics of these bosons.

According to the standard model, the weak interaction is mediated by a pair of charged (W^\pm) and a one neutral (Z^0) boson, while electromagnetism is interacting via the neutral photon. These mediators are linear combinations of W_μ^a and B_μ , the vector fields of the $SU(2)_L \otimes U(1)_Y$ group and can be expressed using the weak mixing angle θ_W ⁴ (see also Fig. 2.2):

$$A_\mu = B_\mu \cos \theta_W + W_\mu^3 \sin \theta_W \quad (2.25)$$

$$Z_\mu = -B_\mu \sin \theta_W + W_\mu^3 \cos \theta_W \quad (2.26)$$

$$W_\mu^\pm = \frac{1}{\sqrt{2}}(W_\mu^1 \mp iW_\mu^2) \quad (2.27)$$

These equations once more stress the close relation between electromagnetism and weak interaction. Photon, Z^0 and W^\pm bosons are made up of gauge fields belonging to both symmetry groups.

Weak leptonic decays have proven to conserve CP⁵ and for some time CP was considered being a conserved quantity in general. This turned out to be wrong, as CP violating weak hadronic decays were observed. They gave one motivation to introduce the so-called *Cabibbo–Kobayashi–Maskawa* matrix⁶. Another reason was the requirement of flavour mixing, since flavours turned out to be a mix of different mass eigenstates. The V_{CKM} transforms lefthanded d , s and b -quarks to their corresponding mixed states d' , s' and b' :

$$\begin{pmatrix} d' \\ s' \\ b' \end{pmatrix}_L = \begin{pmatrix} V_{ud} & V_{us} & V_{ub} \\ V_{cd} & V_{cs} & V_{cb} \\ V_{td} & V_{ts} & V_{tb} \end{pmatrix} \bullet \begin{pmatrix} d \\ s \\ b \end{pmatrix}_L \quad (2.28)$$

One important property of V_{CKM} are the complex elements of this matrix. The non-zero phase in some of the off-diagonal elements is a pre-requirement for CP violating decays. However, they do not affect the flavour mixing, since this only depends on the absolute values of the matrix elements. Nice examples for the

⁴Weinberg angle

⁵charge conjugation; **p**arity: product of charge and parity

⁶short cut: V_{CKM}

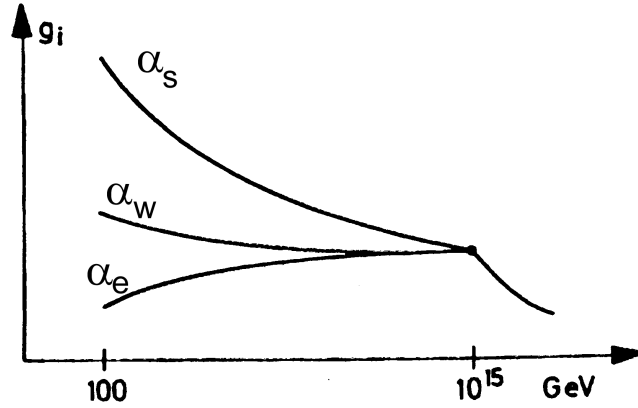


Figure 2.3: Running of the three main interaction coupling constants. All three forces should unify at high energy. A perfect unification is not possible in the Standard Model, but can be achieved using a supersymmetric extension[[dB94](#)].

effect of flavour mixing are the decays of groundstate B-mesons and kaons. Both mesons would be absolutely stable without the existence of mixed flavour states. V_{CKM} allows the following decay chain:

$$b \rightarrow c \rightarrow s \rightarrow u \quad (2.29)$$

Consequently B-mesons are able to decay to D-mesons, with the B showing a remarkably long lifetime. This property is exploited for the identification of this meson. The reason for its longevity can be found in the V_{cb} element, which is rather small compared to the corresponding on-diagonal element. Consequently this decay is suppressed and leads to a long B lifetime. An overview over all experimentally determined V_{CKM} elements is given in the following list[[Par00](#)]:

$$\begin{array}{lll} |V_{ud}| = 0.9742 - 0.9757 & |V_{us}| = 0.2190 - 0.2260 & |V_{ub}| = 0.0020 - 0.0050 \\ |V_{cd}| = 0.2190 - 0.2250 & |V_{cs}| = 0.9734 - 0.9749 & |V_{cb}| = 0.0370 - 0.0430 \\ |V_{td}| = 0.0040 - 0.0140 & |V_{ts}| = 0.0350 - 0.0430 & |V_{tb}| = 0.9990 - 0.9993 \end{array}$$

2.4 The running coupling constants

The three fundamental forces electromagnetism, weak and strong interaction occur in experimental measurements with different relative strength. Hence matter is also affected differently strong by each of these interactions. For electromagnetism the strength of this coupling is expressed via the fine structure constant α_0 :

$$\alpha_0 = \frac{e^2}{4\pi} \approx \frac{1}{137} \quad (2.30)$$

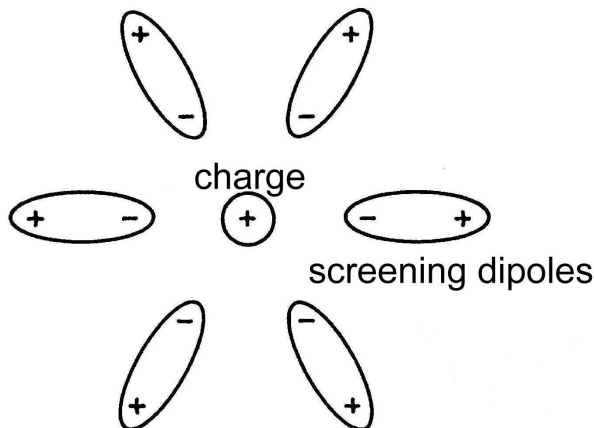


Figure 2.4: Screening of an electric charge by virtual dipoles.

Since this constant is much smaller than unity, one can use perturbation theory to describe QED because higher order terms will contribute less. This requirement for a perturbative description is not necessarily fulfilled for the strong interaction α_s :

$$\alpha_s = \frac{g_s^2}{4\pi} \quad (2.31)$$

Here perturbation theory cannot be used anymore for the full range of energies and it is restricted to higher energies only, where α_s gets small enough.

It turns out, that the coupling α_s decreases with increasing momentum transfer Q . The fine structure constant α shows a similar dependency, but with opposite sign. The latter can be understood from vacuum polarization, because the virtual electron–positron pairs cause a screening of the true charge by acting like a dielectric medium. Hence one can always see only a reduced “effective” charge due to the surrounding dipoles. If one closes in on the true charge by increasing the momentum transfer Q , the amount of screening dipoles reduces and consequently the effective charge increases resulting in a greater coupling constant according to equation 2.30 (see also Fig. 2.4). In real life these effects can be observed with particle accelerators like LEP⁷, where electrons and positrons collide at high energies leading to high Q values. In 1993 $\alpha_e(M_Z^2)$ was determined [Hol93, Sch93] and resulted in $\frac{1}{128.9}$. This is significantly larger than the fine structure constant at low energies.

The strong interaction is also affected by a screening effect with the charge being replaced by a colour charge and the dipoles being made up of $q\bar{q}$ quark pairs. But the screening is dominated by a second anti-screening effect [YM54], which did not occur in case of the QED. Here the gluon itself carries a colour

⁷Large Electron Positron collider

charge, which enables them to self interact with each other, adding gluon loop corrections to the Feynman diagrams. This leads to a reduced “effective” colour charge the closer one gets to the true charge because less gluons contribute to the observed charge. As a consequence, bound quarks behave like free particles due to their short distance to each other. This behavior is also known as *asymptotic freedom* and is one of the characteristics of non-abelian gauge theories since only these allow charged mediators. The strong coupling on the other hand increases with increasing distances, since more gluons contribute with their colour charge. As a consequence it is not possible to observe free quarks. This behavior is also known as *quark confinement*.

2.5 The Higgs mechanism in the standard model

In one of the previous chapters the problem of gauge invariant massive fields was already encountered. As soon as mass terms are introduced, gauge invariance is destroyed. A very elegant way of avoiding this problem is the so-called “spontaneous symmetry breaking”. This principle assumes all particles being massless in the first place and hence keeping gauge invariance is unproblematic. Mass is generated by introducing an additional scalar background field, which does not affect gauge invariance, but gives mass to the gauge bosons of the weak interaction. This field is called the *Higgs field*.

The Higgs field is chosen to be a scalar, complex field Φ with two components. It has to be invariant under $SU(2) \otimes U(1)$ with ϕ^+ representing a charged and ϕ^0 standing for a neutral field:

$$\Phi = \frac{1}{\sqrt{2}} \begin{pmatrix} \phi_1^+ + i\phi_2^+ \\ \phi_1^0 + i\phi_2^0 \end{pmatrix} \quad (2.32)$$

The corresponding Lagrangian for scalar particles can be used:

$$\mathcal{L}_{Higgs} = (\partial_\mu \Phi)^\dagger (\partial^\mu \Phi) - V(\Phi^\dagger \Phi) \quad (2.33)$$

Here the potential $V(\Phi^\dagger \Phi)$ is chosen such, that a non-trivial and non-zero minimum in the complex Φ plane occurs:

$$V(\Phi^\dagger \Phi) = -\mu^2 \Phi^\dagger \Phi + \lambda^2 (\Phi^\dagger \Phi)^2 \quad (2.34)$$

This choice results in two physically meaningful solutions for V depending on the parameters λ and μ . Only one of these two solutions yields a potential with a non-trivial and non-zero minimum. By choosing $\mu > 0$ one obtains such a potential, illustrated by Fig. 2.5. Since the minimum is aligned along a circular

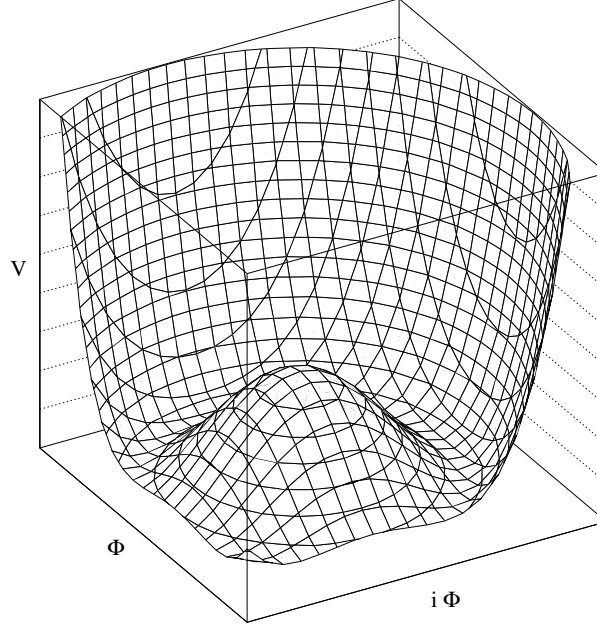


Figure 2.5: The degenerate Higgs potential for $\mu^2 > 0$.

valley in the complex Φ plane at the same potential energy, the vacuum state of V is infinitely degenerated:

$$|\Phi|_{\text{vacuum}} = \frac{1}{\sqrt{2}} \begin{pmatrix} 0 \\ \nu \end{pmatrix}; \quad \nu = \frac{\mu}{\lambda} \quad (2.35)$$

Since the vacuum is not electrically charged, one can assume the charged part of this solution to be zero. The neutral part can be easily derived from equation 2.5 by asking for a minimum.

One can express this potential with respect to its vacuum expectation value 2.35 by using infinitesimal, complex corrections $\eta + i\zeta$. These parameterize the complex Φ plane with respect to $|\Phi|_{\text{vacuum}}$ and leads to an alternative expression for the Higgs field initially introduced with 2.32:

$$\Phi = \frac{1}{\sqrt{2}} \begin{pmatrix} 0 \\ \nu + \eta + i\zeta \end{pmatrix} \quad (2.36)$$

The charged part of this Higgs field representation is zero and indeed a charged Higgs field with non-zero vacuum expectation value would lead to photons with mass. The corresponding potential results from applying this parameterization

to the potential equation 2.34 and yields the following expression:

$$V(\Phi^\dagger\Phi) = \mu^2 \left[-\Phi^\dagger\Phi + \frac{1}{\nu^2}(\Phi^\dagger\Phi)^2 \right] \quad (2.37)$$

$$= \mu^2 \left[-\frac{1}{4}\nu^2 + \eta^2 + \frac{\eta\zeta^2}{\nu} + \frac{\eta^2\zeta^2}{2\nu^2} + \mathcal{O}(\eta^3) + \mathcal{O}(\zeta^4) \right] \quad (2.38)$$

Due to the infinitesimal character of η and ζ , higher order terms can be neglected. The same is true for the mixed terms $\frac{\eta\zeta^2}{\nu}$ and $\frac{\eta^2\zeta^2}{2\nu^2}$. Applying this potential and the Higgs field 2.36 to the Lagrangian 2.33 results in a new representation for \mathcal{L}_{Higgs} :

$$\mathcal{L}_{Higgs} = \left[\frac{1}{2}(\partial_\mu\eta)(\partial^\mu\eta) - \mu^2\eta^2 \right] + \left[\frac{1}{2}(\partial_\mu\zeta)(\partial^\mu\zeta) \right] + \dots \quad (2.39)$$

Equation 2.39 only contains the two leading terms. The first one represents the Klein–Gordon equation for a massive scalar particle η : the Higgs boson. Its mass yields:

$$\frac{1}{2}m_\eta^2 = \mu^2 \Rightarrow m_\eta = \sqrt{2}\mu \quad (2.40)$$

The second term also stands for a scalar particle ζ , but without any mass term. This so-called *Goldstone boson* can be eliminated by performing a local phase transition. Due to the three rotations of SU(2) there exist three Goldstone bosons in the Standard Model, each of them having one degree of freedom. By eliminating these, the three degrees of freedom lost are recovered as longitudinal polarizations of the three heavy gauge bosons.

2.5.1 Giving mass to W^\pm and Z^0 bosons

In order to give mass to the gauge bosons, one has to extend the Lagrangian of a scalar particle 2.33 by a gauge field Lagrangian \mathcal{L}_{gauge} :

$$\mathcal{L} = \mathcal{L}_{Higgs} + \mathcal{L}_{gauge} \quad (2.41)$$

$$\mathcal{L}_{gauge} = -\frac{1}{4}W_{\mu\nu}^i W^{i\mu\nu} - \frac{1}{4}B_{\mu\nu}B^{\mu\nu} \quad (2.42)$$

W and B represent the field tensors of the weak and electromagnetic interactions respectively (see 2.23 and 2.24). The covariant derivative, necessary to conserve gauge invariance, has the known form 2.20:

$$D_\mu = \partial_\mu + i\frac{g'}{2}B_\mu Y + i\frac{g}{2}W_\mu^a \tau_a$$

Now the usual procedure of replacing the regular derivative in the Lagrangian 2.41 by its corresponding covariant form is applied and leads to a gauge invariant form

of this Lagrangian. The kinetic part is shown below, assuming a weak hypercharge Y of 1:

$$\mathcal{L}_{kin} = \frac{1}{4} [(gW_\mu^i \tau_i + g'B_\mu) \Phi]^\dagger [(gW^{\mu i} \tau_i + g'B^\mu) \Phi] \quad (2.43)$$

By expressing the W_μ^i and B_μ terms with the physical fields A_μ , Z_μ and W_μ^\pm using expressions 2.25, 2.26 and 2.27 one finally ends up with a Lagrangian consisting of four main parts:

$$\mathcal{L} = \left[\frac{1}{2} (\partial^\mu \eta) (\partial_\mu \eta) - \mu^2 \eta^2 \right] \quad (2.44)$$

$$- \frac{1}{4} W_{\mu\nu}^i W^{i\mu\nu} - \frac{1}{4} B_{\mu\nu} B^{\mu\nu} \quad (2.45)$$

$$+ \frac{1}{2} \cdot \frac{g^2 \nu^2}{4} \left((W_\mu^+)^2 + (W_\mu^-)^2 \right) \quad (2.46)$$

$$+ \frac{1}{2} \cdot \frac{g^2 \nu^2}{4 \cos(\theta_W)^2} (Z_\mu)^2 \quad (2.47)$$

The first part 2.44 is the well known Klein–Gordon equation for the massive Higgs particle with $m_H = \sqrt{2}\mu$. Next comes the gauge field Lagrangian \mathcal{L}_{gauge} followed by two mass terms 2.46 and 2.47. One can now easily extract the masses for W^\pm and Z^0 bosons yielding:

$$m_W = \frac{g\nu}{2} \quad (2.48)$$

$$m_Z = \frac{g\nu}{2 \cos(\theta_W)} \quad (2.49)$$

$$= \frac{m_W}{\cos(\theta_W)} \quad (2.50)$$

It is striking, that m_Z and m_W are hence directly connected via the weak interaction angle θ_W . Another interesting consequence can be concluded from the absence of a mass term for A_μ :

$$A_\mu = \frac{1}{\sqrt{g^2 + g'^2}} (gB_\mu + g'W_{3\mu}) \quad (2.51)$$

The photon does not obtain a mass, which is in agreement with experimental observations.

2.5.2 Giving mass to fermions

For fermions one is basically facing the same problem as for bosons. The Dirac equation is only invariant under gauge transformations, if all fermions are massless. Since this would lead to massless quarks and massless charged leptons,

the Higgs mechanism is needed again to introduce mass terms by spontaneous symmetry breaking.

The Lagrangian dealing with the Higgs coupling to fermions contains a free parameter, the so-called *Yukawa* coupling g_Y^f , which is different for every charged lepton and quark. In the following example the electron and its corresponding Yukawa coupling g_Y^e are chosen:

$$\mathcal{L}_{Yukawa} = -g_Y^e \left[\bar{e}_R \Phi^\dagger \begin{pmatrix} \nu_e \\ e \end{pmatrix}_L + \begin{pmatrix} \bar{\nu}_e \\ \bar{e} \end{pmatrix}_L \Phi e_R \right] \quad (2.52)$$

By applying the vacuum expectation for Φ (see equ. 2.35) to the Lagrangian 2.52 one obtains the following fermion mass term:

$$\mathcal{L}_{Yukawa} = -\frac{g_Y^e}{\sqrt{2}} \left[\bar{e}_R (0, \nu) \begin{pmatrix} \nu_e \\ e \end{pmatrix}_L + \begin{pmatrix} \bar{\nu}_e \\ \bar{e} \end{pmatrix}_L \begin{pmatrix} 0 \\ \nu \end{pmatrix} e_R \right] \quad (2.53)$$

$$= -\frac{g_Y^e}{\sqrt{2}} [\bar{e}_L e_R + \bar{e}_R e_L] \quad (2.54)$$

$$= -\underbrace{\frac{g_Y^e}{\sqrt{2}}}_{m_e} \bar{e} e \quad (2.55)$$

Consequently g_Y^e has to be chosen such that m_e in equation 2.55 yields a result compatible with experimental observations. This procedure can be repeated with all other fermions and quarks leading to a set of Yukawa coupling parameters which all have to be adjusted manually.

Since the g_Y^f is proportional to its corresponding fermion mass, the Higgs field couples mostly to heavy fermions. Due to the charged part of the vacuum expectation Φ being zero, the neutrinos completely disappeared from the mass term 2.54 leading to massless neutrinos.

Chapter 3

The experiment

All data used to perform the analyses described in this thesis were taken at LEP¹, a circular accelerator for electrons and positrons which was shut down end of 2000 leaving a remarkable amount of physical data. This large accelerator was part of CERN, one of the biggest research centers in Europe. CERN has been founded in 1954 by 12 european countries in order to provide a facility for a huge variety of physical experiments. Such a huge project can only be realised, financed and maintained by an international collaboration. One of the greatest successes of this example for international teamwork was the verification of W and Z bosons[UA185] in 1985. In the mean time, the amount of collaborating countries increased to 80 and CERN is right now aiming towards the next huge project, the LHC² accelerator. This new collider will allow to investigate even higher energy regions and hence enable scientists to discover even more massive particles.

3.1 The LEP accelerator

The LEP accelerator started its operation in 1989 after 6 years of construction. Its purpose was to accelerate electrons and their corresponding anti-particles, the positrons, to high energies and finally force both to collide with each other leading to an annihilation by pairs. During this process a lot of particles are created from the energy provided by the annihilation. These get detected and identified by detector systems optimised for this task. LEP provided four detectors with high

¹Large Electron Positron collider

²Large Hadron Collider

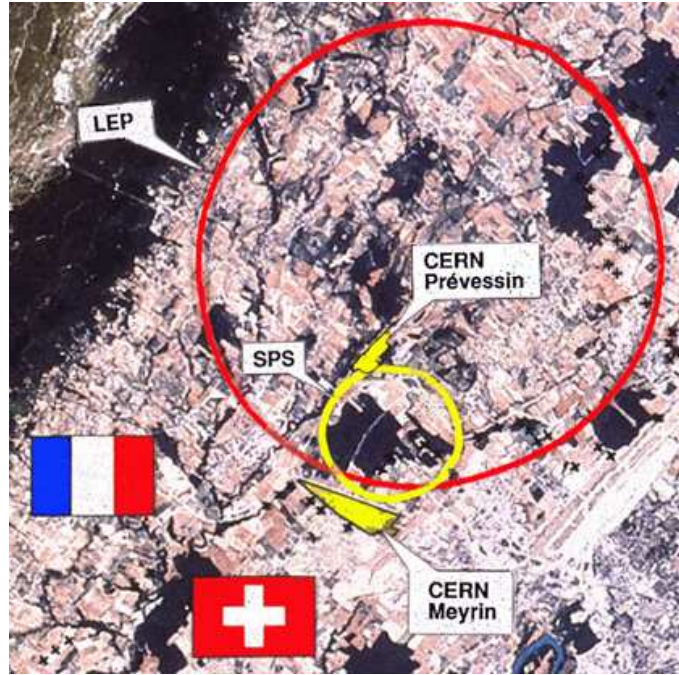


Figure 3.1: CERN, the LEP accelerator and the surrounding area.

energetic electron–positron pairs, namely: ALEPH³, DELPHI⁴, OPAL⁵ and L3⁶. In one of the next chapters DELPHI will be presented in more detail, since all data used for this thesis was accumulated by this detector. With a circumference of 26.7 km, LEP was the biggest accelerator of its kind. The underground system consisting of tunnels and caverns was between 50 m and 175 m below the surface in order to protect the experiments from disturbing influences like cosmic rays. The main tunnel hosting LEP’s beam pipe was 3.8 m to 5.5 m in diameter, reaching across the French–Swiss border (see map 3.2). Constructing LEP took 6 years (1983 – 1989) and cost 1.3 million Swiss Francs, which were distributed among the participating countries (14 member states at that time).

If one takes a closer look, the “ring” consists of 8 straight parts (500 m each) and 8 curved parts (2.8 km each). Each of the 4 detectors was hosted in a big cavern situated in one of the straight parts together with the cavities needed for acceleration. Due to the different charge of electrons and positrons, both could be accelerated at the same time heading in opposite directions. For that purpose, alternating electromagnetic fields with high frequencies and an effective voltage of 400 MV per round were generated. In the curved parts of the beam pipe

³Apparatus for **LEP** Physics

⁴Detector with **L**epton and **H**adron **I**dentification

⁵**O**mn*i* **P**urpos*e* **A**pparatus for **LEP**

⁶Third letter of intend

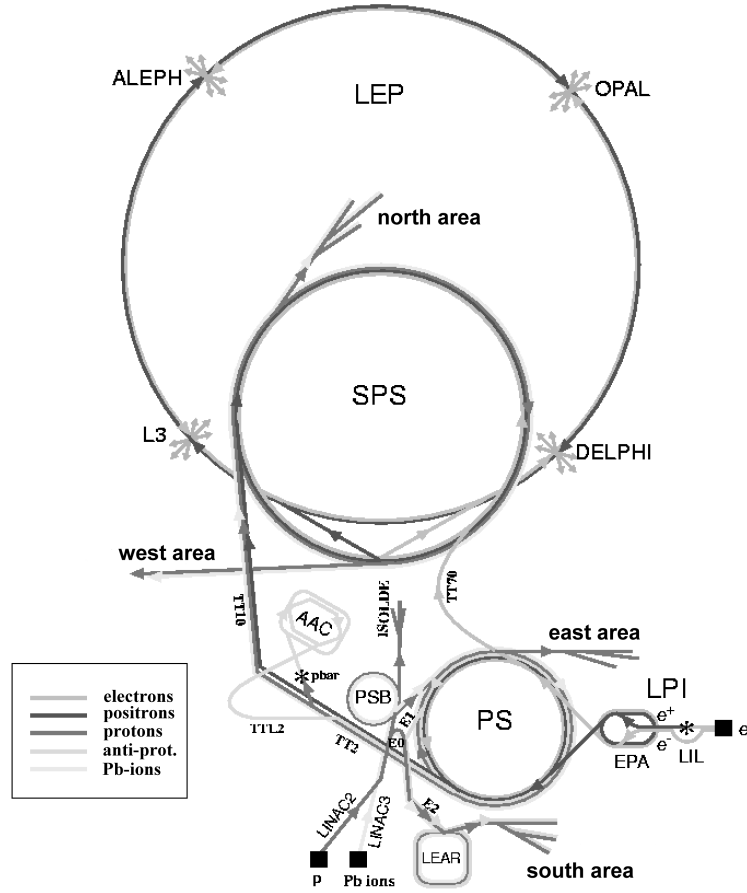


Figure 3.2: LEP and its pre-accelerators.

dipole solenoids kept the particle stream on track. For focusation close to the interaction points quadrupole and sextupole solenoids were used.

The acceleration procedure of LEP happened in several steps taking advantage of two older and smaller acceleration rings which were also used for other experiments (see map 3.2). The first step was to generate electrons in a linear accelerator (**LIL**) with 200 MeV energy. These were partially rerouted to a converter target in order to produce positrons. Both particle streams got further accelerated to 600 MeV and finally ended up in a storage ring (**EPA**). After sufficient electrons and positrons had been accumulated, the next acceleration step to 3.5 GeV was performed in the proton synchrotron (**PS**) followed by the super proton synchrotron (**SPS**) which delivered them directly to **LEP** after the last pre-acceleration to approximately 22 GeV. Here the electron and positron bunches received their final acceleration to *physics energy*. In its quest to find the Higgs, the LEP experiments needed energies as high as possible which lead

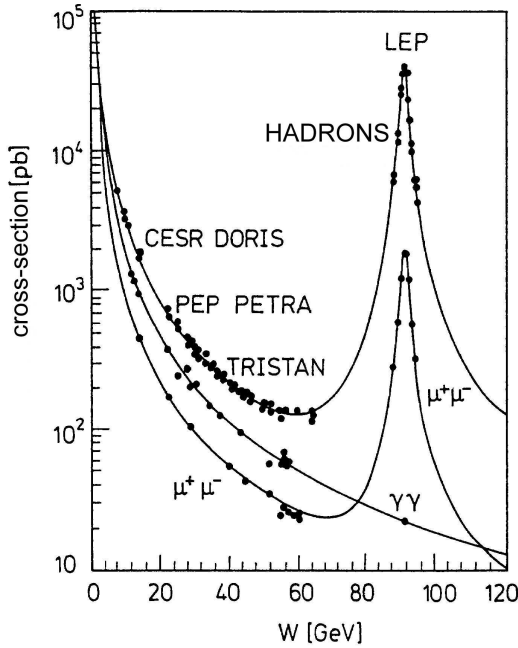


Figure 3.3: Cross-section plotted vers. centre-of-mass energy. The peak at 91 GeV is clearly visible for hadronic and leptonic Z^0 decays. Points symbolize measured results, while solid lines stand for theoretical predictions (plot taken from [Sch95]).

to a maximum of 104.5 GeV per beam at the end of LEP's operation winter 2000. Technical limitations were primarily due to the cavities, which were operated beyond their design capabilities and hence tended to become unstable. Another limitation was emerging directly from the circular shape of the accelerator: synchrotron radiation. The amount of energy radiated increases with the beam energy by a power of four, leading to an enormous loss of roughly 30 MW at 100 GeV beam energy.

Between 1989 and 1995 LEP was operating at a beam energy of approx. 46 GeV, resulting in a centre-of-mass energy of approx. 91 GeV, which lies precisely at the Z^0 resonance peak. This phase was called *LEP 1* and made Standard Model checks and measurements of Z^0 decay processes possible due to the dominant production of these bosons (see fig. 3.3). After 1995 LEP energy was slowly raised and finally reached its maximum of 209 GeV centre-of-mass energy by the end of 2000.

An important parameter to estimate the power of an accelerator is its luminosity together with beam or centre-of-mass energy. A common definition is:

$$\mathcal{L} = \frac{n}{\sigma} \quad (3.1)$$

with n representing the amount of events per second and σ defining the corresponding cross-section. One can also express the luminosity using machine

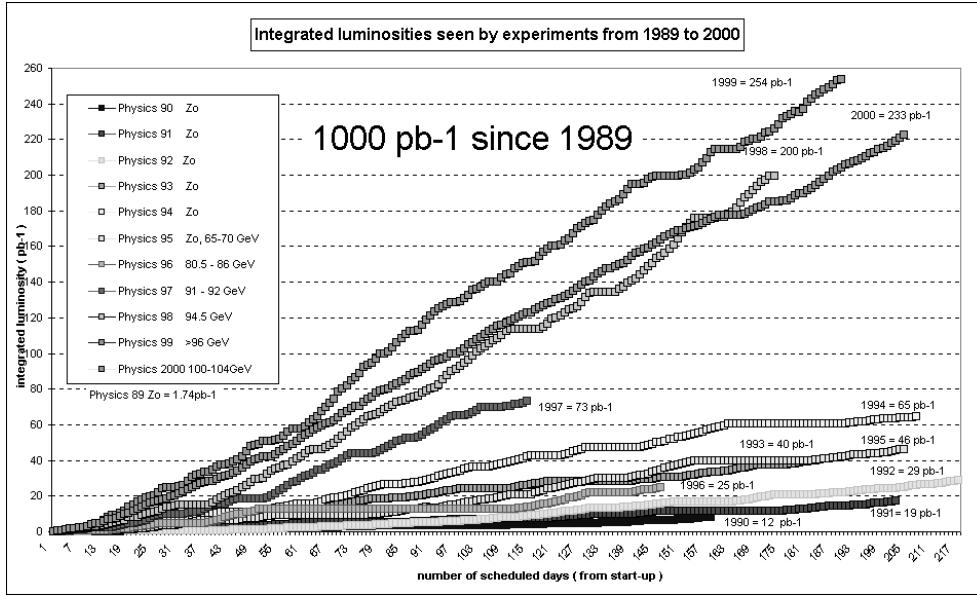


Figure 3.4: Integrated luminosity in the years from 1989 to 2000.

parameters:

$$\mathcal{L} = \frac{N^+ N^- k f}{4\pi \sigma_x \sigma_y} \quad (3.2)$$

Here the nominator contains the amount N of electrons and positrons per bunch, the amount of bunches k and the circulation frequency f . The denominator takes into account the beam width σ_x and σ_y in the x-y plane orthogonal to the beam axis assuming a normal distribution for both. Fig 3.4 gives an overview of the integrated luminosities accumulated per experiment in the years of 1989 until 2000.

3.2 The DELPHI detector

DELPHI was one of the four detectors at LEP. It was situated in an underground cavern approximately 100 m below the surface. It had a cylindrical shape of 8 m in length and 5 m in radius. The total weight amounted to approximately 3500 t. In order to provide an easy maintenance, the apparatus was installed on a rail track system. This allowed easy access to the barrel part, since each endcap could be removed using the rail system (see fig. 3.5). Design and construction of this detector took seven years.

The geometry of DELPHI suggests the usage of cylindrical coordinates with the z -axis pointing in beam pipe direction and the $R\phi$ -plane orthogonal to it. Spherical coordinates are also very common with the $\theta = 0^\circ$ axis pointing in beam

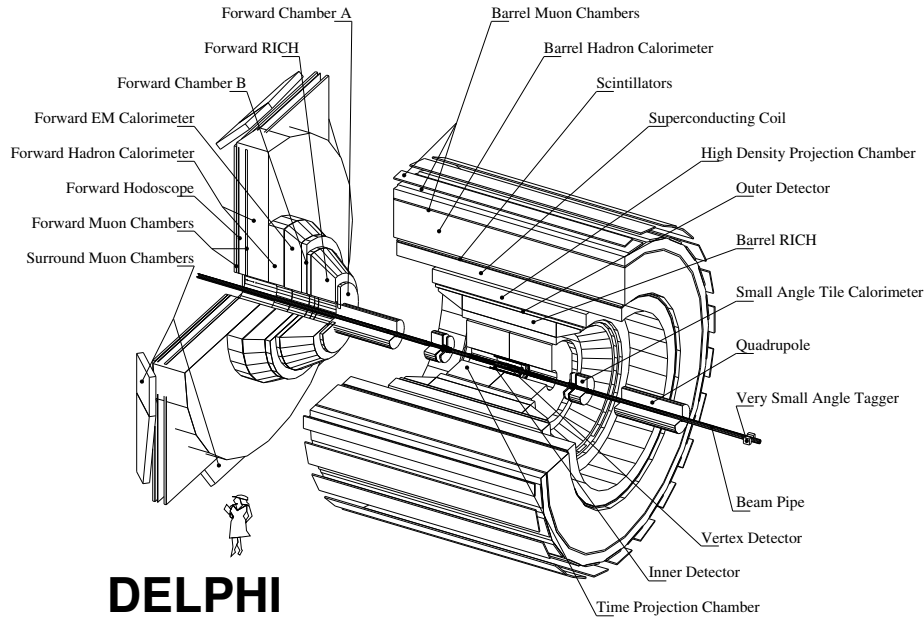


Figure 3.5: Sketch of the DELPHI detector and its sub-detectors.

pipe direction. Dealing with the different sub-detector systems, polar angles θ will be only given for one hemisphere ($0^\circ < \theta < 90^\circ$), automatically extending the definition also to the other hemisphere ($\theta' = 180^\circ - \theta$).

Regarding the performance of this detector, it is characterised by a good vertex reconstruction and a modern particle identification system. Therefore different sub-detector components were designed, each specialised for a certain task. These subsystems of DELPHI will be subject to the next sections in this chapter. A general feature, all particle detectors are aiming at, is a good coverage in θ and ϕ , since particles escaping detection due to cracks in the detector material would lead to misidentifications. DELPHI provides a good overall coverage and has basically only three angular regions with reduced detection efficiency:

- near $\theta = 0^\circ$, close to the beam pipe
- near $\theta = 40^\circ$, where the detector end-caps meet the barrel part (see fig. 3.5)
- near $\theta = 90^\circ$, barrel centre, where the two barrel parts were welded

In order to minimize the probability of misidentifying an event due to particles in these regions, special hermeticity counters were installed acting as a veto system. These counters covered the regions at $\theta = 40^\circ$ and $\theta = 90^\circ$. Close to the beam pipe the STIC⁷ could be used as veto system.

⁷Small angle **T**ile **C**alorimeter

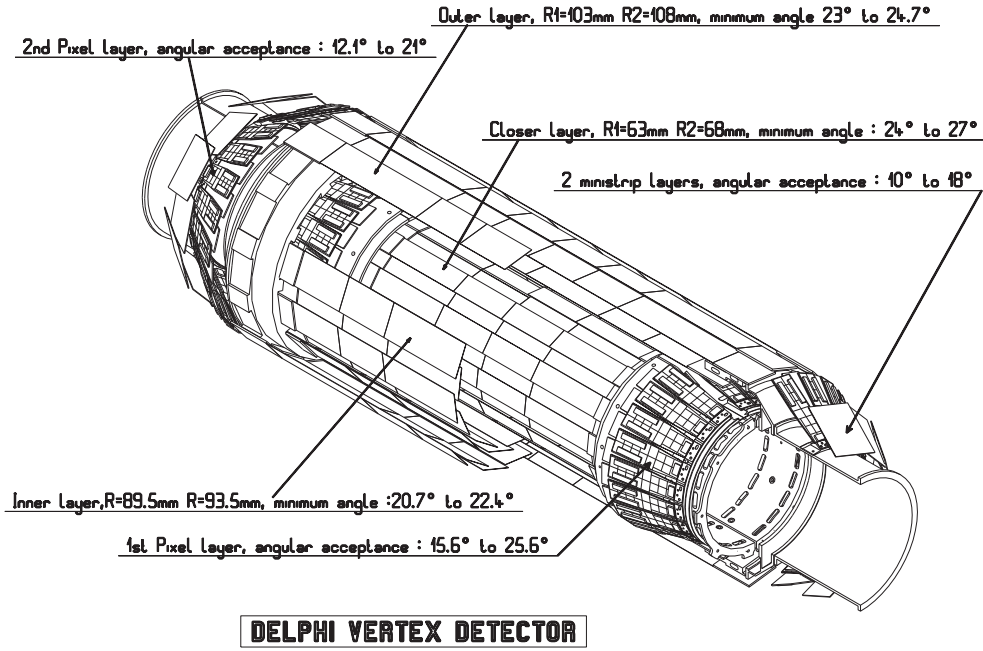


Figure 3.6: Side view on the DELPHI vertex detector.

The following section can only give an overview of the different sub-detector systems of DELPHI. For a more detailed technical description, please refer to [A⁺91] and [A⁺96].

3.2.1 The tracking system

The superconducting solenoid

Momentum reconstruction of charged particles is performed measuring the curvature in strong, homogeneous magnetic fields. DELPHI's superconducting solenoid enclosed all sub-detectors relevant for the tracking and generated a magnetic field of 1.23 Tesla. The geometry of this solenoid was cylindrical with a length of 7.4 m and a radius of 2.6 m. The current necessary to keep up such a strong field was 5000 A. In order to improve the field homogeneity, 35 cm broad wire layers were installed in the end-caps. Superconductivity was assured by keeping the solenoid at a constant temperature of 4.6 K using liquid helium.

The vertex detector (VD)

The silicon vertex detector is typically placed very close to the beam pipe. Given a good resolution, this makes track extrapolations back to their origin possible. Such a feature plays an important role in the identification of secondary vertices, one of the key properties of B-meson decays. After the final upgrade, the DELPHI vertex detector consisted basically of two main parts with different layouts and functionalities (see fig. 3.6).

The barrel part covered a polar angle area of $\theta > 23^\circ$. It consisted of three layers of silicon strip detectors, named after their relative distance to the beam pipe: closer layer, inner layer and outer layer. All three layers were overlapping each other resulting in a resolution of $7.6 \mu m$ in $r\phi$. In order to gain sensitivity in z direction, another set of strip detectors was added to both ends of the VD, resulting in a resolution of $9 \mu m$ in z .

For angles smaller than $\theta = 23^\circ$ the VD was upgraded in 1994 by adding the VFT⁸. For this module a combination of silicon strip and pixel detectors was used. The resolution resulting from the strip detectors was of the same magnitude as for the barrel part, but the pixel detectors allowed only $330 \times 330 \mu m^2$ due to their size. The main benefit from the VFT was the improved sensitivity in $10^\circ < \theta < 23^\circ$ improving the total efficiency of the DELPHI vertex detector.

The inner detector (ID)

The inner detector was a combination of a drift chamber and a multi-wire chamber with five layers. The drift chamber was positioned around the VD and hence had a bigger distance to the beam pipe compared to the VD. Its cylindrical shape was 46 cm in diameter and consisted of 24 sectors with 24 signal wires each, which could be used to assist in reconstructing tracks. The wire chamber consisted of five cylindrical layers with 192 straw tubes⁹ of 8 mm size each.

The ID covered an angular area of $\theta > 15^\circ$ with a resolution of $40 \mu m$ in $R\phi$ and approximately $1.2 mrad$ in θ . Therefore it was not very suitable for track reconstruction and its main purpose was fast triggering.

The time projection chamber (TPC)

The TPC was DELPHI's main tracking chamber with a length of 3.34 metres. Its ability to provide the longest coherent track pieces compared with the other subdetectors made it very important for track reconstruction. The chamber was made up of two cylindrical parts with an inner radius of 29 cm and an outer

⁸Very Forward Tracker

⁹proportional counters

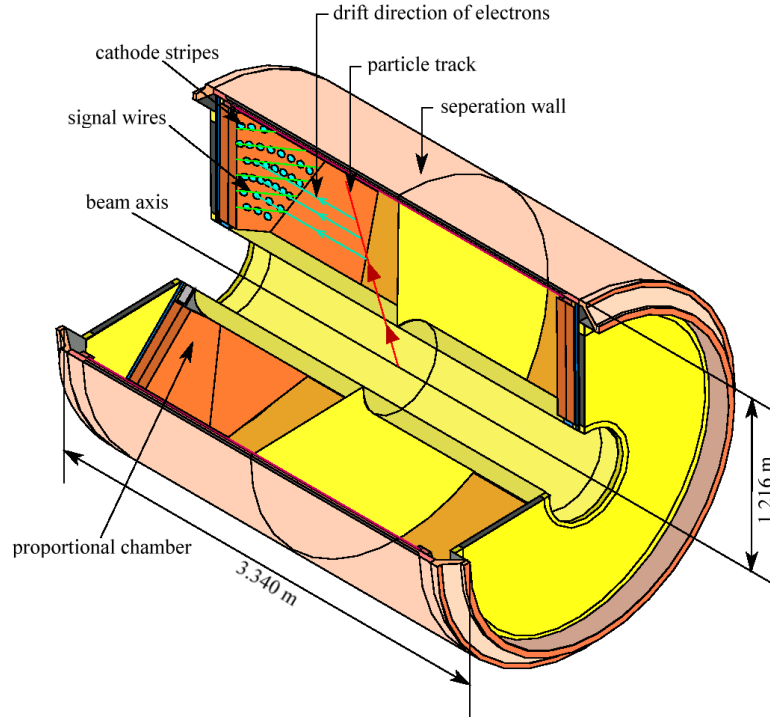


Figure 3.7: Scheme of the DELPHI time projection chamber (TPC).

radius of 1.22 m (see fig. 3.7). The cylindrical body was divided up in two parts by a separation wall creating two chambers with a drift field of $150 \frac{V}{cm}$ each. Each endcap was divided up in six sectors and contained a set of proportional counters in order to detect drift electrons. The $R\phi$ coordinate of a track was determined by the centre of charge on the cathode wires with a resolution of $150 \mu m$. For the z component the drift time of the electrons was used resulting in an accuracy of $900 \mu m$ in z . Finally the differential energy loss was used to provide particle identification due to their characteristic $\frac{dE}{dx}$.

The outer detector (OD)

The OD had a distance of approximately 2 m from the beam pipe and was the outer most subdetector still inside the superconducting solenoid. Due to its rather big distance from the beam pipe a good momentum resolution was achieved, which helped in reconstructing tracks. This subdetector consisted of 24 modules with 145 drift tubes each organized in five layers. Each tube had a length of 4.7 m and used a 4.4 kV field for operation. In total the OD had a length of 4.7 cm and provided a resolution of $100 \mu m$ in $R\phi$ and 4.4 cm in z direction. It covered an angular area of $\theta > 42^\circ$ and had a dead time of only 3 ns

making it a good trigger.

3.2.2 Calorimetric detectors

The electromagnetic calorimeter

The most important electromagnetic calorimeter in the barrel part of DELPHI was the HPC¹⁰. It was installed within the superconducting solenoid and consisted of 144 modules aligned in 6 rings with 24 modules each, covering an angular area of $\theta > 43^\circ$. The basic principle of the HPC is very similar to the TPC mentioned in the previous chapter. In addition several layers of lead were aligned around the drift chambers in order to start the electromagnetic showers. This resulted in an energy resolution (barrel part) of:

$$\frac{\sigma_E}{E} = \sqrt{\frac{(0.32)^2}{E[GeV]} + (0.043)^2} \quad (3.3)$$

In the endcaps, a separate electromagnetic calorimeter was used, the so-called FEMC¹¹. It consisted of 9064 lead-glass counters and covered an angular area of $8^\circ < \theta < 35^\circ$. Here the energy resolution was:

$$\frac{\sigma_E}{E} = \sqrt{\frac{(0.12)^2}{E[GeV]} + \frac{(0.11)^2}{(E[GeV])^2} + (0.03)^2} \quad (3.4)$$

The hadronic calorimeter (HAC)

The HAC subdetector was part of the solenoid iron joke with two endcap parts covering $11^\circ < \theta < 50^\circ$ and a barrel part covering $\theta > 43^\circ$. The detector tubes were aligned in 24 sectors in barrel and 12 sectors in the endcap regions. Each tube was separated by a 5 cm iron layer. The HAC provided an energy resolution of:

$$\frac{\sigma_E}{E} = \sqrt{\frac{(1.12)^2}{E[GeV]} + (0.21)^2} \quad (3.5)$$

3.2.3 Particle identification

The Cherenkov light detector (RICH)

This subdetector was making use of the Cherenkov effect, which occurs if a relativistic charged particle enters a dielectric medium with a velocity higher

¹⁰High density Projection Chamber

¹¹Forward Electro Magnetic Calorimeter

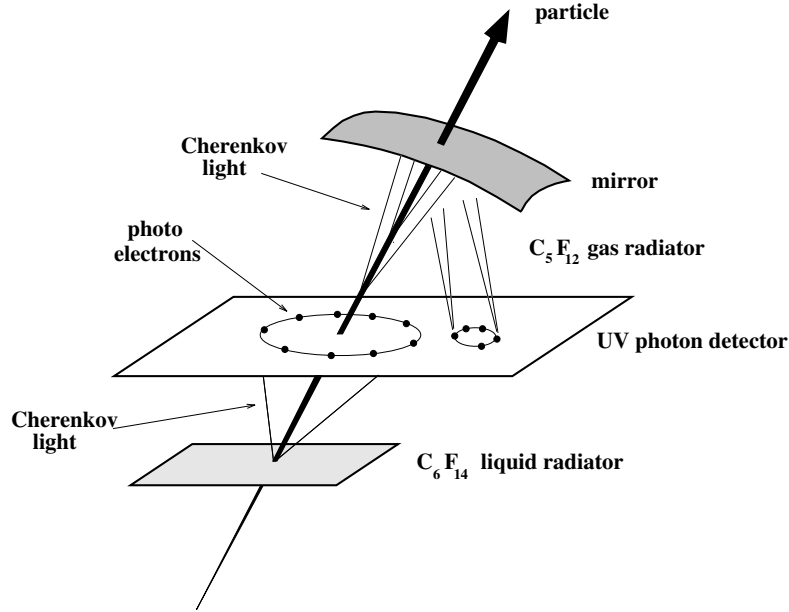


Figure 3.8: Scheme of the RICH-subdetector.

than the speed of light in this medium. A charged particle in a dielectric medium causes a cloud of dipoles in its vicinity. For particles propagating at a speed far below light this cloud has a spherical shape and the global charge is zero, since the dipoles neutralize each other. However this is not true for particles traveling at velocities beyond the light speed of the corresponding medium. Here the electromagnetic interaction, which propagates at the light speed of the medium, is overtaken by its source (the charged particle). As a consequence, dipoles behind this particle are effected by the electromagnetic interaction, whereas dipoles in front are not. Therefore the dipoles do not neutralize each other anymore and emit a Cherenkov light cone with an opening angle depending on the momentum and mass of the charged particle:

$$\cos(\theta) = \frac{1}{n} \sqrt{1 + \left(\frac{M}{p}\right)^2} \quad (3.6)$$

Here n represents the refraction index of the medium, θ is the measured opening angle while M and p are invariant mass and the measured momentum of the particle traversing the subdetector. Having knowledge of opening angle, momentum and refraction index one can easily calculate the invariant mass of the particle and hence identify it.

The DELPHI RICH¹² subdetector was designed to take advantage of this effect. Again there were two forward parts (FRICH¹³) and a barrel part (BRICH¹⁴). The detector in the middle part had two different radiators covering the angular area $\theta > 40^\circ$. The liquid radiator was used for particles with momenta between 0.7 and $8 \frac{\text{GeV}}{c}$, while the gas radiator was most sensitive between 2.5 and $25 \frac{\text{GeV}}{c}$. A mirror system was used to reflect the Cherenkov photons of liquid and gas radiator into the drift chamber, where the detection took place.

The muon chambers

Muons are the only charged particles which are able to traverse the detector without getting stopped by the detector material. For that reason the DELPHI muon chambers were installed as far away as possible from the beam pipe (between 4.5 and 5.3 m). Here also barrel chambers (MUB¹⁵) and forward chambers (MUF¹⁶) existed. They both worked like drift chambers providing a resolution of 4 mm in $R\phi$ and 2.5 cm in z-direction. In order to close detection gaps between MUB and MUF additional surrounding chambers (SMC¹⁷) were installed in 1994.

3.2.4 The offline system

The raw data taken by the detector had to be further processed and analysed. This was done by DELANA¹⁸ a DELPHI specific program which did a step by step analysis:

- first all subdetector responses were analysed and calibrated resulting in track fragments and energy informations for each subdetector
- next DELANA tried to merge the different track informations in order to get the complete track of a particle
- after having removed ambiguities, all tracks were extrapolated through the whole detector and calorimetric informations were added
- finally the primary vertex was reconstructed and all results were stored on DST¹⁹[Sac94]

¹²Ring Image Cherenkov counters

¹³Forward Rich

¹⁴Barrel Rich

¹⁵Muon Barrel

¹⁶Muon Forward

¹⁷Surrounding Muon Chambers

¹⁸DELphi ANALysis program

¹⁹Data Summary Tape

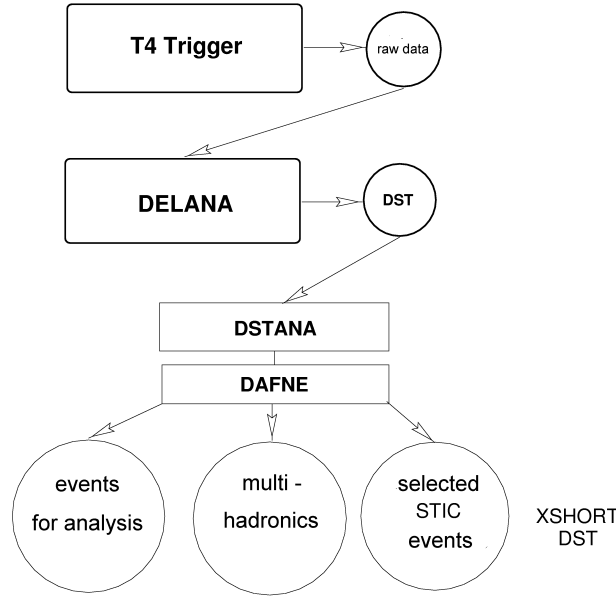


Figure 3.9: Illustration of the data processing chain.

The DST files contained all physically relevant informations like momentum, energy, detector informations, etc. The amount of storage necessary for a multi-hadronic event was only 60 KByte, whereas the same event saved in raw format would have needed approximately 150 KByte. Later the so-called XShort-DST²⁰[Spa97] format was introduced which lead to a further reduction in storage capacity needed.

²⁰EXtended Short DST

Chapter 4

Event simulation using Monte Carlo generators

This chapter deals with the simulation of the different high energy events needed in order to compare data with theoretical expectations and to search for new physics. A good understanding of the background processes and their uncertainties is of high importance for both: measurement and search analyses.

At LEP a huge variety of different processes and interactions occurred, each contributing according to its cross-section, which is highly energy dependent (see fig. 4.1). In the following sections the most important channels for the analyses presented in this thesis and their simulation using Monte Carlo techniques will be discussed.

In general all MC simulations of processes at LEP are set up in four phases (see also Fig. 4.2). The difference in simulating each channel happens mainly in phase I, where the initial partons are created. Hence the description of this first simulation channel will be very detailed, as it will be used as a reference for all other processes described later. These four phases are:

- I generation of primary partons and initial state radiation
- II perturbative description of gluon emissions and building of final partons
- III non-perturbative description of fragmentation and building of hadrons
- IV decay of unstable hadrons

The mentioned initial state radiation (ISR) only occurred during the LEP II phase at high energies, when the electron-positron-pair energy is lowered to m_Z energy by emitting photons. This process is also known as "radiative return" to m_Z .

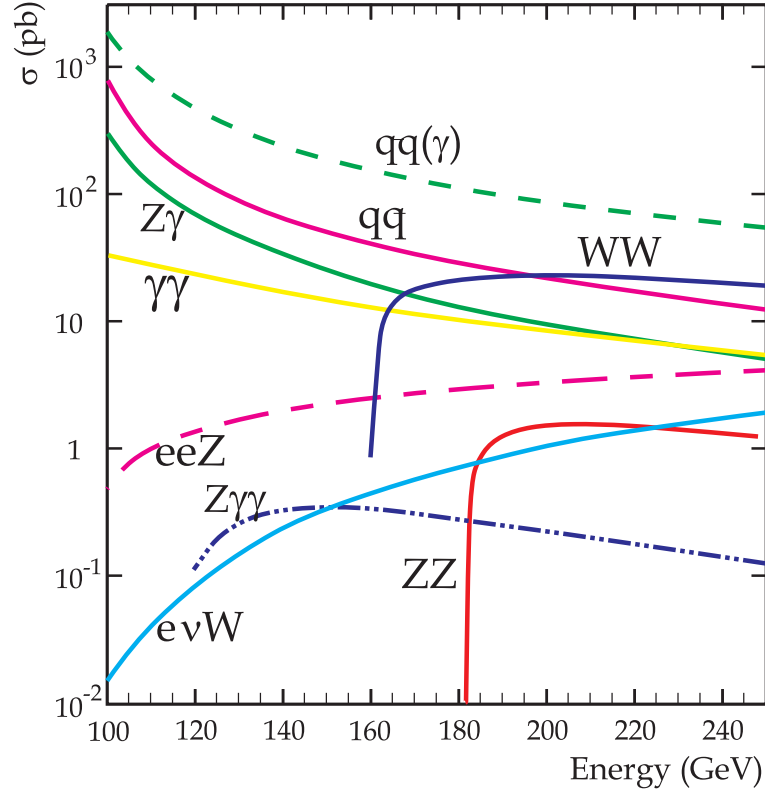


Figure 4.1: Illustration of the different processes and their cross-sections depending on the centre-of-mass energy.

4.1 Simulation of two-fermion processes

Two-fermion processes can be produced via a Z^0 boson or a photon, whereby the last process is strongly suppressed at LEP I and LEP II energies due to the higher cross-section of the Z^0 channel.

The Z^0 boson can decay hadronically into quarks ($q\bar{q}$) as well as into leptons (l^+l^- or $\nu_l\bar{\nu}_l$) with the corresponding branching ratios shown in table 4.1. In the case of electrons and muons the simulation ends after phase I, since these leptons do not interact strongly (no gluon emissions) nor do they fragment or decay within the detector. For tau leptons the situation is a bit different, however.

$Z^0 \rightarrow l^+l^-$	\approx	10.1	%
$Z^0 \rightarrow \nu_l\bar{\nu}_l$	\approx	20.0	%
$Z^0 \rightarrow hadrons$	\approx	69.9	%

Table 4.1: Branching ratio of Z^0 -bosons

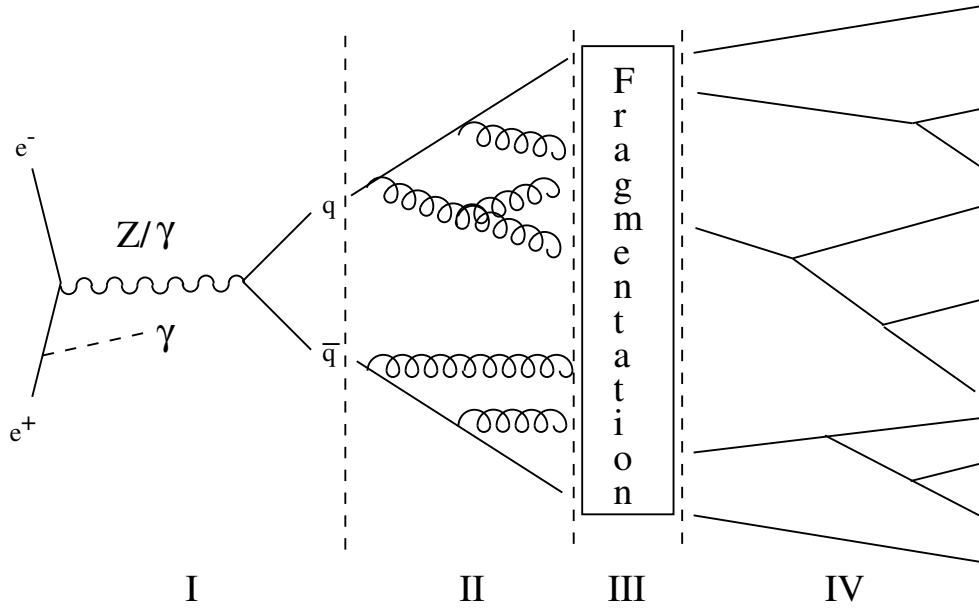


Figure 4.2: Overview of hadronic Z^0 decays and their description in MC generators.

They do interact weakly like the muon, but their short lifetime makes them decay leptonically or hadronically via a W^\pm boson within the detector.

The leptonic decay channel into l^+l^- only contributes 10% to the total amount of decays. Due to their weak interaction with matter, neutrinos can only be measured indirectly as they escape undetected. Most Z^0 bosons (70%) decay hadronically, leaving typically a two-jet signature in the detector. The implementation of hadronic decays and their subsequent processes will be described in detail here.

4.1.1 $e^+e^- \rightarrow q\bar{q}$ (phase I)

This electroweak part of the two-fermion processes is described by a perturbative ansatz. At Born-level and neglecting fermion masses one obtains the following cross-section [Heb92]:

$$\sigma(e^+e^- \rightarrow q\bar{q}) = N_c \frac{4}{3} \pi \alpha^2 \left[\frac{Q_e^2 Q_q^2}{s} + \right. \quad (4.1)$$

$$(V_e^2 + A_e^2)(V_q^2 + A_q^2) |\chi|^2 + \quad (4.2)$$

$$\left. 2 Q_e Q_q V_e V_q \Re(\chi) \right] \quad (4.3)$$

$$\text{with } \chi = \frac{1}{4 \sin(\theta_W)^2 \cos(\theta_W)^2} \cdot \frac{s}{s - M_Z^2 + i M_Z^2 \Gamma_Z} \quad (4.4)$$

Here N_c represents the amount of flavours, α the QED coupling constant and Q the charge. The vector and pseudo-vector couplings are symbolized by V and A respectively. One can divide up the whole equation into three parts. The first part (equation 4.1) describes the photon exchange, the second part (equation 4.2) describes the exchange via Z^0 and finally the third part (equation 4.3) represents the interference term between photon and Z^0 .

For small centre-of-mass energies the electromagnetic part (4.1) dominates due to its $\frac{1}{s}$ structure. At higher energies the two other parts become dominant and lead to the well known resonance peak at m_Z energy.

4.1.2 Building of final partons (phase II)

The primary quark anti-quark pair produced in phase I starts to emit part of its energy in form of gluon radiation. These may split into further gluons or $q\bar{q}$ pairs (so-called gluon splitting). Emitted gluons can be either soft, which means a small angle between gluon and emitting particle, or hard, which results in a bigger angle. Hard gluons usually lead to three-jets during jet clustering.

There are three different models to simulate gluon emission in MC generators. Each one has advantages and disadvantages concerning CPU-time and precision. The following description only provides an overview. Further details can be found in [Sjö93] and [Lön92].

Matrix-elements (ME) method

This is a perturbative description of the gluon emissions during partonisation. Matrix-elements are calculated in leading and next-to-leading order up to $\mathcal{O}(\alpha_s^2)$. However, a fully perturbative description is not possible, since the strong coupling constant is greater than 1 for small energies, which prevents the perturbation calculation from converging. Therefore one only takes into account energies above a certain threshold, usually at 1 GeV. An overview of the Feynman-graphs taken into account is shown in Fig. 4.3.

As one only uses correction-terms up to second order in α_s , not more than four partons can be generated. This sets the limit of possible jets reconstructed at parton level to four. As a consequence the four-jet relevant process

$$e^+e^- \rightarrow qgg\bar{q} \quad (4.5)$$

is calculated without any correction terms which renders the matrix-elements method a bad choice for describing QCD four-jets. The process which leads to three-jets

$$e^+e^- \rightarrow qg\bar{q} \quad (4.6)$$

however has a first order correction.

The first order differential cross-section for three-jets in the matrix-elements model assuming massless quarks has the following structure [Sjö93]:

$$\frac{1}{\sigma_0} \cdot \frac{d\sigma}{dx_q dx_{\bar{q}}} = C_F \frac{\alpha_s}{2\pi} \cdot \frac{x_q^2 + x_{\bar{q}}^2}{(1-x_q)(1-x_{\bar{q}})} \quad (4.7)$$

Here σ_0 represents the cross-section at Born level, C_F denotes a colour factor, while x_q and $x_{\bar{q}}$ have the meaning of parton-energies in their corresponding centre-of-mass frames. The divergences resulting from $x_{q,\bar{q}} \rightarrow 1$ are compensated by second order vertex- and propagator-corrections. The cross-section therefore is finite for all $x_{q,\bar{q}}$.

Parton-shower model

The parton-shower model[Sjö93] uses a so-called 'leading log approximation' (LLO) which means, that correction terms are only calculated up to the leading logarithm of the correction terms. The following processes are taken into account and their correction terms are summed:

$$q \rightarrow qq, g \rightarrow gg, g \rightarrow q\bar{q}, q \rightarrow q\gamma \quad (4.8)$$

Every parton emits in an iterative way new partons according to equation 4.8 until their invariant mass reaches a certain minimum. This minimum value is defined by the effective mass of the lightest possible daughter particle[Sjö93]:

$$m_{eff,g} = \frac{1}{2}Q_0 \quad (4.9)$$

$$m_{eff,q} = \sqrt{m_q^2 + \frac{1}{4}Q_0^2} \quad (4.10)$$

The cut-off value Q_0 is set in the program and depends very much on the used model. The probability of a parton splitting into two new partons according to equation 4.8 is defined by the *Altarelli-Parisi* equations:

$$dP_a = \sum_{b,c} \frac{\alpha_{abc}}{2\pi} P_{a \rightarrow bc}(z) dt dz \quad (4.11)$$

$$t = \ln \left(\frac{Q}{\Lambda} \right)^2 \rightarrow dt = d \ln(Q^2) = \frac{dQ^2}{Q^2} \quad (4.12)$$

Here α_{abc} represents the first order QCD running coupling constant. The four-momentum part of the mother-parton a which is transferred to the daughter-parton b is labeled as z . Consequently the second daughter-parton c receives

the $(1 - z)$ part. The splitting functions $P_{a \rightarrow bc}$ are defined separately for each process[Sjö93]:

$$P_{q \rightarrow qg}(z) = C_F \frac{1 + z^2}{1 - z} \quad (4.13)$$

$$P_{q \rightarrow q\gamma}(z) = e_q^2 \frac{1 + z^2}{1 - z} \quad (4.14)$$

$$P_{g \rightarrow gg}(z) = N_C \frac{(1 - z(1 - z))^2}{z(1 - z)} \quad (4.15)$$

$$P_{g \rightarrow q\bar{q}}(z) = T_R(z^2 + (1 - z)^2) \quad (4.16)$$

with $C_F = \frac{4}{3}$ and $N_C = 3$ (number of colours). The constant $T_R = \frac{n_f}{2}$ depends on the amount of flavours n_f allowed for this decay. Parameter e_Q^2 denotes the squared electrical charge of the quark, which is also flavour dependent.

Due to the fact, that the parton-shower approach uses a leading-log approximation for every splitting, these elementary processes are not well described compared to the matrix-elements method. Therefore the result of the first splitting is matched to the matrix-elements calculations. This so-called “matrix-element-matching” scales the beginning of the shower evolution to the more precise ME calculations. This is done by deriving a correction factor out of the differential three-jet cross-sections of ME (equation 4.7) and parton-shower model. The differential cross-section of the parton-shower model has the following form:

$$\begin{aligned} \frac{1}{\sigma_0} \frac{d\sigma_{PS}}{dx_q dx_{\bar{q}}} &= \frac{\alpha_s}{2\pi} C_F \frac{1}{(1 - x_q)(1 - x_{\bar{q}})} \cdot \\ &\left\{ \frac{1 - x_q}{x_g} \left[1 + \left(\frac{x_q}{2 - x_{\bar{q}}} \right)^2 \right] + \frac{1 - x_{\bar{q}}}{x_g} \left[1 + \left(\frac{x_{\bar{q}}}{2 - x_q} \right)^2 \right] \right\} \end{aligned} \quad (4.17)$$

This correction factor is applied to one of the two primary quarks. The other quark is treated as if it would not shower.

One effect has not yet been considered in this model. According to theoretical considerations, the gluon emissions must soften with every iterative step of the parton-shower. Consequently the emission angles have to decrease. To satisfy this condition all emissions are ordered according to their emission angles (angular ordering).

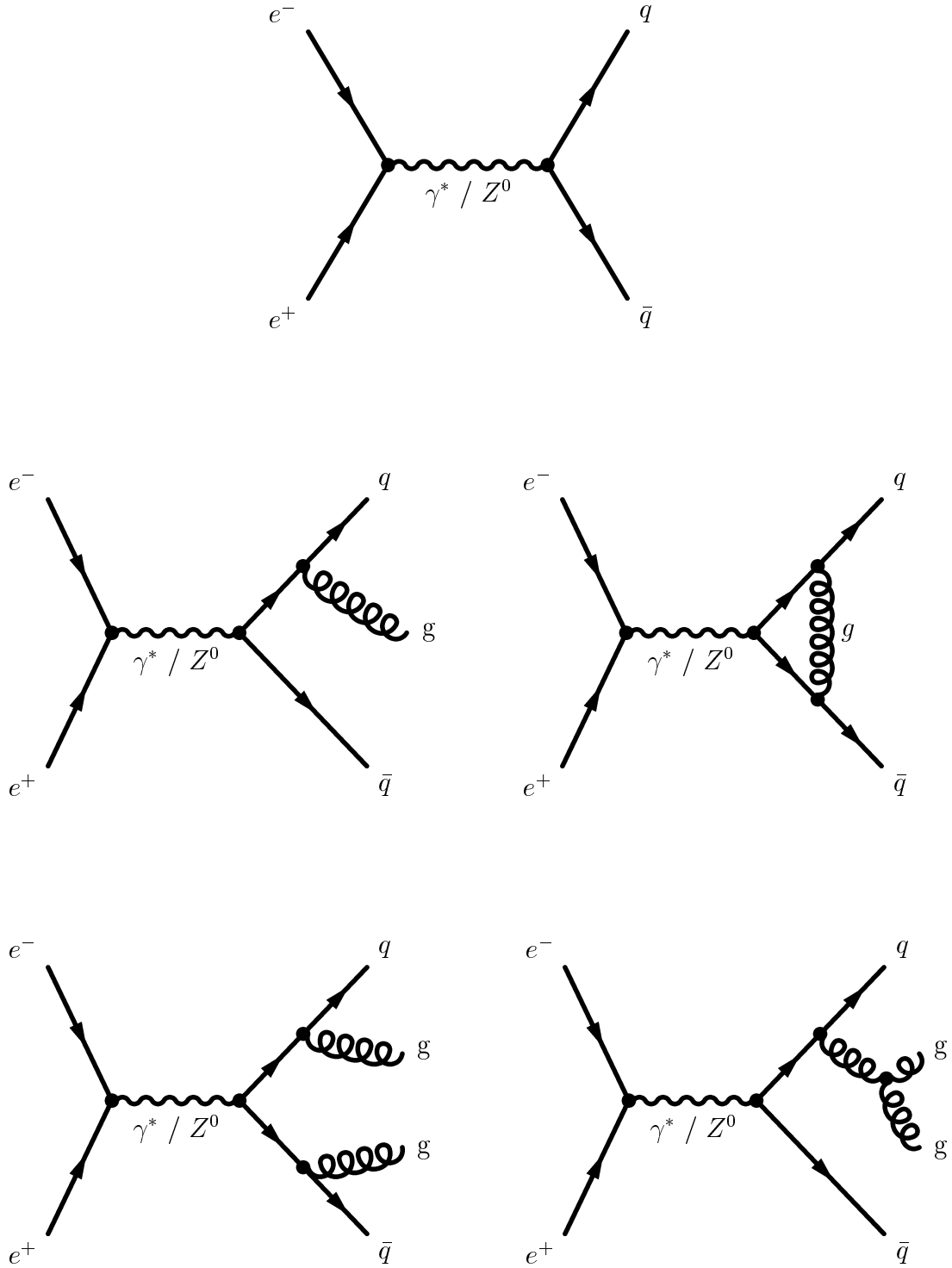


Figure 4.3: The upper Feynman-graph shows the process $e^+e^- \rightarrow q\bar{q}$ at Born-level. The diagram on the middle left shows a first order α_s correction, whereas the right one represents a vertex-correction. The two lower diagrams show second order corrections.

Colour-dipole model

This model also produces a shower of emitted partons, but here every parton pair is treated as a colour dipole. The gluon emissions take place in analogy to electromagnetic dipole emissions in QED. Due to the fact that gluons carry a colour, there exist three possible colour-dipole configurations: $q\bar{q}$ -dipoles, qg -dipoles and gg -dipoles. The corresponding Feynman-graphs are shown in Fig. 4.4.

Every dipole configuration has its own differential cross-section which are shown below assuming massless quarks:

$$\frac{d\sigma_{q\bar{q}}}{dx_q dx_{\bar{q}}} = \frac{2\alpha_s}{3\pi} \cdot \frac{x_q^2 + x_{\bar{q}}^2}{(1-x_q)(1-x_{\bar{q}})} \quad (4.18)$$

$$\frac{d\sigma_{qg}}{dx_q dx_g} = \frac{3\alpha_s}{4\pi} \cdot \frac{x_q^2 + x_g^3}{(1-x_q)(1-x_g)} \quad (4.19)$$

$$\frac{d\sigma_{gg}}{dx_g dx_g} = \frac{3\alpha_s}{4\pi} \cdot \frac{x_g^3 + x_g^3}{(1-x_g)(1-x_g)} \quad (4.20)$$

Again x represents the partonic energy scaled to the centre-of-mass energy of the dipole. If the quark-mass is taken into account, equations 4.18 and 4.19 have to be modified accordingly[Lön92].

The already mentioned angular ordering is also of importance to this model and is implicitly achieved by preferring gluon emissions with decreasing transverse momentum (p_t):

$$p_t^2 = S_{Dip} \left(1 - x_1 + \frac{m_1^2 - (m_2 + m_3)^2}{S_{Dip}} \right) \cdot \left(1 - x_3 + \frac{m_3^2 - (m_2 + m_1)^2}{S_{Dip}} \right) \quad (4.21)$$

The so-called “Sudakov-form-factor” [Lön92] adjusts the probability for a gluon emission at a given p_t . Since gluons are treated as massless, some masses in equation 4.21 become zero. The square of the dipole centre-of-mass energy is expressed by S_{Dip} in 4.21.

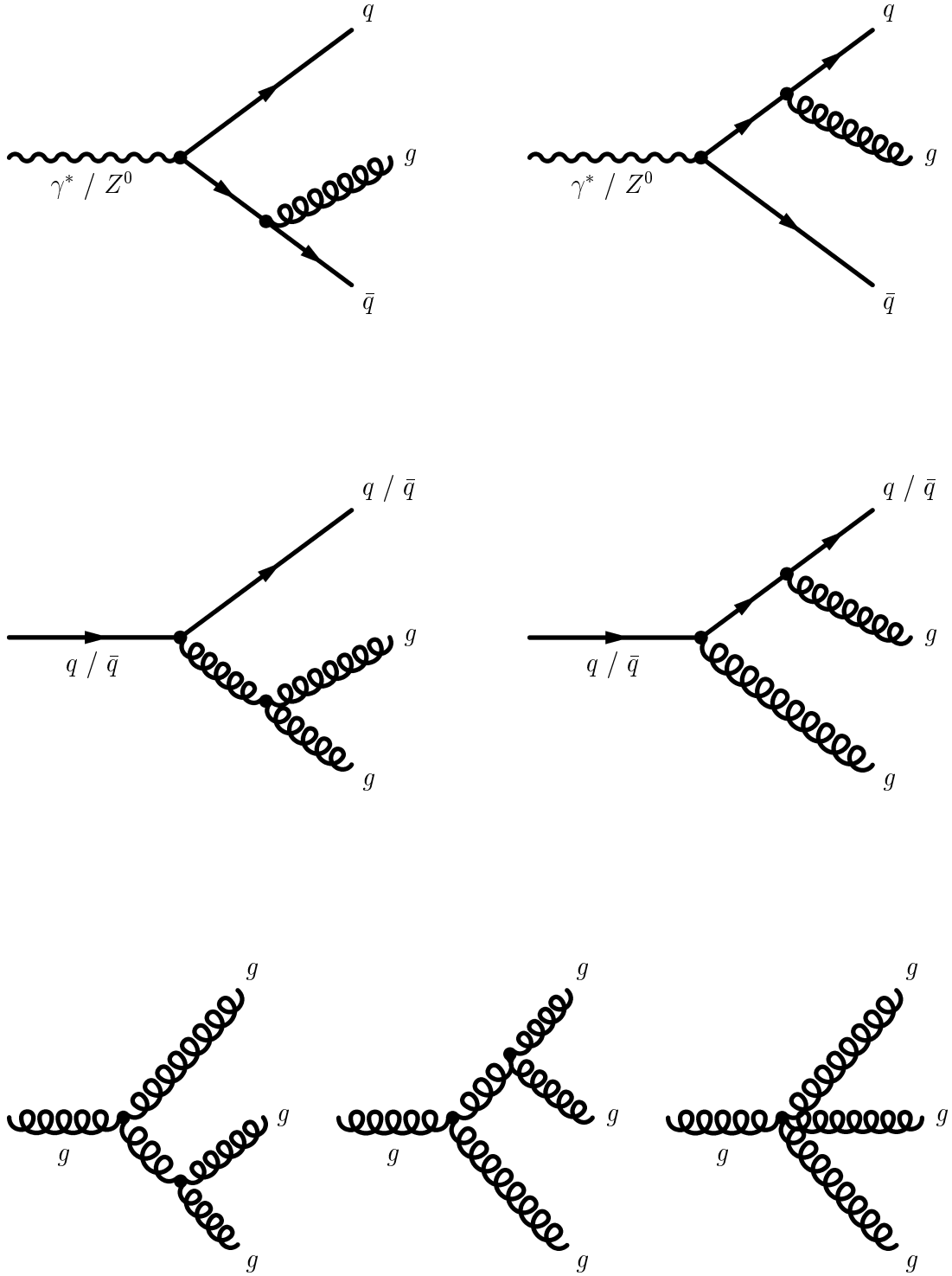


Figure 4.4: Feynman-graphs considered in the colour-dipole model. The two upper plots show $q\bar{q}$ -dipoles, qg -dipoles are shown in the middle and three examples of gg -dipole emissions can be seen in the lower part of this figure.

4.1.3 Hadronisation (phase III)

During this phase, all partons charged with colour are combined to colourless hadrons. There exist more or less three different models which try to provide a non-perturbative description of the fragmentation. Right after the gluon emission in phase II all partons are relatively close together and behave like free particles. Due to their kinematics, these particles disperse and thus α_s increases. Consequently, α_s is not negligible compared to one any more and thus a perturbative description of the fragmentation process is not possible. This can be expressed in a corresponding potential depending on the relative distances:

$$V(r) = -\frac{4\alpha_s}{3r} + \sigma \cdot r \quad (4.22)$$

For small distances the first part of equation 4.22 dominates. Here only few gluons are exchanged between the partons and a $\frac{1}{r}$ -term similar to the electromagnetic potential dominates. As soon as distance r increases a gluon-string originates which is described by the second term of equation 4.4. The so-called “string-tension” σ of $0.9 \frac{\text{GeV}}{\text{fm}}$ causes the linear term to dominate the whole expression 4.4 for increasing r . Thus all quarks have to be bound to hadrons (quark confinement).

String-fragmentation

This model has been developed at the Lund University in 1980. The basic idea is to consider all gluons between a $q\bar{q}$ -pair as one string. Due to the possibility of multiple quark-pairs being produced, the amount of strings is not restricted to one only. Provided that sufficient energy is available a string can split into two strings by generating a new $q\bar{q}$ -pair out of the vacuum (see Fig. 4.5). This procedure is iteratively repeated until the string energy is not sufficient to build another quark-pair.

Quarks generated during the string-splitting are technically treated energy-less during their generation. Their final energy consists of the mass and the momentum transverse to the propagation of the initial quark-pair. Heavy quark production is suppressed during this process, because the quarks achieve their final mass by tunneling the energy difference:

$$\mathcal{P} \sim e^{-\frac{\pi(m_q^2 + p_t^2)}{\kappa}} \quad (4.23)$$

Hence the probability depends on the final mass and therefore on the flavour of the quark, leading to the following ratios:

$$d : u : s : c : b = 1 : 1 : 0,3 : 10^{-11} : 10^{-100} \quad (4.24)$$

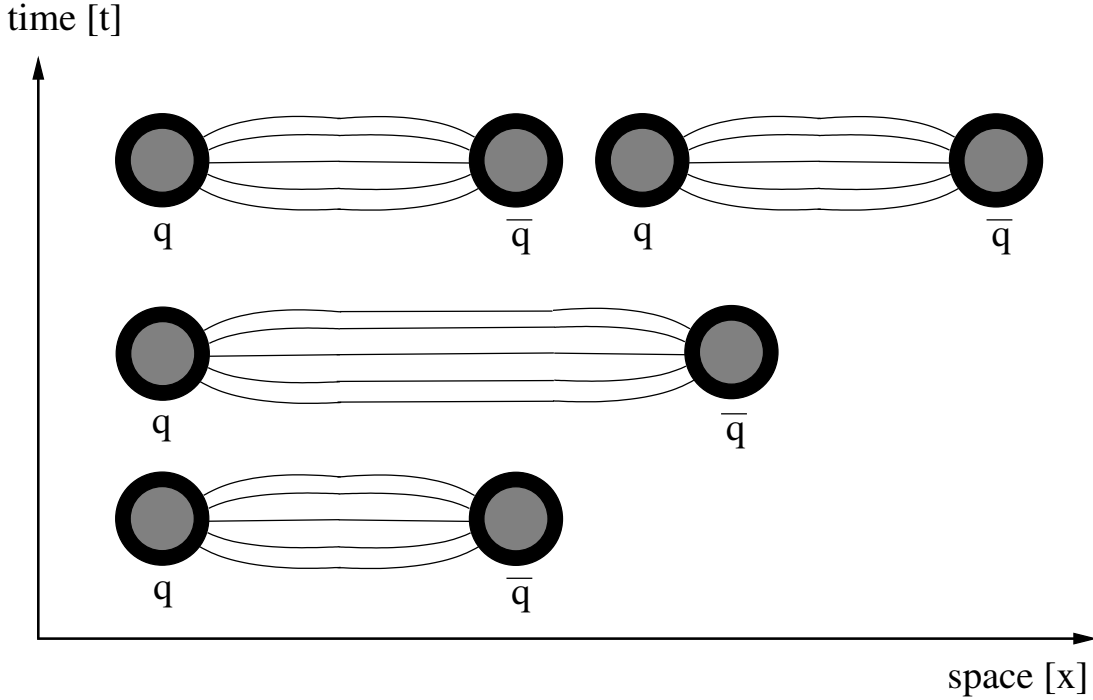


Figure 4.5: Schematic presentation of the string-fragmentation. One can see the two quarks separating and the string splitting into a new $q\bar{q}$ -pair, building a colourless hadron.

These values confirm, that c-quarks and therefore the even heavier b-quarks can hardly be generated during fragmentation. In most cases they emerge directly of the Z^0 . A second possibility is the gluon splitting into $c\bar{c}$ and $b\bar{b}$. But here the rates are quite low too (3.0% and 0.3% respectively).

Another important parameter of the string-fragmentation is z . This variable describes the fraction of $E + p_t$ taken by the daughter hadron during the fragmentation process. The Likelihood distribution for this variable is called the “fragmentation function” $f(z)$. For light quarks the symmetric LUND fragmentation function is used:

$$f(z) \sim \frac{(1-z)^a}{z} e^{-\frac{bm_t^2}{z}} \quad (4.25)$$

Here a and b are tuneable variables, the so-called “LUND fragmentation parameters”, whereas m_t describes the transverse mass. Light quarks do not take much energy from the string during fragmentation, hence they fragment “soft”. The more massive c- and b-quarks use up a considerable amount of energy and momentum and therefore they fragment “hard”. To describe the fragmentation of

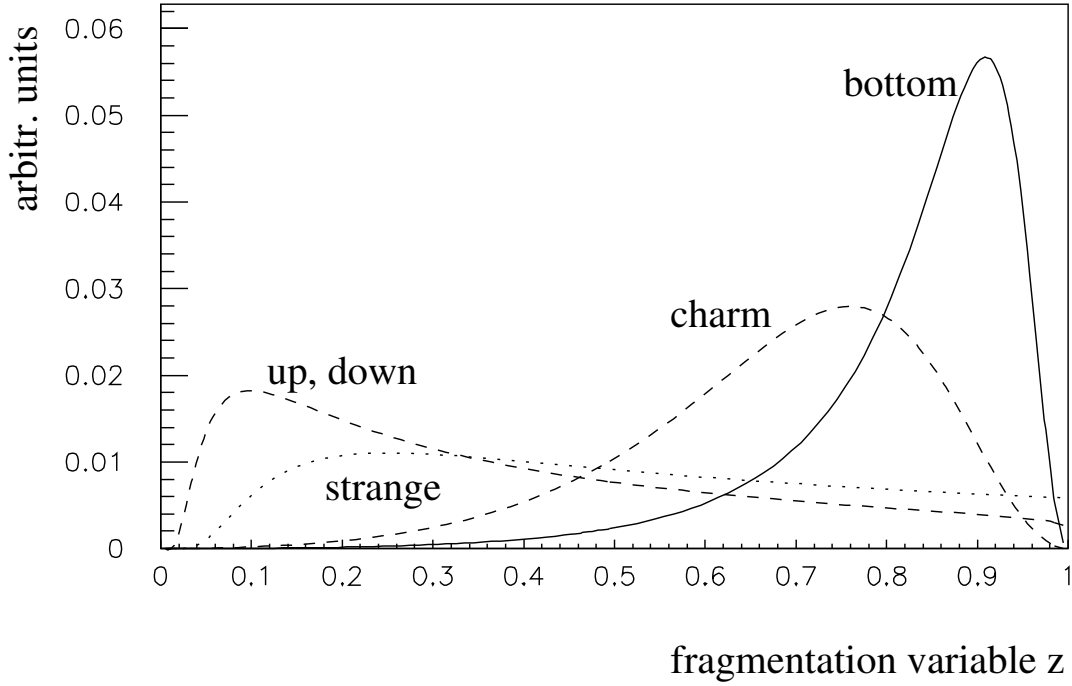


Figure 4.6: Overview of fragmentation functions depending on the variable z for every quark-flavour.

these particles one prefers the Peterson function.

$$f(z) \sim \frac{1}{z \left(1 - \frac{1}{z} - \frac{\epsilon_Q}{1-z}\right)^2} \quad (4.26)$$

The Peterson function has only one free parameter ϵ_Q . An overview of all quark-flavours and their description by the corresponding fragmentation function can be seen in Fig. 4.6.

The favorite model for hadronisation is the string-fragmentation. It provides the best agreement with data and also takes into account the string-effect, which describes the increased hadron production between qg and $g\bar{q}$ for 3 jet events. In addition there is no need for special scale factors as for the cluster-fragmentation. The drawback is its quite complex structure and the amount of parameters compared to the other models.

Cluster-fragmentation

Here all partons of phase II are grouped to colourless clusters. Every cluster is then treated separately by the fragmentation process. This results in two hadrons per cluster, except for very light and very heavy clusters which are treated

differently. Heavy clusters are split up into lighter ones before they fragment and light clusters only give one hadron.

To obtain a reasonable agreement with data, a cluster reweighting turned out to be necessary. This is one of the reasons why the cluster fragmentation is not used very often. A Monte-Carlo generator which makes use of this fragmentation model is Herwig[M⁺96]. A recent comparison, which has been performed doing a χ^2 -test[Kup98], confirms a less accurate description of data by the cluster fragmentation.

Independent fragmentation

This fragmentation model which has been introduced by Field and Feynman in 1978 is the oldest one. Here all partons hadronise independently from each other. Energy and momentum are derived from a fragmentation function but conservation of both is neglected. Therefore one has to apply additional corrections to conserve energy and momentum. Furthermore the string effect is not taken into account at all. These circumstances make the independent fragmentation a bad choice and consequently it is hardly used any more.

4.1.4 Decay of unstable hadrons (phase IV)

During this phase all hadrons marked unstable decay to stable and long living particles. Their decay is simulated in the following detector simulation. This chapter can only provide an overview. A more detailed description can be found in [Sjö93].

Branching ratios are known for many hadrons especially for the light ones and their momentum can be determined from phase-space. In some cases the phase-space is reweighted by a matrix-element expression. The situation is completely different for heavy charm-hadrons. Here a $V - A$ matrix-element is not sufficient to describe its decay. Thus a combination of different methods is applied. One possibility is to supplement known branching ratios by “plausible assumptions” in order to obtain a preferably complete decay table. In addition some extra hadrons can be generated by an iterative method similar to the already described fragmentation until a predefined multiplicity is reached. Finally some consistency checks concerning kinematic variables are applied.

Bottom-hadrons depend even more on the knowledge of branching ratios. Here, all hadrons not tabulated decay according to the so-called “spectator model”. In this model, the b-quark is treated as a free particle and all other quarks of the decaying hadron do not interact with it or with each other. They are treated as non-involved “spectators”. This process is performed for all hadrons in the same way. Of course it is not a very precise method.

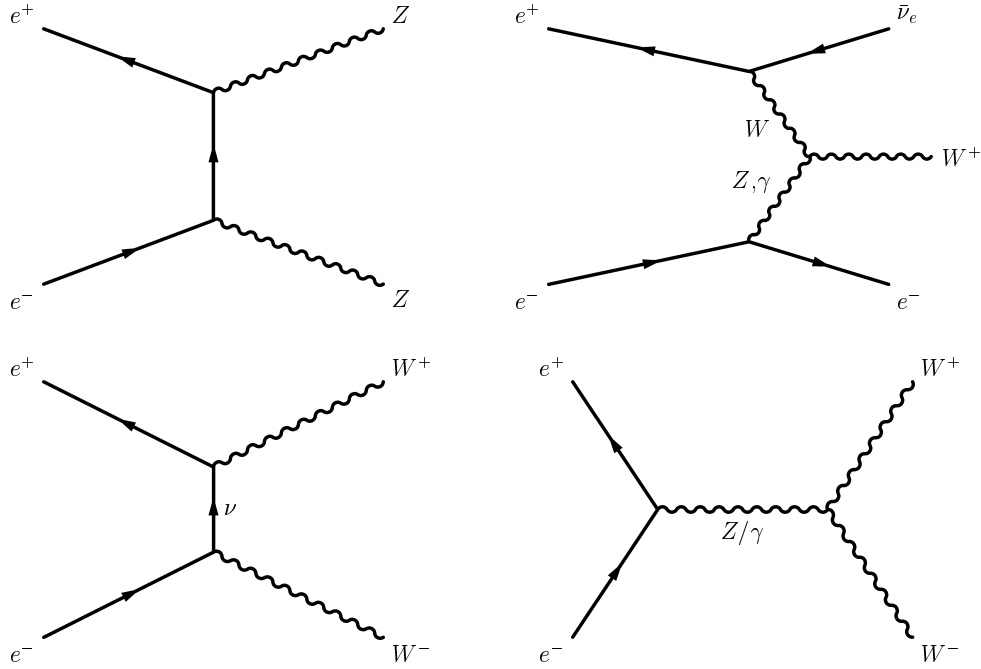


Figure 4.7: The three four-fermion channels contributing most to the total cross-section: neutral current Z pair production (upper left), $W e \nu$ (upper right) and W^+W^- production (two lower graphs).

4.2 Simulation of four-fermion processes

This category covers all processes with four-fermion final states in the electroweak part (phase I) of the simulation chain. The following partonisation, fragmentation and decays of unstable particles is performed in the same way by the same routines as for the two-fermion simulation.

One can further distinguish between charged current processes involving W^\pm bosons and neutral current processes exchanging Z^0 bosons. At LEP, a variety of s-channel and t-channel processes including leptonic and hadronic final states were belonging to these two classes, but only three of them contributed with significant cross-sections (see Fig. 4.7).

For simulating such processes two generators are quite commonly used within the DELPHI collaboration: EXCALIBUR[BPK95] and recently also WPHACT[AB97]. One of the main drawbacks of EXCALIBUR with respect to WPHACT is the missing implementation of the CKM matrix. This was one of the reasons, why the most recent four-fermion MC productions have been done using WPHACT. Another insufficiency of EXCALIBUR is its inability to simulate $W e \nu$ processes.

4.2.1 $e^+e^- \rightarrow Z^0 Z^0$

The threshold for Z^0 pair production is at 183 GeV, when the centre-of-mass energy is sufficient to produce two on-shell Z^0 bosons. Its cross-section raises very fast and reaches a plateau-like maximum of roughly 1 pb (see Fig. 4.1). This process is also referred to as NC02¹ since it belongs to the class of neutral current interactions and there are 2 contributing Feynman diagrams – the one shown in Fig. 4.7 and its mirror graph.

4.2.2 $e^+e^- \rightarrow W^+W^-$

Since the mass of a W boson is approximately 10 GeV below the mass of a Z, its production threshold is around 160 GeV. The cross-section reaches also very fast a plateau-like maximum, which is by a factor 20 higher compared to the Z^0 pair production, rendering the W^+W^- channel a difficult background. Three Feynman graphs are contributing to this CC03² channel, shown in the lower part of Fig. 4.7. The t-channel diagram on the lower left would lead to a divergent cross-section evolution, which is prevented by the two other s-channel contributions via Z^0 and γ respectively.

4.2.3 $e^+e^- \rightarrow W e \nu$

The cross-section of this four-fermion t-channel process may not be as high as for WW, but it has a property, which renders it a very difficult background source for channels focusing on missing energy. One of the two initial leptons is emitting a soft photon or an off-shell Z^0 boson (see Fig. 4.7 upper right part) which hardly changes kinematics of the emitted lepton, turning it into a spectator like particle. Consequently it will leave the detection area very close to the beam pipe of the detector, resulting in a high probability of escaping undetected and hence leading to a missing energy signature.

4.3 Simulation of two-photon and Bhabha processes

Events resulting from these two processes are quite easy to select and hence they only play a minor role as background source for missing energy analyses. But their

¹Neutral Current 02

²Charged Current 03

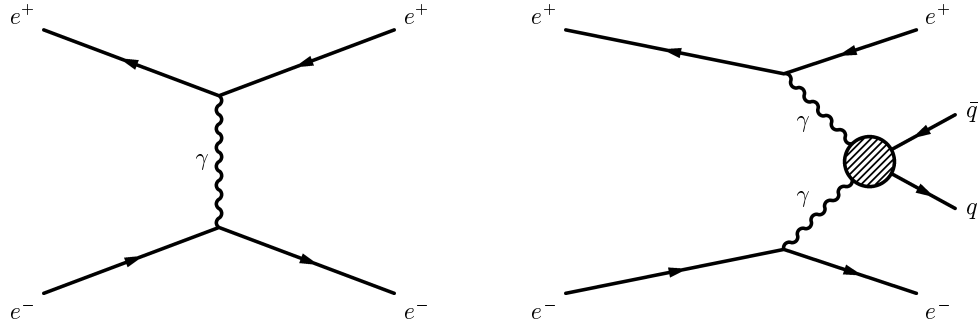


Figure 4.8: The diagram on the left hand side shows the Bhabha scattering process, while the one on the right hand side represents the two-photon interaction. The shaded vertex stands for the three different models used to describe the generation of the quark pair.

extraordinary high cross-sections (several nanobarn) makes the implementation in MC simulation worth mentioning.

Two-photon processes are not easy to simulate and three different models are used to describe the properties of the hadronic production shown in Fig. 4.8.

- QPM-model: describing a point like photon-photon interaction
- QCD-model: using a partonisation model including gluon radiation
- VDM-model: partons are treated similar to vector mesons. Used to simulate soft emissions.

Since the whole system tends to be boosted in forward direction, soft emissions can lead to convergence problems in the perturbative description. This makes an ansatz using three different models necessary.

In the past, two different generators had to be used in order to cover all three models. Recently the description of such processes has been significantly improved in the latest versions of the Pythia MC simulation package[Sjö93]. Therefore the latest samples have been produced using Pythia.

The Bhabha scattering process (see Fig. 4.8 left hand side) is characterised by its simplicity and a very high cross-section. Typically events resulting from this process have only few reconstructed tracks and hence they can be quite easily separated and discriminated.

4.4 Detector simulation

Main purpose of the detector simulation is the reconstruction of the detector response, providing the possibility to directly compare simulated events with real data. The program to simulate the DELPHI detector is called DELSIM[DEL89]. It has to be constantly updated and separated calibrations for each year of data taking have to be applied. The last step is necessary in order to keep track of the constant change of each subdetector's efficiency and operational status. The whole simulation chain can be outlined by three steps:

- Event simulation at generator level. Here the generators introduced in the last sections are used and their results are written to a file for later processing by DELSIM.
- Simulation of the detector response. Now each particle's track through the "virtual" detector is simulated taking into account interactions with the detector material like photo-effect, Compton-scattering, multiple-scattering, etc.
- Simulation of the subdetector responses. In this phase the read-out of each subdetector, if hit by a particle, is simulated by calling a separate program. This modular structure helped simplifying the maintenance of DELSIM.

Since the last two steps are very CPU intensive, detector simulations in general require powerful computer clusters.

Chapter 5

Analysis tools and techniques

In this chapter, commonly used tools and techniques for analyzing and classifying data samples shall be discussed. Since only methods applied in this thesis are presented here, the reader is referred to a more general overview found in [Cow98] or [Lyo86] for example.

5.1 Jet clustering

Jets[Sjö93] give important hints for event classifications. They are determined by grouping tracks with similar energy and momentum to so-called “clusters”. Monte-Carlo generators initially treat every stable hadron as a cluster. Then for every cluster the closest cluster nearby is searched according to a predefined distance definition. If the distance measured between two clusters falls below a predefined minimal value, both clusters are joined and form a new cluster. This process is repeated iteratively until no cluster falls below the set minimal distance or until a desired amount of clusters is generated. These final clusters form the so-called “jets”.

Basically there are two very common methods to describe the distance between two clusters. One is based on the square of the invariant mass:

$$m_{i,j}^2 = (E_i + E_j)^2 - \left(\vec{P}_i + \vec{P}_j\right)^2 \quad (5.1)$$

Here i and j represent two adjacent clusters. However, this method has some drawbacks:

If the particles (or clusters) only have small momenta, this results in small values for $m_{i,j}$. Consequently slow particles are clustered first, what in some sense contradicts to what one would expect: slower particles should be clustered around faster ones. Also the description of two-jet events therefore leads to some

problems [Sjö93]: In a typical two-jet event, particles with high momentum can be found near the jet axis. Consequently the slowest particles will form a separate cluster which then has to be joined with one of the two others to build the final two-jet structure. This results in one jet being forced to contain all particles with low momenta.

Another approach which does not depend that much on the absolute value of particle momenta can be achieved by using the transverse momentum instead. Pythia provides its own cluster algorithm using a method based on transverse momenta called LUCLUS[Sjö93]. This routine, JADE[JB⁺86] and DURHAM[DY⁺91] are the three most commonly used cluster algorithms in e^+e^- environments. Two other examples which will not be discussed any further are the Cone- and the Cambridge-algorithms.

5.1.1 LUCLUS

LUCLUS has been developed at the university of Lund[Sjö83]. Its distance parameter $d_{i,j}$ is based on the transverse momentum between particle i and j and can be expressed in the following way:

$$d_{i,j}^2 = \frac{4 |\vec{p}_i|^2 |\vec{p}_j|^2 \sin^2(\frac{1}{2} \theta_{i,j})}{(|\vec{p}_i| + |\vec{p}_j|)^2} \quad (5.2)$$

Assuming small angles $\theta_{i,j}$ expression 5.2 can be simplified by approximating $2 \sin(\frac{1}{2} \theta_{i,j}) \approx \sin(\theta_{i,j})$ and $\cos(\theta_{i,j}) \approx 1$:

$$d_{i,j} \approx \frac{|\vec{p}_i \times \vec{p}_j|}{|\vec{p}_i + \vec{p}_j|} \quad (5.3)$$

Here the cut-off value for $d_{i,j}$ is called d_{join} . The clustering takes place as described above by using the distance parameter just defined. To improve the algorithm and in particular the determination of jet-energy and momentum every new cluster is checked for misassociated particles. In such a case, a redistribution of the affected particles is performed. This results in a higher amount of CPU-time, because for every iterative step the particle configuration has to be checked and eventually changed. In order to reduce the amount of necessary computation, a so-called “pre-clustering”[Sjö93] is performed which reduces the number of initial clusters and therefore helps saving CPU-time. Unfortunately this step causes slightly different jet-rates compared to runs without a pre-clustering[BiG99] and hence it has been deactivated for the Monte-Carlo productions of DELPHI.

5.1.2 JADE

The JADE-algorithm uses a distance-definition related to the invariant mass. The iterative clustering steps are performed as already described in the begin-

ning of this section, although JADE doesn't do any checks for misassociated particles. Hence, energy and momentum cannot be determined as precisely as with LUCLUS. The distance variable used is defined as follows:

$$y_{i,j} = \frac{2 E_i E_j (1 - \cos \theta_{ij})}{E_{vis}^2} \quad (5.4)$$

Here the denominator E_{vis}^2 is only used for normalization. The cut-off value for $y_{i,j}$ is called y_{min} for this algorithm.

5.1.3 DURHAM

The DURHAM-algorithm is very similar to the JADE technique, although DURHAM uses the transverse momentum of the softer particle with respect to the more energetic one:

$$y_{i,j} = \frac{2 \min(E_i^2, E_j^2) (1 - \cos \theta_{ij})}{E_{cm}^2} \quad (5.5)$$

Here the cut-off value of $y_{i,j}$ is called y_{cut} and is usually chosen between 0.005 and 0.05. At the moment DURHAM is the official cluster algorithm used in DELPHI, but the other two are also very common.

5.2 Discriminant analyses techniques

A discriminant analysis in general is a method for classifying events exploiting topological characteristics. Its main purpose is to maximise the separation between several classes of events. In high energy physics typically two different classes are considered: background events and signal events.

Technically, this separation is achieved by constructing a discriminant variable such, that the mean values of each class get maximally separated, while the variance of each class gets minimized. A function taking both criteria into account can be easily constructed:

$$S(\mathbf{a}) = \frac{[M_1(\mathbf{a}) - M_2(\mathbf{a})]^2}{\Sigma_1^2(\mathbf{a}) + \Sigma_2^2(\mathbf{a})} \quad (5.6)$$

In equation 5.6 M_i represent the mean values of the two classes taken into account, while Σ_i^2 stand for the variances. Both depend on a set of parameters \mathbf{a} , which have to be determined from Monte Carlo simulation by maximizing $S(\mathbf{a})$, resulting in an optimal separation.

In the following two subsections the Fisher discriminant analysis[Fis36] will be explained first as an introduction to the iterated discriminant analysis, which was used to perform both analyses performed in this thesis.

5.2.1 Fisher discriminant analysis

The Fisher analysis defines its discriminant variable $D_{\mathbf{a}}(\mathbf{x})$ as linear combination of all input variables \mathbf{x} :

$$D_{\mathbf{a}}(\mathbf{x}) = \mathbf{a}^T \mathbf{x} \quad (5.7)$$

This results in a set of parameters a_i with i equivalent to the amount of input variables. In order to determine all parameters such that an optimal discrimination is achieved, mean M and variance Σ^2 have to be calculated from the discriminant variable distribution for both hypothesis (H_i , $i = 1, 2$) separately:

$$M_i = \int D f(D|H_i) dD \quad (5.8)$$

$$\begin{aligned} &= \int (\mathbf{a}^T \mathbf{x}) f(\mathbf{x}|H_i) d\mathbf{x} \\ &= \mathbf{a}^T \int \mathbf{x} f(\mathbf{x}|H_i) d\mathbf{x} = \mathbf{a}^T \mathbf{m} \end{aligned} \quad (5.9)$$

$$\Sigma_i^2 = \int [D - M_i]^2 f(D|H_i) dD \quad (5.10)$$

$$\begin{aligned} &= \int [\mathbf{a}^T \mathbf{x} - \mathbf{a}^T \mathbf{m}]^2 f(\mathbf{x}|H_i) d\mathbf{x} \\ &= \int [\mathbf{a}^T (\mathbf{x} - \mathbf{m})]^2 f(\mathbf{x}|H_i) d\mathbf{x} \\ &= \int [\mathbf{a}^T (\mathbf{x} - \mathbf{m})]^T [\mathbf{a}^T (\mathbf{x} - \mathbf{m})] f(\mathbf{x}|H_i) d\mathbf{x} \\ &= \int [\mathbf{a}^T (\mathbf{x} - \mathbf{m})(\mathbf{x} - \mathbf{m})^T \mathbf{a}] f(\mathbf{x}|H_i) d\mathbf{x} \\ &= \mathbf{a}^T \left[\int (\mathbf{x} - \mathbf{m})(\mathbf{x} - \mathbf{m})^T f(\mathbf{x}|H_i) d\mathbf{x} \right] \mathbf{a} \\ &= \mathbf{a}^T \mathbf{V} \mathbf{a} \end{aligned} \quad (5.11)$$

Mean M_i and variance Σ_i^2 of the final discriminant only depend on the means \mathbf{m} and Covariance matrix \mathbf{V} defined by the input variables. Both can be extracted easily from a set of MC simulations modelling all input variable distributions for both hypotheses.

Equations 5.10 and 5.11 can now be applied to the criterium for maximum separation of signal and background defined in equation 5.6. The indices on vector \mathbf{m} and matrix \mathbf{V} stand for the two hypothesis considered (signal and

background).

$$S(\mathbf{a}) = \frac{[M_1(\mathbf{a}) - M_2(\mathbf{a})]^2}{\Sigma_1^2(\mathbf{a}) + \Sigma_2^2(\mathbf{a})} \quad (5.12)$$

$$\begin{aligned} &= \frac{[\mathbf{a}^T \mathbf{m}_1 - \mathbf{a}^T \mathbf{m}_2]^2}{\mathbf{a}^T \mathbf{V}_1 \mathbf{a} + \mathbf{a}^T \mathbf{V}_2 \mathbf{a}} \\ &= \frac{[\mathbf{a}^T (\mathbf{m}_1 - \mathbf{m}_2)]^T [\mathbf{a}^T (\mathbf{m}_1 - \mathbf{m}_2)]}{\mathbf{a}^T (\mathbf{V}_1 + \mathbf{V}_2) \mathbf{a}} \\ &= \frac{[\mathbf{a}^T (\mathbf{m}_1 - \mathbf{m}_2)] [(\mathbf{m}_1 - \mathbf{m}_2)^T \mathbf{a}]}{\mathbf{a}^T (\mathbf{V}_1 + \mathbf{V}_2) \mathbf{a}} \\ &= \frac{\mathbf{a}^T \mathbf{B} \mathbf{a}}{\mathbf{a}^T (\mathbf{V}_1 + \mathbf{V}_2) \mathbf{a}} \text{ with } \mathbf{B} = (\mathbf{m}_1 - \mathbf{m}_2)(\mathbf{m}_1 - \mathbf{m}_2)^T \end{aligned} \quad (5.13)$$

Now the resulting expression 5.13 has to be minimized using the variation principle by setting its derivative $\nabla S(\mathbf{a})$ equal to zero. This leads to an eigenvalue problem with λ standing for the eigenvalue and \mathbf{I} denoting the unity matrix:

$$[(\mathbf{V}_1 + \mathbf{V}_2)^{-1} \mathbf{B} - \lambda \mathbf{I}] \mathbf{a} = \mathbf{0} \quad (5.14)$$

Solving equation 5.14 results in a set of eigenvalues and eigenvectors. Since the eigenvalue can be interpreted as measure for the separation power of the corresponding eigenvector \mathbf{a} , only the solution with the highest eigenvalue λ is chosen.

$$\mathbf{a} = (\mathbf{V}_1 + \mathbf{V}_2)^{-1} (\mathbf{m}_1 - \mathbf{m}_2) \quad (5.15)$$

$$\lambda = (\mathbf{m}_1 - \mathbf{m}_2)^T (\mathbf{V}_1 + \mathbf{V}_2)^{-1} (\mathbf{m}_1 - \mathbf{m}_2) \quad (5.16)$$

The resulting set of coefficients \mathbf{a} can then be used to calculate the discriminant variable $D_{\mathbf{a}}(\mathbf{x})$ using equation 5.7. Background compatible events (hypothesis 1) will result in an lower value for $D_{\mathbf{a}}(\mathbf{x})$ than events with signal like signature (hypothesis 2).

In theory, an optimal separation between classes can be obtained from a so-called ‘‘Likelihood ratio’’, which is defined by the ratio of probability densities $f(\mathbf{x})$ for both hypothesis:

$$r(\mathbf{x}) = \frac{f(\mathbf{x}|H_1)}{f(\mathbf{x}|H_2)} \quad (5.17)$$

However, this requires full knowledge of the multidimensional probability density for all input variables, including correlations of any order. Given M bins and N input variables one would need to determine M^N parameters (see also [Cow98]), which renders this method impracticable for more than two variables. In case of the Fisher discriminant one can avoid such a problem. According to equation 5.15

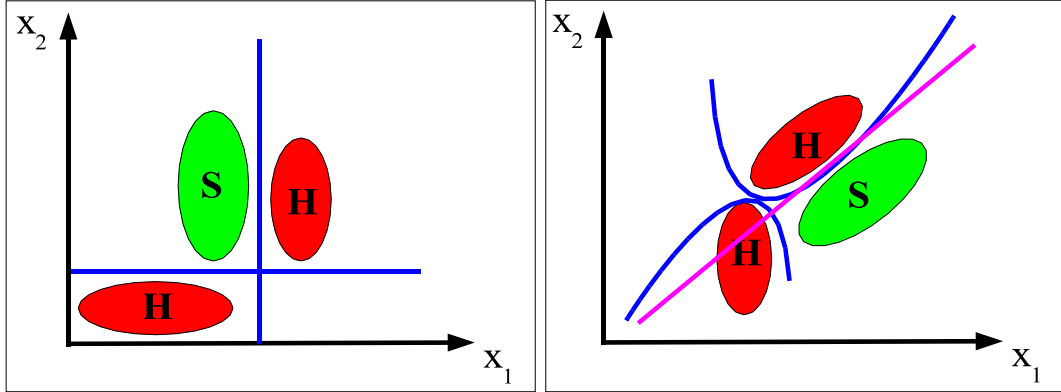


Figure 5.1: On the left hand side signal S and the two background sources H can be easily separated by two sequential cuts on variable x_1 and x_2 . This is not possible anymore for the example on the right hand side. Also the linear Fisher discriminant (straight line in grey) could not discriminate both background sources at once. But a non-linear approach, resulting in a pair of hyperbolas for this example, would be able to perform the distinction.

only mean \mathbf{m} and variance \mathbf{V} of the input variables need to be determined in order to calculate the set of coefficients \mathbf{a} .

It can be shown, that in the hypothetical case of perfect Gaussian input variables, the Fisher discriminant provides a class separation as powerful as the optimal Likelihood ratio 5.17. Hence, all input variables should be more or less Gaussian shaped in order to achieve an optimal separation. This can be achieved by for example taking the logarithm of input distributions, or by removing long tails with suitable cuts.

5.2.2 Non-linear and Iterated Discriminant Analyses

The previously discusses Fisher discriminant is using a linear combination of input variables to build its final discriminant variable. For just two input variables this corresponds to a straight line, separating the two-dimensional plane into two classes of events (see Fig. 5.1). However this method turns out to be not optimal, if one class (the background in this case) is composed of different event topologies populating different areas of phase space. On the right hand side of Fig. 5.1 such a situation is illustrated using two background areas (H) and one signal area (S). One clearly sees, that the grey straight line cannot separate both background areas from the signal region in the middle. Since LEP II high energy analyses very often face such a problem due to the variety of background channels contributing, a linear discriminant analysis can only provide limited discrimination.

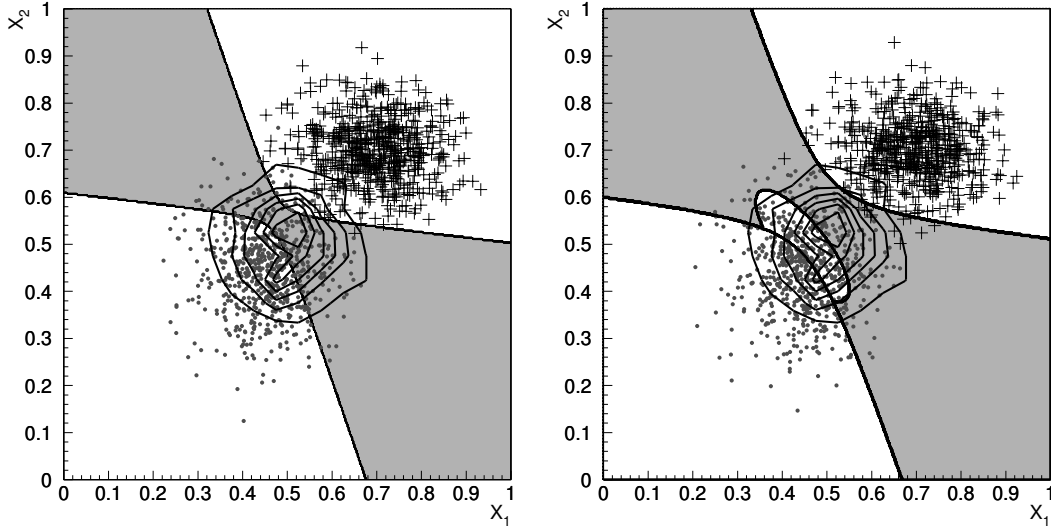


Figure 5.2: Non-linear discriminant analysis iteratively applied on a problem with two background sources (dots and crosses) and one signal area (contour lines)[Vol99]. The first iteration on the left hand side shows already a good discrimination. However the second iteration adds an ellipse, which improves discrimination against the background source close to the signal area (dots) at the same level of efficiency.

A very elegant method to compensate this weakness while keeping the advantages of the linear Fisher discriminant analysis is using a quadratic discrimination function instead of a linear one:

$$D_{\mathbf{a}}(\mathbf{x}) = \underbrace{\mathbf{a}^T \mathbf{x}}_{\text{lin. term}} + \underbrace{\mathbf{x}^T \mathbf{B} \mathbf{x}}_{\text{quadr. term}} \quad (5.18)$$

This expression can be transformed to look like its linear counterpart 5.7 by performing a linearization using the following substitutions:

$$\mathbf{a}' = (a_1, a_2, \dots, a_n, B_{11}, B_{12}, \dots, B_{nn})^T \quad (5.19)$$

$$\mathbf{x}' = (x_1, x_2, \dots, x_n, x_1 * x_1, x_2 * x_1, \dots, x_n * x_n)^T \quad (5.20)$$

Now the same criteria 5.7 as for the linear case can be applied and the set of coefficients \mathbf{a}' can be derived from mean and variances of the input variables. In the case of just two input variables such a discriminant corresponds to conic sections¹, trying to isolate signal from background (see Fig. 5.1).

In order to further improve the separation of background and signal, the discriminant analysis can be applied in an iterative manner. Technically, this can be

¹ellipses, parabolas or hyperbolas

realized by removing some of the background events with a cut on the discriminant variable resulting from the first iterative step, followed by a reoptimisation of the coefficients, resulting in the discriminant variable of the second iteration. Studies done by *Fritz Vollmer*[Vol99] lead to the conclusion, that in cases where background and signal are situated closely to each other in phase space, an iteration can improve the separation of the two classes. This is illustrated on Fig. 5.2, where on the left hand side the first iteration is shown, while on the right hand side the effect of the second iteration can be seen. Both plots show the selected signal region (grey area) at an efficiency of 52%, with an improvement in purity visible in case of the second iteration.

5.3 Artificial neural networks

Artificial neural networks (ANN) have a long tradition, which goes back to the late 50s. At that time, the first machines were developed, which tried to mimic the neural functionality of a human brain. In fact, structure and operation is quite similar to its biological counterpart and that is where the name and the initial inspiration came from. Our present knowledge and experience tells us, that an artificial neural net will never be able to provide the same functionality as a human brain, however it turned out to be a powerful tool for classification and pattern recognition purposes.

Technically, an ANN is very much related to the discriminant analyses techniques discussed in the previous section. In fact, a single layer perceptron (see Fig. 5.3) creates a test statistic $D(\mathbf{x})$ identical to the linear Fisher discriminant analysis (see equation 5.7) concerning separation power:

$$D(\mathbf{x}) = s(a_0 + \mathbf{a}^T \mathbf{x}) \quad (5.21)$$

The linear test statistics 5.21 has an additional offset a_0 and an activation function $s()$ compared to the Fisher discriminator. The activation function is usually a sigmoid or sigmoid-like function, which projects the output to a certain range of values (typically from -1 to 1). However, in the case of a single layer perceptron it does not add any discriminative power, since a sigmoid is a monotonic function. Finally, the offset a_0 can be used to adjust the working point by moving the argument of $s()$.

The most common ANN architectures are feed-forward multi layer perceptrons with one or even more hidden layers (see Fig. 5.3). In this iterative approach, the output results of the first iteration $h_i(\mathbf{x})$ from the hidden layer is then used as input for the second iteration resulting in a final output function $D(\mathbf{x})$:

$$D(\mathbf{h}(\mathbf{x})) = s(a_0 + \mathbf{a}^T \mathbf{h}) \quad (5.22)$$

$$\mathbf{h}(\mathbf{x}) = s(w_{i0} + \mathbf{W}^T \mathbf{x}) \quad (5.23)$$

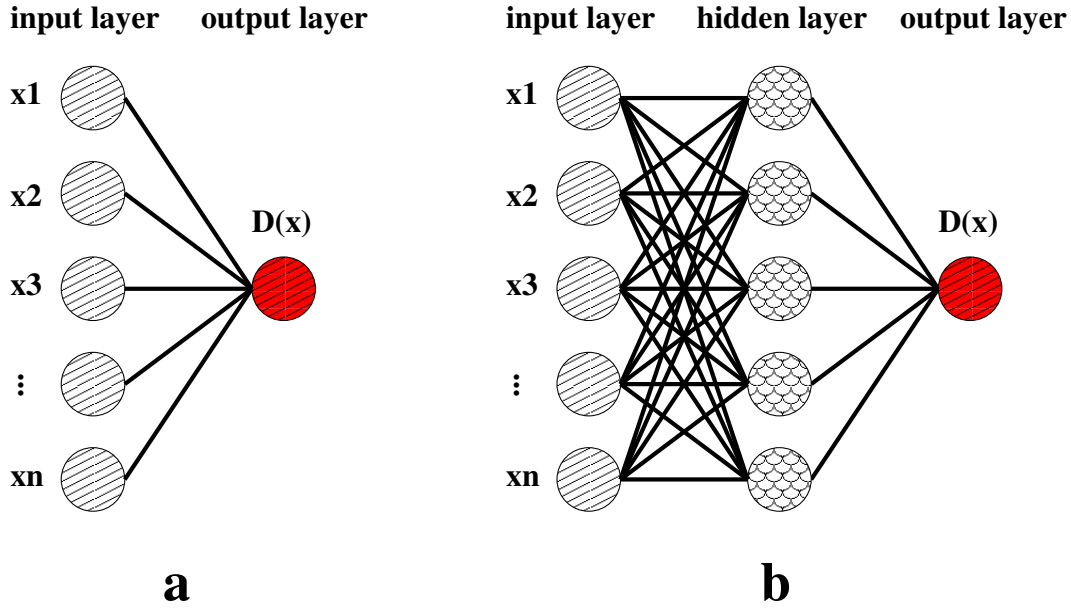


Figure 5.3: Two typical topologies of artificial neural networks. Architecture **a**: single layer perceptron, architecture **b**: two layer perceptron with a hidden layer.

Here the monotonic activation function $s()$ allows to generate any test statistics with just one hidden layer, making a neural net a very powerful classification tool.

Training such a network is done numerically by minimising an error function $E(D_i)$ defined as deviation from the preassigned target values (typically -1 for background and 1 for signal).

$$E(D) = \sum_{\text{events}} \underbrace{(D_1 - (-1))^2}_{\text{background}} + \underbrace{(D_2 - (1))^2}_{\text{signal}} \quad (5.24)$$

There exists a huge variety of minimisation algorithms with different optimisations concerning minimisation quality and CPU usage. Training a neural network is time consuming and there is always a risk of getting stuck in local minima, which weaken the discriminative power of an analysis. This is especially true, if the input variables are not properly preprocessed. On the other hand, a discriminant analysis also suffers from non-Gaussian input distributions, however training consumes considerably less time and there is no risk of getting stuck in a local minimum due to its analytic minimisation of the error function.

An artificial neural network package which tries to improve training while hardly suffering from the drawbacks mentioned above is “NeuroBayes” written by *Michael Feindt et. al.*[Fei01]. One of its key features is the preprocessing: all

input variables are linearly de-correlated and transformed to Gaussian distributions with variance one. This speeds up training and lowers the risk of getting stuck in a local minimum during minimisation of the error function.

5.4 Binned maximum Likelihood fit

The technique of maximising the total Likelihood of a hypothesis is mainly used to determine a set of parameters such, that the hypothesis becomes best compatible with the observed data. This is achieved by using the output of an analysis, isolating the signal hypothesis one would like to test. In the case of a discriminant analysis or neural net the corresponding final discriminant variable or network output can be used.

In general, a Likelihood function $L(\mathbf{a})$ is defined as a product of probability density functions (pdf) $f(x_i, \mathbf{a})$ coming from independent measurements:

$$L(\mathbf{a}) = \prod_{i=1}^n f(x_i, \mathbf{a}) \quad (5.25)$$

Here the observable x has been measured n times with its pdf depending on a set of parameters \mathbf{a} . These have to be chosen such, that $L(\mathbf{a})$ reaches a maximum. However, this leads to a problem numerically, since pdfs are by definition normalized to unity. Consequently taking the product of values $f(x_i, \mathbf{a}) \in [0., 1.]$ can rather soon exceed the numerical precision of the computer program used. An easy way to solve this problem is maximizing the logarithm of the Likelihood instead:

$$\mathcal{L}(\mathbf{a}) = \ln L(\mathbf{a}) = \sum_{i=1}^n \ln f(x_i, \mathbf{a}) \quad (5.26)$$

This leads to a sum instead of a product, which does not bear the risk of running into precision problems.

Analytically, the maximum can be found by asking the gradient to be zero. This criterium is sufficient due to the parabolic shape of $\mathcal{L}(\mathbf{a})$:

$$\nabla \mathcal{L}(\mathbf{a}) = \mathbf{0} \quad (5.27)$$

The corresponding error matrix E_{ij} can be derived by inversion from the Hesse matrix H_{ij} , which is build up by partial second derivatives:

$$H_{ij} = - \begin{pmatrix} \frac{\partial^2}{\partial a_1 \partial a_1} & \frac{\partial^2}{\partial a_1 \partial a_2} & \cdots & \frac{\partial^2}{\partial a_1 \partial a_j} \\ \frac{\partial^2}{\partial a_2 \partial a_1} & \frac{\partial^2}{\partial a_2 \partial a_2} & \cdots & \frac{\partial^2}{\partial a_2 \partial a_j} \\ \vdots & \vdots & \ddots & \vdots \\ \frac{\partial^2}{\partial a_i \partial a_1} & \frac{\partial^2}{\partial a_i \partial a_2} & \cdots & \frac{\partial^2}{\partial a_i \partial a_j} \end{pmatrix} * \mathcal{L}(\mathbf{a}) \quad (5.28)$$

Since one usually does not know the analytical form of $\mathcal{L}(\mathbf{a})$, numerical approaches to find the max. Likelihood and the Hesse matrix have to be used [Jam94].

For cross-section measurement analyses, one commonly uses a binned maximum Likelihood method to fit one parameter from a distribution with n bins. Here each bin content of the analysis output distribution is treated as independent measurement. The probability density function is assumed to be Poisson distributed for each bin and the parameter a is defined as deviation factor to the standard model cross-section. This leads to the following definition for the pdf of each bin:

$$f(r, \mu) = \frac{\mu^r}{r!} e^{-\mu}; \quad r \in \mathbb{N}_\mu^+ \quad (5.29)$$

$$f(a, d, s, b) = \frac{\overbrace{(a * s + b)}^M{}^d}{d!} e^{-\overbrace{(a * s + b)}^M} \quad (5.30)$$

Equation 5.29 shows the definition of a Poisson distribution depending on its mean μ and a positive integer value r . Each bin of the analysis output consists of a certain amount of observed data events d and simulated Monte Carlo events M . Data d is assumed to be Poisson distributed with the simulated mean M . The full set of simulated events M consists of two classes: signal s and background b . In both cases standard model cross-sections are used to generate these simulation samples. Since one is interested in the signal cross-section, the total amount of simulation events is defined as $M = a * s + b$, with a being the fitted parameter. A result of $a = 1$ consequently has the meaning of an observed cross-section identical to the expected one (in this case the standard model expectation).

The logarithmic Likelihood \mathcal{L} defined in equation 5.26 is then constructed using the pdf 5.30, which leads to the following expression assuming a distribution with n bins:

$$\mathcal{L}(a) = \sum_{i=1}^n d_i \ln(a * s_i + b_i) - (a * s_i + b_i) - \ln(d_i!) \quad (5.31)$$

The last logarithmic term in equation 5.31 can be neglected for the maximisation, since it does not depend on parameter a .

If only one parameter has to be determined, one can deduce the statistical parameter error directly from the Likelihood shape without knowing the second derivatives. The *central limit theorem* states, that summing over n randomly distributed and independent variables x with mean μ and variance σ^2 will result

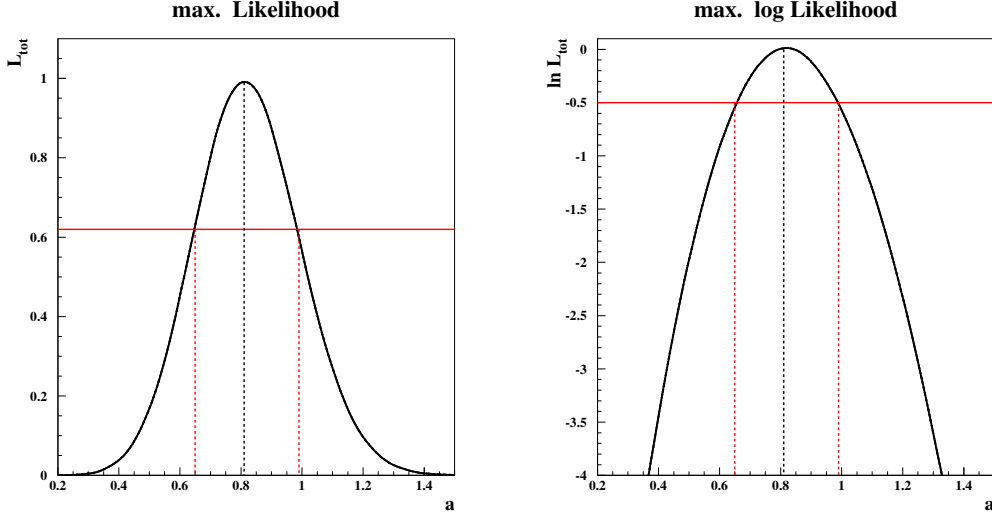


Figure 5.4: The left hand side shows a sample Likelihood distribution. One clearly sees the Gaussian shape with the black dashed line indicating its mean and the grey dashed lines pointing at the standard deviation boundaries. On the right hand side the corresponding logarithmic distribution is shown. The statistical uncertainty is derived from $\mathcal{L}_{max} - \frac{1}{2}$ indicated by the solid grey line, with the dashed grey lines pointing to the resulting 1σ boundaries.

in a Gaussian shaped variable with mean M and variance Σ^2 :

$$M = \sum_{i=1}^n \mu_i \quad (5.32)$$

$$\Sigma^2 = \sum_{i=1}^n \sigma_i^2 \quad (5.33)$$

This theorem requires n to be large, but already 10 distributions can be considered large enough to treat the resulting distribution as a Gaussian. Hence, in many cases the Likelihood L will have a Gaussian shape and variance. For the logarithmic Likelihood \mathcal{L} such an assumption results in a parabolic distribution:

$$\mathcal{L}(X) = \ln L(X) = -\frac{(X - M)^2}{2\Sigma^2} + \text{const.} \quad (5.34)$$

This distribution has its maximum at $X = M$ resulting in

$$\mathcal{L}(X = M) = \text{const.} \quad (5.35)$$

The corresponding value for \mathcal{L} in a distance of one standard deviation to the

maximum ($X = M \pm \Sigma$) yields

$$\mathcal{L}(X = M \pm \Sigma) = \text{const.} - \frac{1}{2} \quad (5.36)$$

By comparing expression 5.35 to expression 5.36 one finds, that one standard deviation Σ corresponds to a change in parameter X such, that the maximum logarithmic Likelihood gets reduced by $\frac{1}{2}$. This result can be exploited to get an estimate for the statistical uncertainty of a Likelihood fit as shown on Fig. 5.4.

The fact that logarithmic Likelihoods of independent measurements can be added up comes very handy when fit results from different analyses have to be combined in order to increase the statistical significance of the final results. Each analysis can be treated as independent measurement and the corresponding logarithmic Likelihoods can be added up to form a combined Likelihood. In the case of cross-section determinations, results derived at different centre-of-mass energies can also be combined to check global compatibility with the Standard Model expectation.

5.5 Kinematic fits with constraints

Kinematic fits have turned out to be very useful in constructing variables for background suppression for both Higgs analyses studied in this thesis. In addition, it is necessary in order to calculate the invariant mass of a hypothetical Higgs boson from the event kinematics observed.

Technically a constraint fit is very much related to the well known least squares fit of an analytic function to observed data. In the case of a kinematic fit in high energy physics, one is more interested in fitting four-vectors of the outcome of an interaction rather than an analytic function. For this thesis the four-momentum vectors of n jets (\mathbf{p}_{fit}) were fitted to the particle tracks observed (\mathbf{p}_{obs}) for each event (see equation 5.37). Additionally, k kinematical constraints like energy and momentum conservation were imposed (see equation 5.38).

$$S = \sum_{tracks} \sum_{jets} (\mathbf{p}_{obs} - \mathbf{p}_{fit})^T \mathbf{V}^{-1} (\mathbf{p}_{obs} - \mathbf{p}_{fit}) \quad (5.37)$$

$$\mathbf{C} = \sum_{jets} \mathbf{p}_{fit} - \begin{pmatrix} \sqrt{s} \\ \mathbf{0} \end{pmatrix} = \begin{pmatrix} 0 \\ \mathbf{0} \end{pmatrix} \quad (5.38)$$

The fitted four-vectors \mathbf{p}_{fit} in equation 5.37 have to be determined such, that S gets minimal by summing over all observed tracks and the corresponding covariance matrix \mathbf{V} . In addition, the constraints \mathbf{C} (see equation 5.38) have to be fulfilled. Both objectives can be achieved by using the method of Lagrange

multipliers, which leads to a new function \mathcal{L} :

$$\mathcal{L} = S(\mathbf{p}_{jet1}; \dots; \mathbf{p}_{jetn}) + \begin{pmatrix} \lambda_1 \\ \lambda_2 \\ \lambda_3 \\ \vdots \\ \lambda_k \end{pmatrix} * \mathbf{C}(\mathbf{p}_{jet1}; \dots; \mathbf{p}_{jetn}) \quad (5.39)$$

The minimising of function 5.39 is performed by setting the first derivative of \mathcal{L} with respect to all \mathbf{p}_{fit} parameters equal to zero.

$$\begin{pmatrix} \frac{\partial}{\partial \mathbf{p}_{jet1}} \\ \frac{\partial}{\partial \mathbf{p}_{jet2}} \\ \frac{\partial}{\partial \mathbf{p}_{jet3}} \\ \vdots \\ \frac{\partial}{\partial \mathbf{p}_{jetn}} \end{pmatrix} * \mathcal{L} = 0 \quad (5.40)$$

Due to the four-vectors involved, this results in $4 * n$ equations (4 equations for each jet). By taking into account k constraints², one ends up with a total of $4 * n + k$ equations in order to determine the same amount of parameters.

In this thesis, all kinematic fits were performed using the PUFITC[KM91] package by *Niels Kjaer*. Typically, three different kinds of kinematic fits were used:

- fits with **4 constraints** using energy and momentum conservation only
- fits with **5 constraints** asking in addition for one invariant jet pair mass to match the signal topology
- fits with **6 constraints** asking for two invariant jet pair masses to match the signal topology

The resulting χ^2 distributions can be easily used as discrimination criterium for a certain kind of background, while the invariant mass, calculated from the fitted four-vectors, can be used to check the compatibility of an eventual excess in data with the expectation from a Higgs boson with a certain mass.

In cases where more than two jets had to be fitted, the definition of the invariant jet pair mass gets ambiguous. In these cases the combinatorical combination resulting in the lowest χ^2 was chosen.

²in case of energy and momentum conservation: $k = 4$

Chapter 6

Systematic errors: the shaking technique

Most physics analyses rely on Monte Carlo (MC) simulations consisting of the physical processes followed by a detector simulation to extract relevant physics from data.

Usually the simulation does not describe the data perfectly, which introduces systematic uncertainties in the physics results. It was found that the most critical parameter affecting the systematic errors of missing energy analyses is the particle multiplicity. If the charged and neutral multiplicities in the MC agree with data in all momentum bins and angular intervals, all other distributions, like visible energy, transverse momentum and thrust turn out to agree better as well. This improvement is also visible in the tails of the distributions and hence has a significant impact on all channels with missing energy, which highly rely on the reconstruction of the energy flow through the detector.

In practice, the multiplicities are simple to measure and easy to correct in the MC by a reweighting technique denoted as “shaking” method. The weight factor is just the ratio of multiplicity in MC and data for a given phase space bin. Since the weight factors are usually quite different for charged and neutral particles, the reweighting is done for each of them separately. In order to check if disagreements between data and MC are due to MC imperfections and do not originate from new physics, one should determine the weight factors from a data sample, for which the physics is known. In this case data from the Z^0 -resonance in e^+e^- -physics was used. Since the multiplicity is only slowly increasing with energy, the weight factors determined at the Z^0 -energy can be used at higher energies as well.

At LEP I, after having performed a loose hadronic preselection, most events originate from non-radiative, multi-hadronic annihilation events at the Z^0 pole. This makes it easy to compare data and MC since only one simulation channel

has to be taken into account. The corrections necessary to bring simulation and data into agreement at LEP I are then propagated to the LEP II high energy MC samples. This is done by adding and removing charged and neutral tracks according to the reweighting determined at Z^0 energy.

The main application considered here is the extraction of a systematic uncertainty in the missing energy channels originating from imperfect description of the detector response. Such errors are commonly evaluated by studying the impact of variations to the most discriminating variables on the final results. The magnitude of these variations is usually deducted from fitting MC to match data in each of the variable distributions taken into account. The advantage of such a method is, that no extrapolations from Z^0 energy to LEP II high energy are necessary. However such a procedure does not take into account correlations between the different variable distributions and it does not distinguish between the contributing event topologies. The shaking however provides a more natural way of estimating these uncertainties, since it propagates them through all variables and analysis steps to the final result without the need to rescale each distribution separately.

It is not recommended to apply the shaking to channels with an isolated particle signature, since adding or removing tracks to leptonic or semi-leptonic events might lead to unphysical changes of the event topologies.

In the following section the technique is described in more detail. Cross-checks are then performed using LEP I data and simulation samples. Finally the method is applied to a LEP II high energy analysis in order to extract its systematic error. In this context two other missing energy analyses were also used to cross-check the impact and the consistency of this technique.

6.1 The reweighting technique

6.1.1 Determination of weight factors

In order to determine the weight factors from data and simulation samples at the Z^0 pole a common particle selection has to be applied first to assure a minimum reconstruction quality. For this task, the Skelana[SS97] based selection was used, which asks for the following particle criteria:

- charged momentum greater than 400 MeV
- charged particles have to originate from within 4 cm in the transverse plane and within $\frac{4 \text{ cm}}{\sin \theta}$ along the beam axis, depending on the polar angle θ

- neutral clusters with more than 300 MeV in the HPC¹ and STIC², or with more than 400 MeV in FEMC³

In addition to this analysis independent selection, it was necessary to remove the Bhabha and two-photon backgrounds due to their high cross-sections, providing a loose hadronic preselection. These cuts were common to all analyses studied in this note and assured an easy comparison. First, there is a requirement of at least two charged particles with transverse momentum greater than 2 GeV, originating from within 1 mm in the transverse plane and 3 mm along the beam axis. After this quality cut a loose hadronic preselection is applied asking for the following event properties:

- at least eight charged particles
- charged energy greater than $0.16\sqrt{s}$
- transverse energy greater than $0.15\sqrt{s}$
- sum of all particle momenta along thrust axis greater than $0.25\sqrt{s}$
- energy of electromagnetic shower below $0.45\sqrt{s}$

This results in a complete suppression of Bhabha events and a 97% reduction of the two-photon background.

As mentioned before, the multiplicity in hadronic events is a function of phase space. Therefore the charged and neutral multiplicities were determined for the following momentum and angular intervals:

- track angle (barrel with $\cos(\theta) < 0.7$ or forward with $\cos(\theta) > 0.7$)
- track momentum ($|p|$ in [0.0, 0.5] [0.5, 1.0] [1.0, 2.0] [2.0, 5.0] [5.0, ∞] GeV)

The averaged multiplicity was determined by fitting a Poisson function to the multiplicity distribution in the considered interval (class).

The discrepancies between data and MC are shown for each class in Fig. 6.1, separately for charged and neutral multiplicities. In each class, a separate correction coefficient P is calculated by determining the mean multiplicities of the corresponding data and MC distributions:

$$P = \frac{\langle N_{data} \rangle - \langle N_{MC} \rangle}{\langle N_{MC} \rangle} \quad (6.1)$$

¹barrel electromagnetic calorimeter

²very forward electromagnetic calorimeter

³forward electromagnetic calorimeter

next to final processing				
	1997 F3	1998 D2	1999 A1	2000 A1
charged multipl.	4.8 %	1.9 %	2.0 %	2.3 %
neutral multipl.	10.1 %	9.1 %	10.4 %	10.3 %
final processing				
	1997 G1	1998 E1	1999 E1	2000 E1
charged multipl.	-. %	3.3 %	2.9 %	2.7 %
neutral multipl.	-. %	10.2 %	11.0 %	9.6 %

Table 6.1: Mean correction coefficients obtained for different years and processings by averaging the ten coefficients within each multiplicity class. Clearly, the charged classes tend to result in a lower correction factor. For 1997, no finally reprocessed Z^0 samples were available.

For $P > 0$ the multiplicity in data is above the one in MC, while for $P < 0$ the opposite is the case. Therefore P can be used as the probability to add or delete tracks in the MC for a given class.

In Tab. 6.1, the mean correction coefficient per year is shown for the two last processings of the DELPHI data (used in a majority of final DELPHI publications), separately for charged and neutral classes.

In general, effects were found to be larger for neutral than for charged particles, and in the forward compared to the barrel part of the detector. On the other hand, effects were similar for both of the last data processings.

6.1.2 Application of the weight factors

In order to apply these coefficients to high energy MC one first needs to perform the same 20 bin classification already used for the 91 GeV samples. Since every coefficient corresponds directly to a probability for adding or removing a track in the corresponding class, all multiplicities in each class are modified accordingly. If a specific track is to be removed, it is locked via LVLOCK in the VECP array (see [SS97]). Hence, it will be ignored by all analysis routines. If a track has to be added, it is important, that the event topology is conserved. One way of doing this is to take an existing track from the same event and just duplicate it. Since two identical tracks would be unphysical, the duplicated track's momentum is smeared by 2.5% in all directions (x, y and z). This corresponds to the assumed track resolution.

In order to add a track in one of the 20 classes, at least one track must exist in each class. If not, no track will be added. In cases where the MC has more events with 0 tracks in a given class than the data, one has to add a track

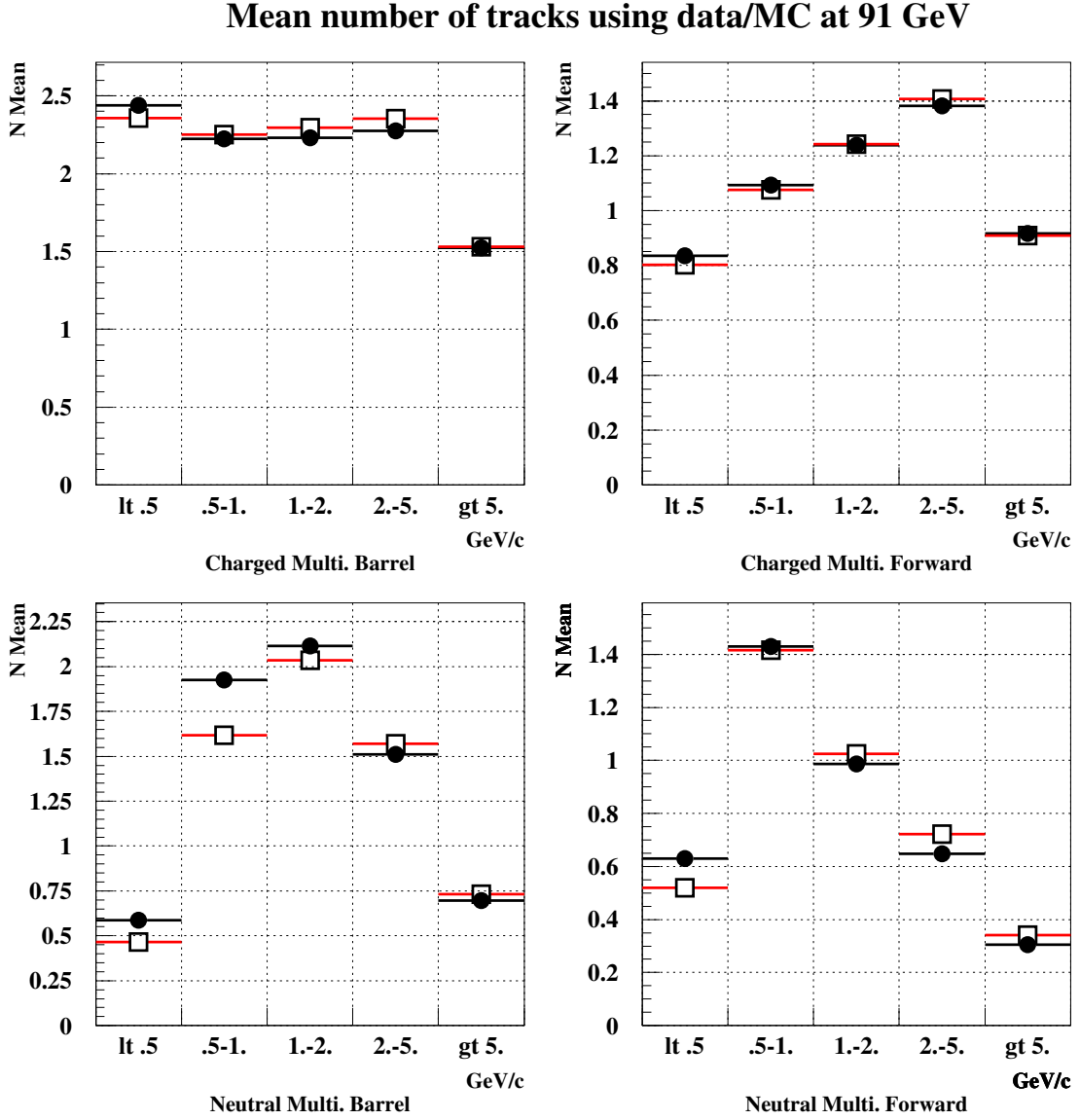


Figure 6.1: Mean multiplicities obtained from 99 Z^0 samples using data (bullets) and MC (squares). Every histogram represents a multiplicity class containing tracks of 5 different momentum regions.

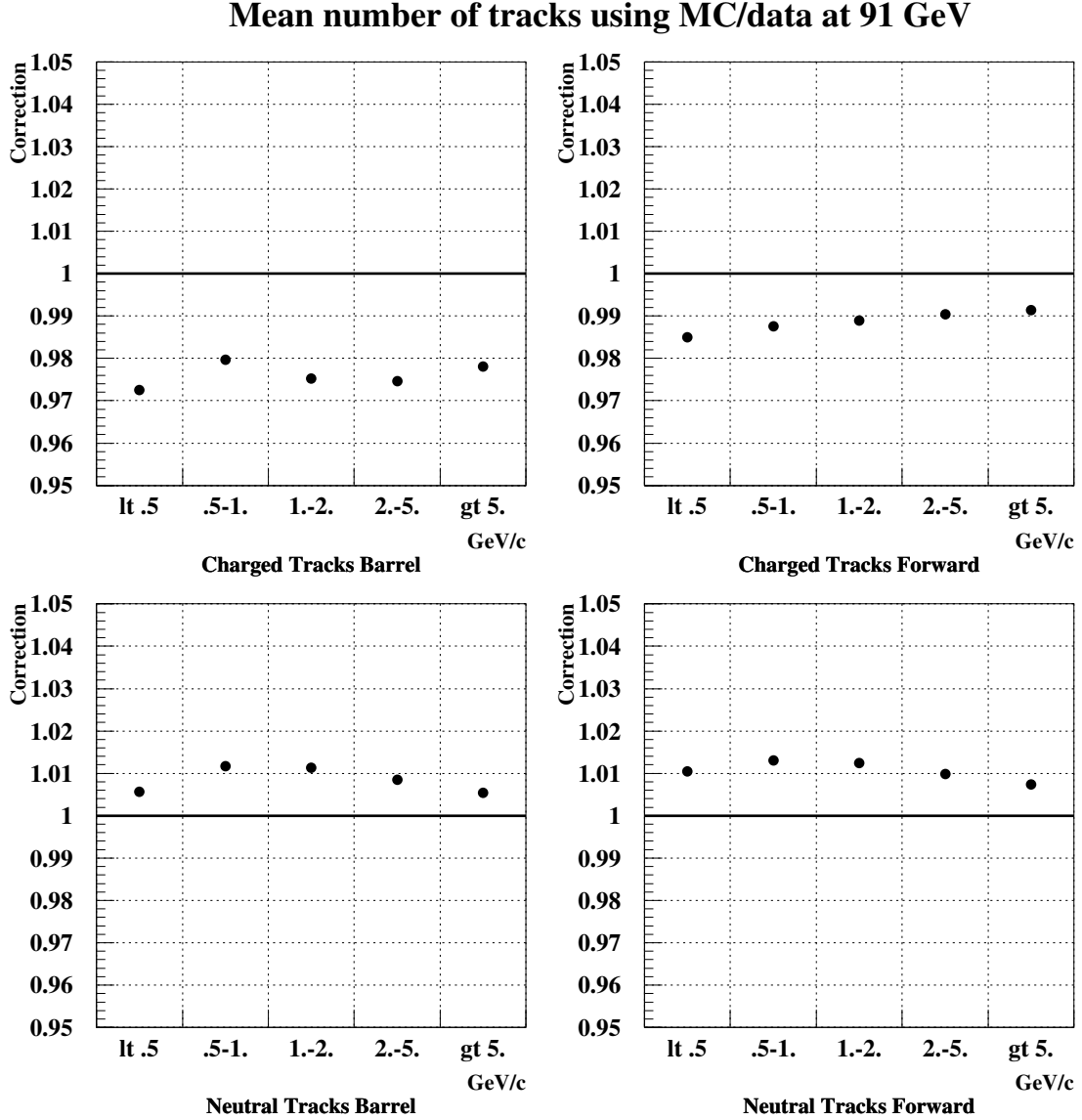


Figure 6.2: Correction coefficients for events with no tracks in the corresponding phase space class. In case of charged tracks, the necessary corrections are negative, hence MC events with one track have to migrate to events with no track in the corresponding phase space bin. This is covered by correcting the mean multiplicities. But in the neutral case, tracks have to be added to events with no tracks. Hence, a migration from events with no tracks to events with one track is necessary using the corrections shown on the lower plots.

in this “0”–multiplicity interval so it will migrate to the “1”–multiplicity bin. The probability for this migration is determined from the first two bins of the multiplicity distribution. If migration is needed, for example a neutral track needs to be added with a certain probability for a certain class, then a charged track in that class is duplicated, smeared and its charge set to zero.

This guarantees a consistent event topology since the track is taken from a class with the same momentum and polar angle range. It may happen that the corresponding charged class also does not have any tracks suitable for this event. In this case, the track is taken from one of the higher momentum classes and scaled down correspondingly to meet the requirements of the target class. It should be noted, that this procedure of copying tracks from other event classes is only necessary in rare cases (roughly 1 % of all events) and mainly neutral tracks are affected (see Fig. 6.2).

6.2 Applications for the shaking method

Since analyses, searching in channels with missing energy signature, tend to be very sensitive to uncertainties in the energy flow, they are predestinated as application for the shaking technique. First, some basic checks at Z^0 energy will be described, then the effect of the shaking on LEP II analyses will be studied.

6.2.1 Cross-checks by shaking 91 GeV MC samples

Several tests have been performed in order to study and check the effects of the shaking method under different conditions. First, some low level comparisons like checks in overall charged and neutral multiplicity mean values have been done (see Fig. 6.3). Both multiplicity shapes can be seen on Fig. 6.3 using the multi-hadronic preselection to remove $\gamma\gamma$ and Bhabha background as stated above. On these plots, the impact of the shaking is best visible in the neutral case (two lower plots on Fig. 6.3) since typically larger corrections have to be applied. One clearly observes a significant improvement in the distribution shape resulting in a better data–MC agreement.

Two further variables with high importance to missing energy analyses due to their discrimination power have been studied: transverse momentum and acoplanarity times inter-jet angle (see Fig. 6.4). In order to emphasize the regions relevant for missing energy analyses, a typical LEP II energy signal ($ZZ \rightarrow qq\nu\nu$) was included in the figure.

In case of the transverse momentum, there is a clear tendency in the simulation to overestimate low momenta and to underestimate the higher momenta region (see upper left of Fig. 6.4). This shift of the distribution is perfectly corrected by

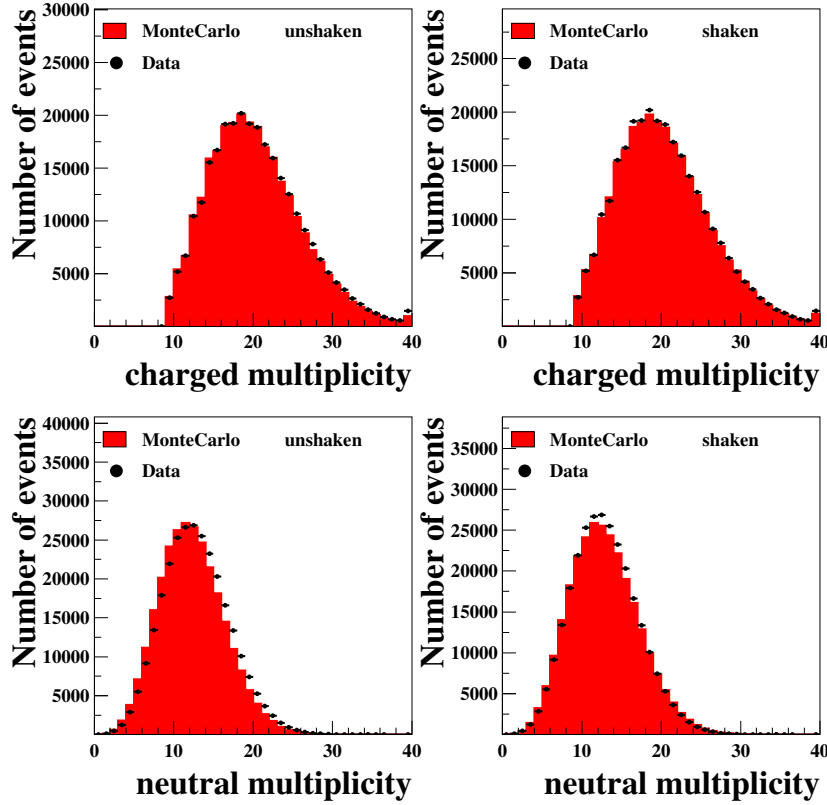


Figure 6.3: Comparison of multiplicity distributions between 91 GeV data and MC before and after shaking using Z^0 calibration samples of 1997 until 2000. The improvement of the shape is clearly visible for the neutral part, while for the charged tracks the corrections are too small to be visible.

the shaking technique as can be seen on the upper right. This also applies to the indicated signal like region (see black arrow), where 40633 events were found in data, with 36024.1 events predicted by the normal MC simulation and 39082.2 events predicted by the shaken simulation samples.

The situation is similar in the case of the acoplanarity times inter-jet angle distribution, although not as severe. Here, an underestimation of data by simulation is visible for events with high acoplanarity, in the region of the typical missing energy signal studied. Again the shaking provides a nice correction and brings the simulation into good agreement with data. For this variable the indicated signal region (see black arrow) contains 40983 events in data, 38267.0 events are predicted by the unmodified simulation, while 40837.8 events are simulated by

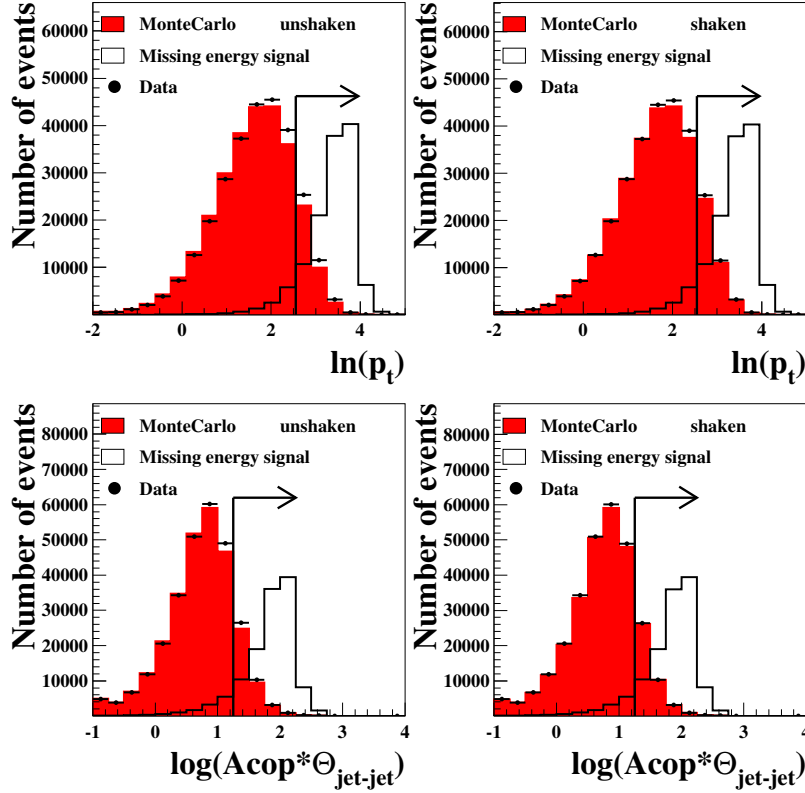


Figure 6.4: The effect of the shaking on simulated events of two variables commonly used for missing energy analyses (transverse momentum and acoplanarity times inter-jet angle) using 91 GeV calibration samples (1997 until 2000). A typical LEP II missing energy signal is included to point out the importance of the tail regions.

the shaken MC.

From these checks, one can conclude, that the method works as expected at 91 GeV centre-of-mass energy and that the main reason for discrepancies in data-simulation agreement is indeed related to particle flow reconstruction deficiencies. These are well simulated by the shaking method and all distributions analysed show a remarkable recovery of their initial deficiencies.

6.2.2 Checks using LEP II samples

Now another set of consistency tests were performed using LEP II high energy data and MC samples. In a first step, the shapes of typical variables at preselection

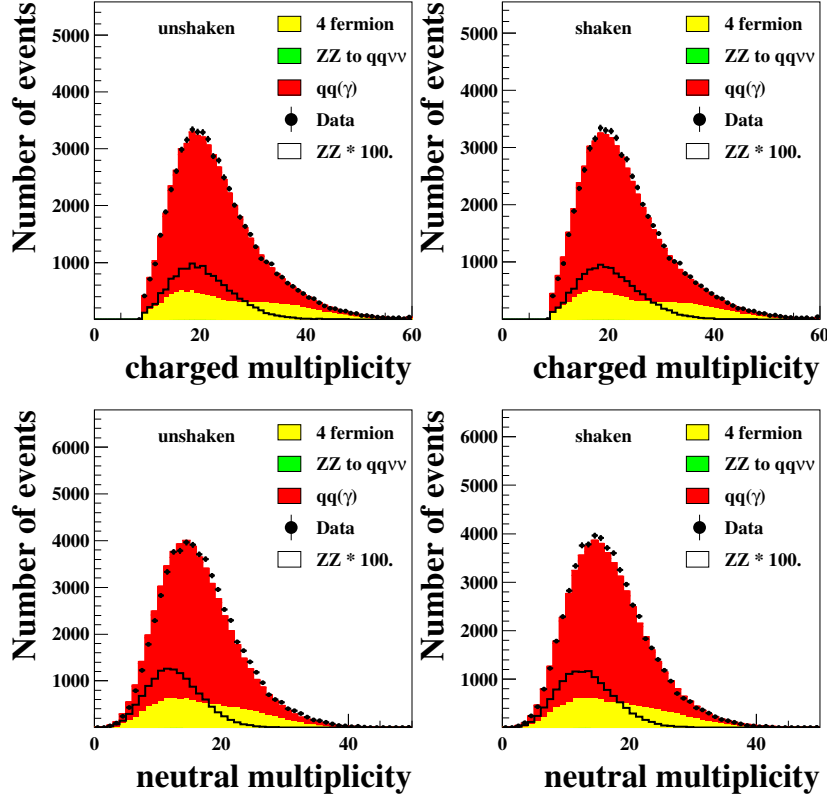


Figure 6.5: Comparison of multiplicity distributions between LEP II data and MC before and after shaking using high energy samples of 1997 until 2000. There is a slight improvement of the shape visible for the neutral part, while for the charged tracks only very small corrections are observed.

tion level were investigated. Then the shapes of the final discriminant variables of three missing energy analyses have been checked in order to study the impact of the shaking on analysis level with typical missing energy signature.

Preselection level studies

Since it is also interesting to study the impact of these shaken MC samples on LEP II analyses, data–MC agreement evolution at different preselection levels common to missing energy channels have been studied. The preselection criteria are characterised by two classes of cuts:

energy	cut	two-photon	Bhabha	two-ferm.	four-ferm.
189 GeV	hadr. presel.	8071.0	8664.7	14374.2	2430.7
	$\gamma\gamma$ cuts	236.3	0.0	12227.5	2339.3
	QCD cuts	16.4	0.0	1016.5	485.9
200 GeV	hadr. presel.	4212.9	31.2	6609.1	1353.8
	$\gamma\gamma$ cuts	107.0	0.0	5537.7	1306.9
	QCD cuts	12.8	0.0	490.8	266.2
207 GeV	hadr. presel.	3788.6	25.7	5943.4	1335.6
	$\gamma\gamma$ cuts	96.2	0.0	4885.6	1288.6
	QCD cuts	10.8	0.0	434.3	256.5

Table 6.2: Number of events in the $e^+e^- \rightarrow ZZ \rightarrow q\bar{q}\nu\bar{\nu}$ analysis between 183 and 207 GeV after various cuts. They show that only a small amount of QCD and four-fermion events successfully pass the selection criteria.

- cuts to remove gamma-gamma and Bhabha background
- cuts to remove two-fermion background (QCD)

Each step is sequentially applied and results in a corresponding background reduction. In particular the $\gamma\gamma$ and Bhabha contributions get nearly completely suppressed. Tab. 6.2 gives an overview on how many events of each background type typically pass such an analysis.

The comparison of shaken and unshaken samples at different preselection levels of a typical missing energy analysis can be seen on Fig. 6.5. Here charged and neutral multiplicities combining centre-of-mass energies from 183 to 207 GeV are shown after having removed Bhabha and di-photon background events. A very good agreement between data and simulation is visible for the charged multiplicities and the shaking has only a negligible effect there. For the neutral multiplicity there is some improvement visible in the low multiplicity region, which corresponds to the signal region.

On the next set of plots (see Fig. 6.6) the variables transverse momentum and acoplanarity times inter-jet angle are analysed at preselection level, using LEP II high energy data and simulation samples. The transverse momentum distribution shows a slight underestimation of signal like events in the case of regular MC samples, which is confirmed by counting data and simulation events as indicated, resulting in 3061 data events and 2929.5 events expected from simulation. The shaking seems to improve the situation slightly by shifting the whole distribution towards higher transverse momentum, leading to more signal like events. However, repeating the event counting in the signal region yields 3172.1 events, which overestimates the 3061 events observed.

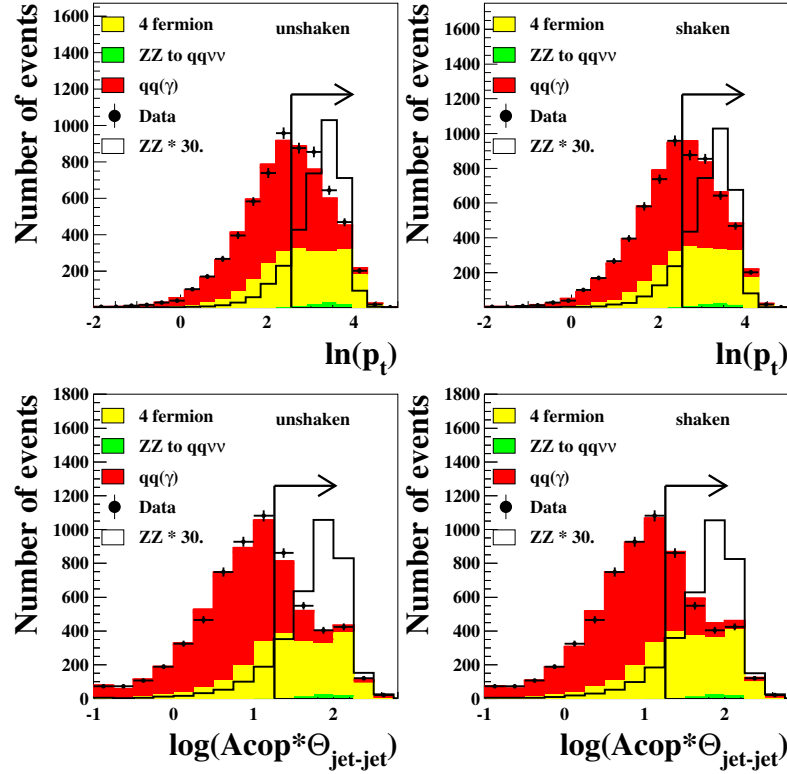


Figure 6.6: The effect of the shaking at preselection level on the simulation prescription of two variables commonly used for missing energy analyses (transverse momentum and acoplanarity times inter-jet angle) using LEP II high energy samples (1997 until 2000). A typical LEP II missing energy signal is included to point out the importance of the tail regions.

The situation is quite similar for the second variable analysed: acoplanarity times inter-jet angle. Again data is slightly underestimated by MC in the signal region, while the shaking leads to a slight overestimation. Counting the amount of signal like events in data and simulation leads to 2379 data events, 2263.0 expected events from regular MC and 2479.9 events from using shaken simulation samples.

Analysis level studies

Here, the influence of shaken MC samples on the overall shape of final discriminant variables for three typical missing energy analyses have been studied (see

Fig. 6.7). For the missing energy analysis $ZZ \rightarrow q\bar{q}\nu\bar{\nu}$ the full statistics available, ranging from 183 GeV taken during 1997 up to 208 GeV taken during 2000, was used. The two other analyses provided cross-checks and only one energy was used in each case to study the final discriminant variables.

- $ZZ \rightarrow q\bar{q}\nu\bar{\nu}$ (described in detail in the next chapter)
- hZ with $Z \rightarrow q\bar{q}$ and h decaying invisibly[Sta03]
- hZ with $h \rightarrow b\bar{b}$ and Z decaying invisibly[DHJ⁺03]

In case of the $ZZ \rightarrow q\bar{q}\nu\bar{\nu}$ analysis, there is a clear underestimation of data in the tail for low values of the discriminant variable, which gets perfectly corrected by the shaking. However, especially around the distribution peak, the shaking predicts too many events. This is confirmed by counting the amount of data and simulated events for the full distribution, resulting in: 834 data events, 783.8 simulated unshaken events and 895.8 simulated shaken events. By focusing on the signal region of this distribution at an efficiency of approximately 40 %, data (112 events) is better described by the unshaken simulation (123.7 events), while the shaking is predicting 127.9 events. In this high purity region the effect from the shaking is very small and dominated by the statistical uncertainties.

A similar behaviour can be observed for the analysis searching for invisibly decaying Higgs bosons. Here 46 events were counted in data, while unshaken simulations predicted 43.4 events for the final discriminant distribution. By using shaken MC samples the amount of expected events increased to 52.9, which leads to an overestimation. Concerning the general shape of the final discriminant variable, both simulations (unshaken and shaken) provide a reasonable description for the data observed.

In case of the third analysis, Fig. 6.7 shows a clear improvement in shape by using shaken simulation samples to describe data. This observation is confirmed by counting the total amount of events for both simulations. Here 28 events were observed in data, while only 21.4 were predicted by unshaken simulations. The amount of predicted MC events increases to 25.4 by applying the shaking technique, which leads to an improvement in data description.

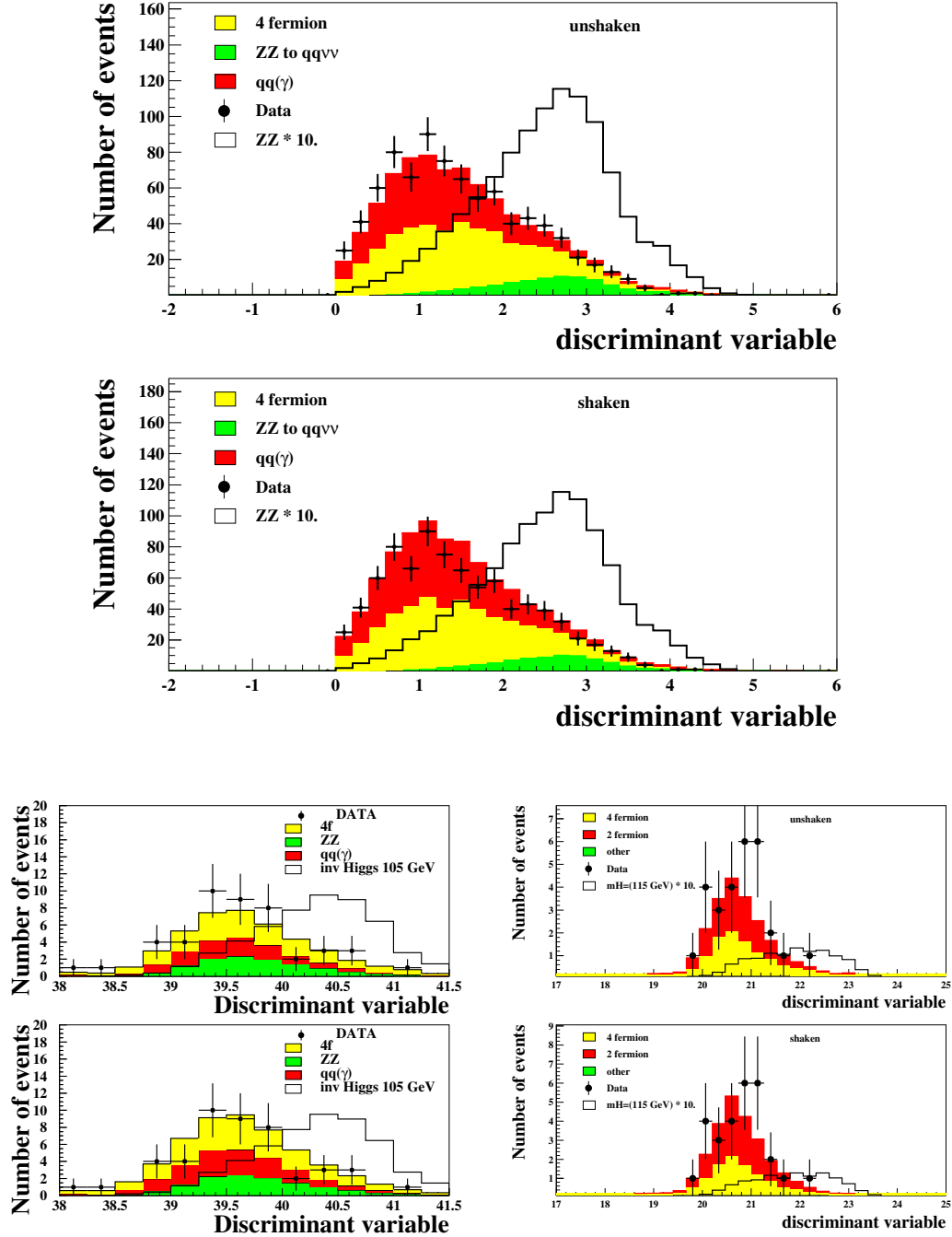


Figure 6.7: The effect of the shaking on final discriminant variables using three missing energy analyses: $ZZ \rightarrow qq\nu\bar{\nu}$ (upper), hZ with $Z \rightarrow q\bar{q}$ and h decaying invisibly (lower left) and hZ with $h \rightarrow b\bar{b}$ and Z decaying invisibly (lower right).

6.2.3 Conclusions

The checks performed using 91 GeV samples provide a proof of principle, that the correction coefficients derived from the same samples indeed lead to a strong improvement of variable shapes and mean values concerning the agreement between data and simulation. Applying the same method to LEP II high energy samples resulted in the same tendency, but especially in the signal region the shaken MC samples generally led to an overestimation of data where the unshaken simulation underestimated the measurement.

Consequently, the shaking technique should not be used as a correction for the MC simulation, but still it allows to estimate the uncertainty coming from the imperfect description of the detector response and its manifestation in an incorrect prediction of event multiplicities. This can be done, by conservatively interpreting the full effect of the shaking on the final result as systematic uncertainty.

6.3 Scaling and boosting technique

The statistics in data at LEP II energies is too limited to study precisely the effects of the shaking at high signal purity. Hence a special technique was introduced which allowed to check, that data indeed lies within the uncertainty band defined by unshaken and shaken MCs using data and simulation samples of the calibration runs at Z^0 energy. In addition, it allows to verify, whether the interpretation of the differences between shaken and unshaken results as systematic error band is justified.

From the studies performed in the previous sections, it was found, that the MCs affected most by the shaking, and therefore also contributing most to the total systematic error, are the two-fermion final state samples. Therefore data and MC samples at the Z peak have been used to mimic this process at LEP II

topology	$\sqrt{s} = 189\text{GeV}$	$\sqrt{s} = 207\text{GeV}$
non-radiative	22.8 %	22.7 %
single-radiative	69.6 %	68.1 %
double-radiative	7.6 %	9.2 %

Table 6.3: Contribution of non-radiative, single-radiative and double-radiative return events to the total two-fermion final state background as estimated from MC. Both columns show results after having performed a loose hadronic preselection. A threshold of 10 GeV was imposed to accept photons using generator information.

energies as well as possible in order to cross-check the reliability of the shaking in high purity signal regions with the full statistics provided by the Z^0 runs from 1997 to 2000.

The two-fermion final state processes can be divided up in 3 categories: non-radiative, single-radiative and double-radiative events, with photons being emitted via initial state radiation. Each of these event topologies contribute to the total two-fermion QCD background in the ZZ analysis as shown in table 6.3. One clearly sees that mainly single-radiative events plus some non-radiatives contribute significantly. Hence, these two topologies were simulated using two-fermion MC at the Z^0 peak by applying a so-called “scaling and boosting” technique.

In order to simulate $Z \rightarrow q\bar{q}$ non-radiative and $Z \rightarrow q\bar{q}\gamma$ single radiative two-fermion final state events, the energy distribution of the most energetic photon $E_{1\gamma}$ was extracted from two-fermion samples at LEP II centre-of-mass energies using generator information. Using this distribution, an event was classified as non-radiative or single-radiative according to the following criteria:

- events with $E_{1\gamma} < 10 \text{ GeV}$ were considered non-radiative
- events with $E_{1\gamma} > 10 \text{ GeV}$ were considered single-radiative

For the non-radiative case, all events were accepted as relevant for missing energy analyses. However a typical missing energy analysis would efficiently reject $Z \rightarrow q\bar{q}\gamma$ events with an identified isolated photon. Hence, only events with the photon lost in insensitive regions of the detector at LEP II energies were taken into account due to their much higher signal affinity. The resulting photon energy distribution E_γ was then used as probability distribution to calculate the energy of the two-fermion system E_{2f} for each event:

$$E_{2f} = \sqrt{m_{Z^0}^2 + E_\gamma^2} \quad (6.2)$$

Knowing E_{2f} , one can now use the 91 GeV two-fermion sample to simulate the LEP II 2 fermion part by scaling up the track energy of each event in the following way:

$$f_{scale} = \frac{E_{2f}}{91 \text{ GeV}} \quad (6.3)$$

The mass of each particle must not change during this transformation. Hence energy and momentum of each track were scaled by applying f_{scale} such that the invariant mass of each track was conserved:

$$E_{2f}^{track} = f_{scale} * E_Z^{track} \quad (6.4)$$

$$p_{2f}^{track} = \sqrt{(E_{2f}^{track})^2 - ((E_Z^{track})^2 - (p_Z^{track})^2)} \quad (6.5)$$

Finally the resulting two-fermion system had to be boosted in order to take the photon into account, which is assumed to be lost in the insensitive parts of the detector. This was done by performing a Lorentz transformation resulting in the following four-vector for the simulated LEP II two-fermion system:

$$E_{2f}^* = \frac{E_{cm}^2 + E_{2f}^2}{2 E_{cm}} \quad (6.6)$$

$$p_{2f}^* = \sqrt{(E_{2f}^*)^2 - m_Z^2} \quad (6.7)$$

The direction of the boost vector was chosen to be within few degrees in θ to the beam pipe, since most of the photons get lost in this region.

In order to cover a wide range of missing energy topologies, the scaled and boosted simulations have been applied to the three typical missing energy analyses already introduced earlier with four different phase space optimisations depending on their signal topologies:

- hZ with $Z \rightarrow q\bar{q}$ and h decaying invisibly at 207 GeV[Sta03]
- hZ with $Z \rightarrow \nu\bar{\nu}$ and $h \rightarrow b\bar{b}$ at 207 GeV[DHJ+03]
- $ZZ \rightarrow q\bar{q}\nu\bar{\nu}$ at 183 GeV centre-of-mass energy
- $ZZ \rightarrow q\bar{q}\nu\bar{\nu}$ at 207 GeV centre-of-mass energy

For an easy comparison of shaken and unshaken MC with data, a performance curve was plotted showing the integrated amount of events at different levels of the corresponding signal efficiencies. This exercise was performed for each of the three analyses, leading to the following results and conclusions.

6.3.1 Analysis with invisible Higgs decays at 207 GeV

This analysis is optimised to search for an invisibly decaying object close to the kinematic limit, leaving the visibly decaying Z^0 basically at rest. From the performance plot in Fig. 6.8, one sees nicely, that data falls well in between the uncertainty band limited by shaken and unshaken simulation.

6.3.2 Analysis with $Z \rightarrow \nu\bar{\nu}$ and $h \rightarrow b\bar{b}$ at 207 GeV

Here, the analysis was optimised to detect a Higgs boson decaying visibly to a pair of b-quarks with a mass close to the kinematic limit, while the Z^0 Boson decays invisibly to a pair of neutrinos. Again the corresponding performance plot in Fig. 6.9 is in reasonable agreement with an error band interpretation.

6.3.3 $ZZ \rightarrow q\bar{q}\nu\bar{\nu}$ at 183 GeV

The event topology selected by this analysis is characterised by an invisibly decaying Z^0 and a second Z almost at rest, which decays visibly. Here the corresponding performance plot (Fig. 6.10) shows a clear underestimation of data by unshaken MC, although data does not contradict with the uncertainty band.

6.3.4 $ZZ \rightarrow q\bar{q}\nu\bar{\nu}$ at 207 GeV

The same ZZ analysis was repeated using data and MC samples scaled/boosted up to 207 GeV resulting in a boosted visible system. Again, one can conclude from Fig. 6.11, that data is well situated within the uncertainty band, although this time much more compatible with the unshaken MC samples.

6.3.5 Conclusion

For three out of four analyses studied, the data were fairly well described by unshaken MC samples at relatively high signal purities (corresponding to about 40 % efficiency), while the description by shaken samples tended to exceed the data in these cases. In general, for all of the four analyses, the performance plots were however nonetheless still compatible with an error band limited by shaken and unshaken simulations, as described in section 6.2.3. This confirms that the correction coefficients determined using Z^0 energy runs can be used to extrapolate to high energy. It also indicates that the interpretation of the full width as $\pm 1\sigma$ error around a central value in the middle of this band is reasonable.

6.4 Interpretation and outlook

In the context of reconstructing the energy flow of events, it was shown that charged particle multiplicities are relatively well described by present MC simulations. However, neutral particle multiplicities require corrections up to 10 % in the various phase-space classes defined.

The shaking method provides a useful tool to study the impact of such discrepancies on global energy flow variables as well as the propagation of the effects onto the results of analyses involving purely hadronic systems or hadronic systems with missing energy. It can however not be considered reliably as a correction scheme for the simulation.

A reasonable way to estimate the corresponding systematic errors consists in comparing the final results of the studied analysis using regular and shaken LEP II

MC. The difference between the two can be interpreted as ± 1 sigma of the error arising from the imperfect MC modelling, around a central value in the middle of the resulting uncertainty band.

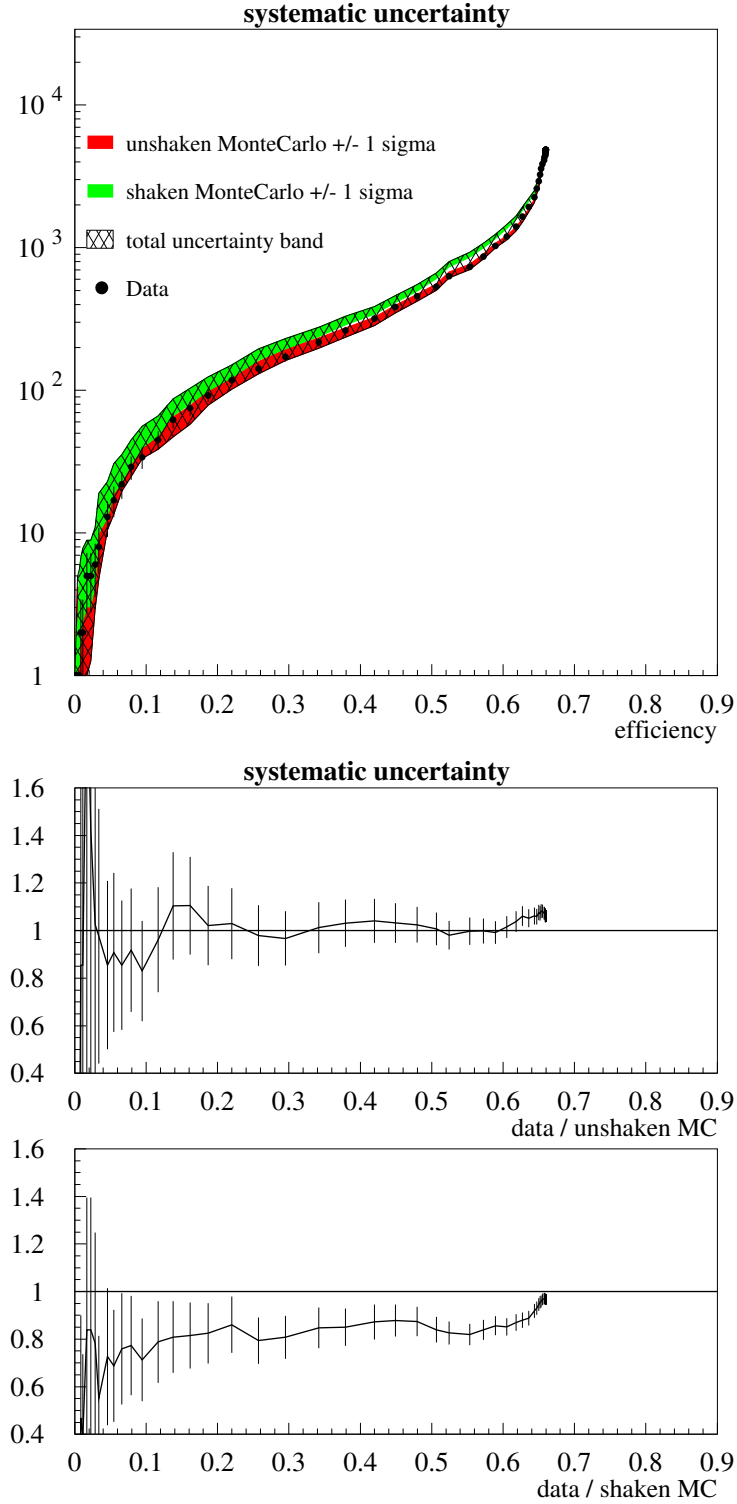


Figure 6.8: Performance plot showing data/MC agreement over signal efficiency by using scaled and boosted MC samples. The coloured area is representing the $\pm 1\sigma$ -band for each sample while the dashed part marks the full uncertainty. The analysis was optimised to search for an invisibly decaying Higgs boson with a mass close to the kinematic limit at a centre-of-mass energy of 207 GeV.

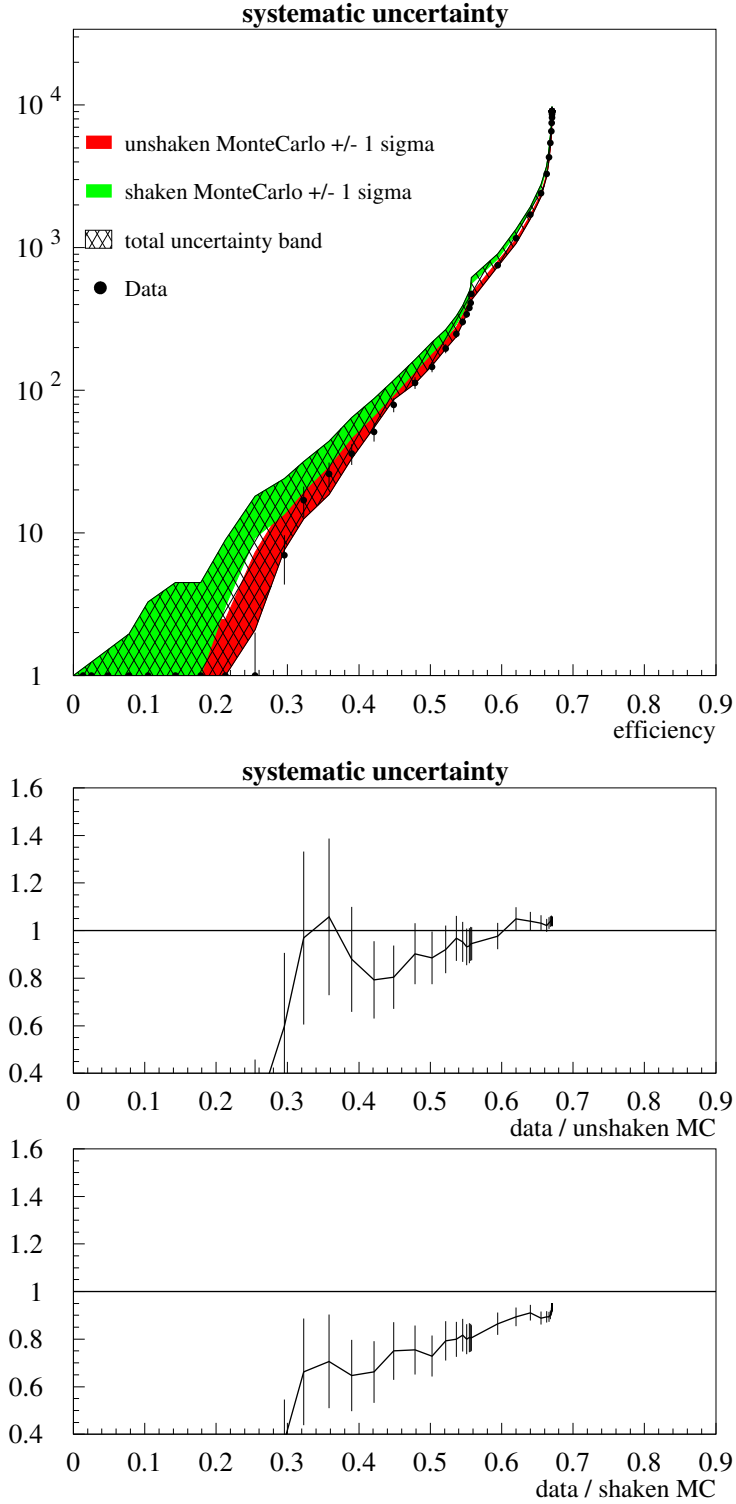


Figure 6.9: Performance plot showing data/MC agreement over signal efficiency by using scaled and boosted MC samples. The coloured area is representing the $\pm 1\sigma$ -band for each sample while the dashed part marks the full uncertainty. The analysis was optimised to search for a hZ production with the Z^0 decaying invisibly and a Higgs (mass close to kinematic limit) decaying to a $b\bar{b}$ pair at a centre-of-mass energy of 207 GeV.

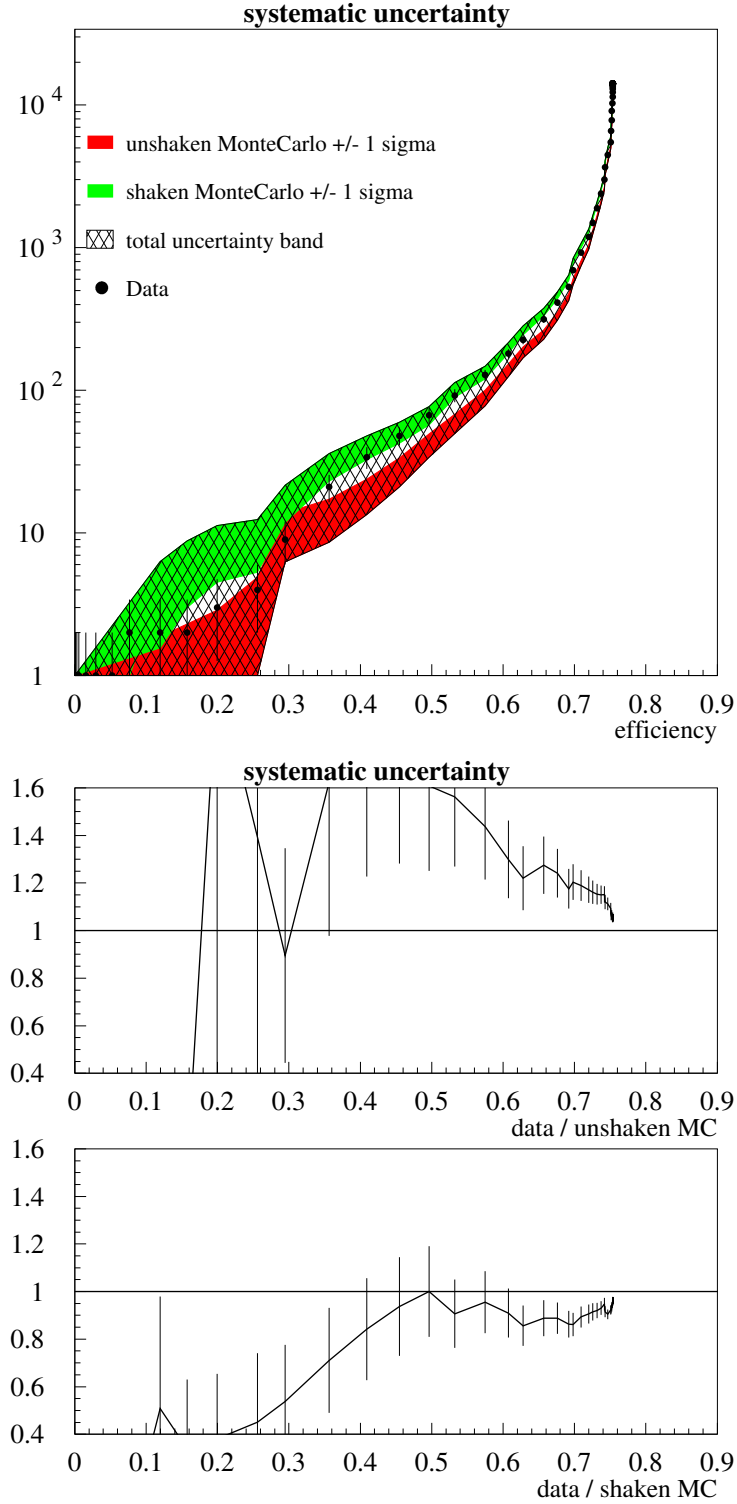


Figure 6.10: Performance plot showing data/MC agreement over signal efficiency by using scaled and boosted MC samples. The coloured area is representing the $\pm 1\sigma$ -band for each sample while the dashed part marks the full uncertainty. The analysis was optimised to search for doubly resonant Z^0 pair production at a centre-of-mass energy of 183 GeV.

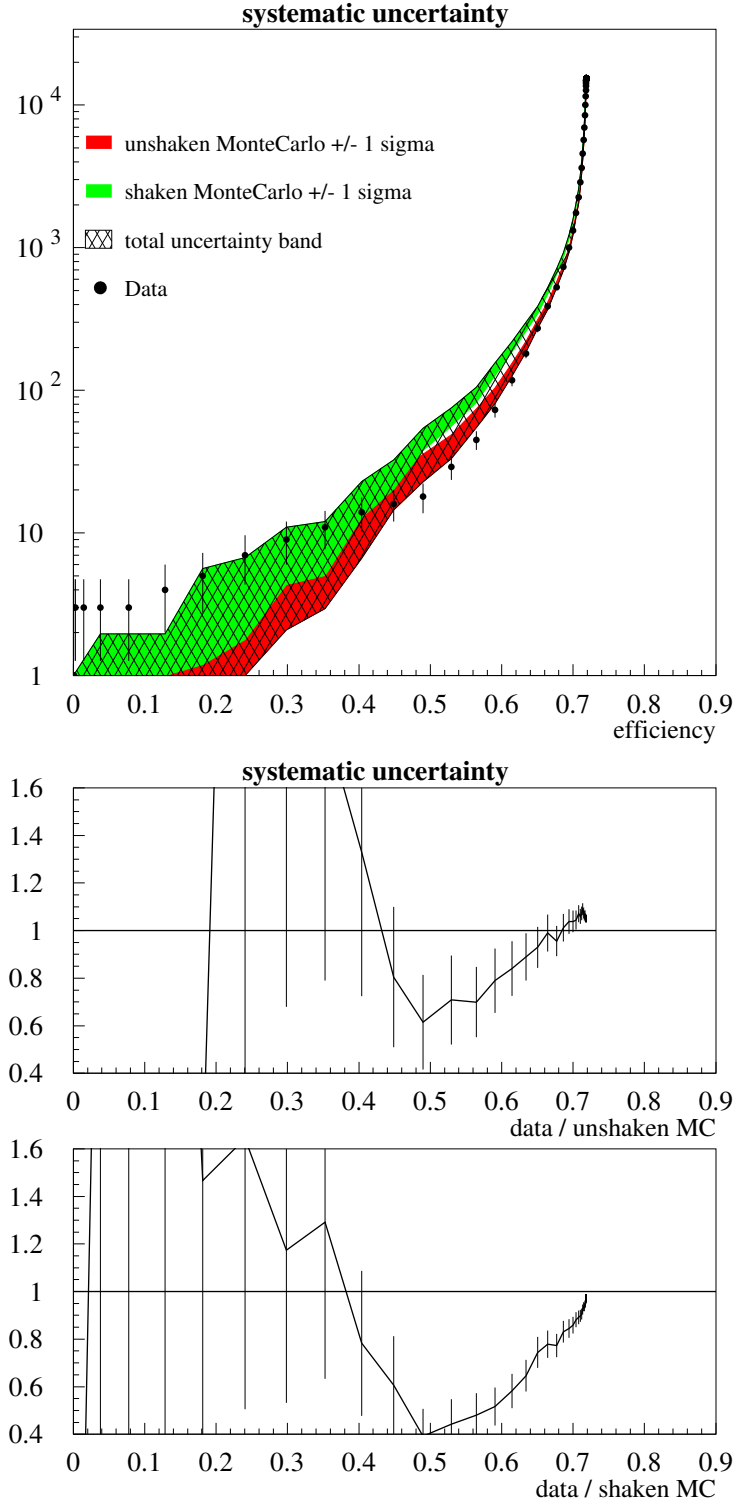


Figure 6.11: Performance plot showing data/MC agreement over signal efficiency by using scaled and boosted MC samples. The coloured area is representing the $\pm 1\sigma$ -band for each sample while the dashed part marks the full uncertainty. The analysis was optimised to search for doubly resonant Z^0 pair production at a centre-of-mass energy of 207 GeV.

Chapter 7

Cross-section measurement of doubly resonant Z^0 pairs

Measuring the doubly resonant Z^0 pair production cross-section became firstly possible in 1987, when LEP reached the threshold centre-of-mass energy of 183 GeV. Main backgrounds arise from two-fermion, W^+W^- and $W e \nu$ processes. Since the signatures of W^+W^- and $W e \nu$ decay products are very similar to those coming from ZZ , it is a challenging task to isolate these background sources. In addition, the cross-sections for W^+W^- and two-fermion processes are roughly 25 and 215 times larger respectively.

The ZZ production channel enabled us to perform additional cross-checks on the Standard Model by comparing the observed production rate with the expectation. Since LEP has increased its operating energy during the runs in 1999 and 2000, the cross-section evolution at different centre-of-mass energies can also be compared with the corresponding Standard Model predictions. Another motivation to study this channel is its great importance for the Higgs searches. ZZ

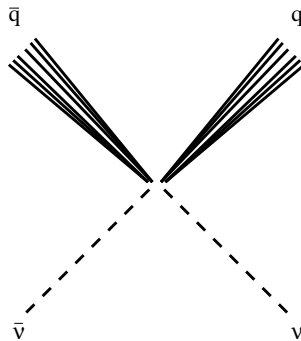


Figure 7.1: Schematic presentation of the process $ZZ \rightarrow q\bar{q}\nu\bar{\nu}$ resulting in two quark jets and missing energy.

class	channel	Br ratio
vis. fermions	qqqq	48.8 %
	qqll	9.4 %
	llll	0.5 %
miss. energy	qq $\nu\nu$	28.0 %
	$\nu\nu\nu\nu$	4.0 %
	ll $\nu\nu$	2.7 %
$\tau\tau$	$\tau\tau$ qq	4.7 %
	$\tau\tau\nu\nu$	1.3 %
	$\tau\tau$ ll	0.5 %
	$\tau\tau\tau\tau$	0.1 %

Table 7.1: Overview of the possible ZZ decay channels and their corresponding branching ratios. Here ll denotes electrons and muons only.

forms an irreducible background for the Higgsstrahlungs process HZ, especially if the Higgs boson mass is close to that of the Z^0 boson. Hence powerful selection and discrimination techniques are required in order to clearly identify doubly resonant Z^0 pair processes. Measuring the ZZ cross-sections also contributes to the searches for new physics beyond the Standard Model, such as anomalous neutral current triple gauge couplings (TGC). Here a Z^0 pair couples directly to another Z^0 or photon and hence forms a TGC, which is forbidden in the Standard Model. The existence of such a process would also lead to a deviation from the Standard Model cross-section and from the expected angular distributions of the initial di-bosons.

A doubly resonant pair of Z^0 bosons can decay in several channels with typical signatures and branching fractions. The analysis studied in this thesis focuses on the channel providing the second highest branching ratio of 28 % (see table 7.1): $ZZ \rightarrow q\bar{q}\nu\bar{\nu}$. Here, one boson decays hadronically, resulting in two jets of particles, while the other Z^0 leads to a pair of neutrinos. Since neutrinos escape undetected, such events are characterised by missing energy and momentum, carried away by the two neutrinos (see Fig. 7.1). The resulting event topology typically leads to a pair of rather acoplanar jets (centre-of-mass energy dependent) and both reconstructed masses (visible and recoil) compatible with the Z^0 mass.

7.1 Data and simulation samples

In the years from 1997 until the end of 2000, DELPHI accumulated a total integrated luminosity of $665.3pb^{-1}$ above the production threshold for Z^0 pair produc-

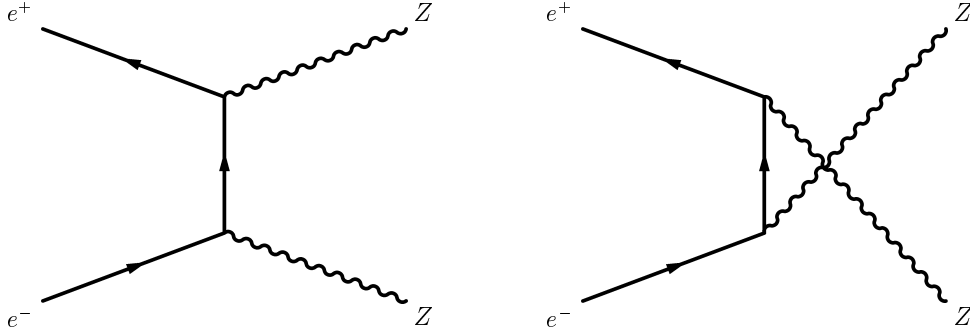


Figure 7.2: Feynman graphs contributing to the NC02 doubly resonant Z^0 pair production.

tion. The full data set was analysed, including centre-of-mass energies ranging from 183 GeV up to 209 GeV. During the run in 2000, one sector (corresponding to $\frac{1}{12}$) of DELPHI's main tracking chamber had a major malfunction and was deactivated for the last quarter of data taking in 2000. All analyses treated this period separately and special simulation samples had been produced to take into account the missing information.

In order to compare the measured data with the Standard Model expectation, all relevant processes have been simulated using appropriate Monte Carlo simulation programs. In the following, the simulation packages used for this analysis will be summarized:

- EXCALIBUR[BPK95] was used to simulate four-fermion final state processes
- GRC4F[F⁺97] focused on a subset of four-fermion final state events coming from $W e \nu_e$ and $(Z/\gamma^*)e^+e^-$ processes, with the charged leptons close to beam pipe direction
- PYTHIA[Sjö93] generated the hadronic two-fermion final state processes including initial state radiation: $e^+e^- \rightarrow q\bar{q}(\gamma)$
- the corresponding leptonic two-fermion final state interactions were simulated by BHWIDE[JPW97] for electrons and by KORALZ[JWW93] for muons and taus
- TWOGAM[NOT90] and BDK[BDK86] were used to describe two-photon interactions, covering all three models necessary for a complete description (see chapter 4.3)

The simulation size should be high enough in order to cause negligible statistical

errors compared with data. Hence, all event topologies have been simulated with at least 100 times the statistics expected from data.

The aim of this analysis was the measurement of the NC02 doubly resonant Z^0 pair production (see Fig. 7.2). Since it was not possible to produce pure simulation samples containing only NC02 processes, the contribution from other four-fermion processes mimicing the NC02 final states (mainly $Z\gamma^*$) had to be isolated and removed. This was done by calculating the matrix elements from the four-momenta of the final state fermions for NC02 only (M_{NC02}) and for all graphs contributing (M_{all})[Cos00]. Each event then had to pass the following criterium:

$$\frac{|\mathcal{M}_{NC02}|^2}{|\mathcal{M}_{all}|^2} > 0.5 \quad (7.1)$$

This ensured a pure NC02 signal sample, since the other contributing non-NC02 processes get clearly separated (see Fig. 7.3).

7.2 Track selection and pre-selection

Typically, a common particle selection is applied first to assure minimal reconstruction quality. The common track selection used in most DELPHI analyses is based on Skelana[SS97] and asks for the following particle criteria:

- charged momentum greater than 100 MeV
- charged particles have to originate from within 4 cm in the transverse plane and within $\frac{4 \text{ cm}}{\sin \theta}$ along the beam axis, depending on the polar angle θ
- neutral clusters with more than 300 MeV in the HPC¹ and STIC², or with more than 400 MeV in FEMC³

7.2.1 Data quality cuts

Since during data taking it can happen, that not all subdetectors are online, special quality flags have been introduced. These quality indicators assure, that all subdetectors were operational during recording of a specific data event.

For this analysis, only data events with all subdetectors being in an acceptable condition have been used. For analyses exploiting missing energy signatures, this is crucial, since faulty or missing subdetector readouts might lead to signal-like misinterpretations of data events.

¹barrel electromagnetic calorimeter

²very forward electromagnetic calorimeter

³forward electromagnetic calorimeter

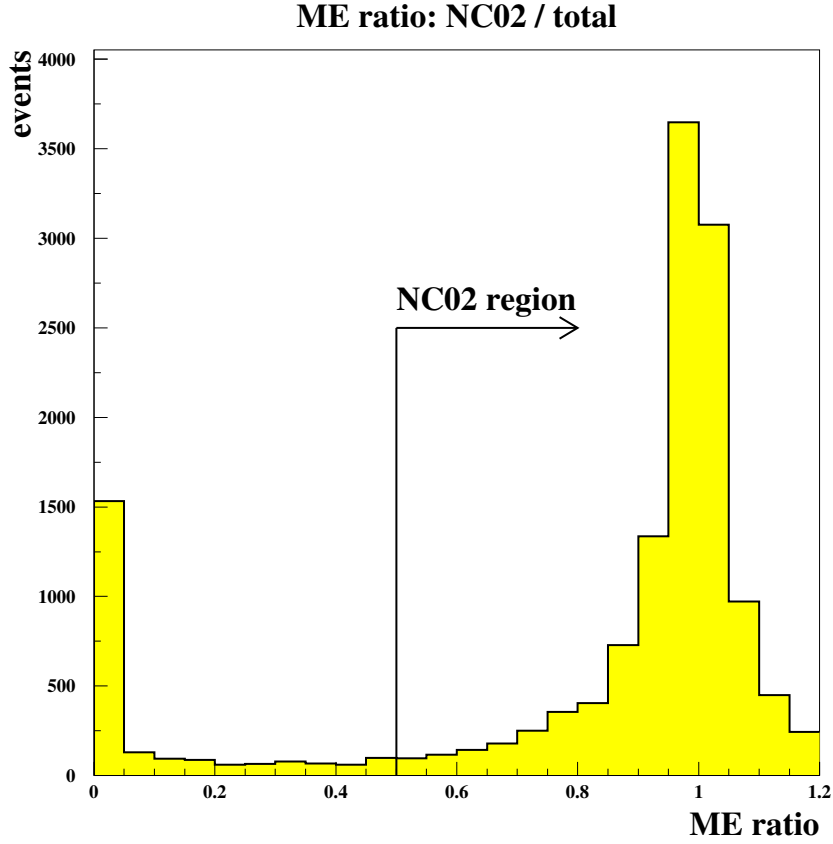


Figure 7.3: Ratio of NC02 matrix elements to all contributing matrix elements calculated from the four-vector of the final state fermions. This was done in order to purify MC signal samples from other non-NC02 contributions.

7.2.2 Anti-two-photon and anti-Bhabha cuts

In addition to this analysis independent selection, it was necessary to remove the Bhabha and two-photon backgrounds due to their high cross-sections, by applying a loose hadronic preselection. These cuts were common to both analyses studied in this thesis and assured a good background suppression while not touching the signal. This was achieved by firstly requiring at least two charged particles with transverse momentum greater than 2 GeV, originating from within 1 mm in the transverse plane and 3 mm along the beam axis. After this quality cut, a loose hadronic preselection is applied asking for the following event properties:

- at least **eight charged particles**

- **charged energy** greater than $0.16\sqrt{s}$
- **transverse energy** greater than $0.15\sqrt{s}$
- sum of all **particle momenta along thrust axis** greater than $0.25\sqrt{s}$
- **energy of electromagnetic shower** below $0.45\sqrt{s}$

This results in a complete suppression of Bhabha events and a 97% reduction of the two-photon background.

7.2.3 Anti-two-fermion and anti- WW cuts

The aim of the next set of cuts was the reduction of the two-fermion final state background. This process can have some missing energy signature due to initial state photons lost in the beam pipe or other insensitive regions of the detector. Each event had to satisfy the following conditions:

- effective centre-of-mass energy $\sqrt{s'}$ greater than 115 GeV for polar angles less than 40° or greater than 140°
- **electromagnetic energy within $\theta < 30^\circ$** had to be less than $0.16\sqrt{s}$
- total **energy deposition in STIC⁴** detector had to be less than $0.08\sqrt{s}$
- no veto coming from **hermiticity counters**
- effective centre-of-mass energy $\sqrt{s'}$ less than $0.96\sqrt{s}$
- coplanar events with **acoplanarity** (definition see 7.3) less than 10° were required to have no jets in $35^\circ < \theta < 45^\circ$ or $135^\circ < \theta < 145^\circ$

These cuts removed about 88% of the total two-fermion background.

Processes leading to four-fermion final states via a pair of W-bosons also contribute to the total background. Hence, another set of preselection cuts was applied in order to discriminate semi-leptonic decays, which can easily mimic missing energy events.

- **most energetic particle** less than $0.2\sqrt{s}$
- no **charged particle with transverse momentum to closest jet** greater than 10 GeV
- momentum of **most isolated particle** in the range $0.01\sqrt{s} < p < 0.20\sqrt{s}$

⁴Small angle Tile Calorimeter: used as luminosity monitor

- **visible mass** smaller than \sqrt{s}

These four requirements removed about 80 % of the background originating from WW . At this stage of the analysis the signal efficiency left was about 74 %.

7.3 Selection variables and tail cuts

In order to further isolate the signal from background, a combined discriminant variable was constructed from twelve input variables using the iterated discriminant analysis technique described in section 5.2. These variables have been chosen according to their discriminating power and correlation.

Since discriminant analyses require input variables to be Gaussian shaped in order to achieve the best discrimination power, a set of loose tail cuts was applied in addition to the preselection cuts described in the previous section. They reduced the signal efficiency by only 1.5 %. Each cut is mentioned along with the description of the corresponding input variable.

- **logarithm of transverse momentum** with respect to the beam axis
- **visible energy** normalized to \sqrt{s} for values smaller than one
- **transverse energy** with respect to the beam axis normalized to \sqrt{s} for values in the range of 0.15 - 0.60
- **minimum polar angle** common to a pair of cones to the positive and negative beam direction respectively, which contain 6% of the total visible energy
- **difference of the jet energies** of an event forced to two jets normalized to \sqrt{s} . Values had to be smaller than 0.35
- **sum of particle energies in a double cone** around the most isolated particle normalized to \sqrt{s} . For all particles with at least 2 GeV momentum a double cone is defined with an inner angle of 5° and an outer angle α_{max} depending on the particle momenta. For particles in the range of 2 GeV to 5 GeV $\alpha_{max} = 60^\circ$ is chosen and for particle momenta above 5 GeV $\alpha_{max} = 25^\circ$ is used. The particle with the smallest ratio of total energy in the defined cone to its momentum is considered the most isolated particle. This cone-energy was required to be below 0.15
- **effective centre-of-mass energy** $\sqrt{s'}$

- **logarithm of product of acoplanarity and interjet angle** forcing all events to two jets. Acoplanarity is defined as interjet angle of the projection to the plane orthogonal to the beam axis. Variable values were required to be lower than 2.80
- **logarithm of the acolinearity.**
- **longitudinal momentum** with respect to the thrust axis, normalized to \sqrt{s} , for values lower than one
- **logarithm of the largest transverse momentum** of any particle with respect to its jet direction
- **missing mass** normalized to \sqrt{s} , constraining the visible mass to be compatible with m_Z .

The missing mass, used as last variable in the selection listed above, can be constructed from the observed quantities E_{vis} and p_{vis} in the following way:

$$\begin{aligned} m_{mis} &= \sqrt{E_{mis}^2 - p_{mis}^2} \\ m_{mis} &= \sqrt{(\sqrt{s} - E_{vis})^2 - p_{vis}^2} \end{aligned} \quad (7.2)$$

The centre-of-mass energy \sqrt{s} is well known and precisely measured. A significant improvement in discrimination power can be achieved by calculating the missing mass with the constraint of the visible mass being compatible with m_Z . One possibility to achieve this is to simply introduce a scaling factor $\alpha = \frac{m_Z}{m_{vis}}$:

$$\begin{aligned} m_Z = \alpha m_{vis} &= \sqrt{(\alpha E_{vis})^2 - (\alpha p_{vis})^2} \\ E_{vis} \longrightarrow \alpha E_{vis} \quad \wedge \quad p_{vis} \longrightarrow \alpha p_{vis} \\ m_{mis} &= \sqrt{(\sqrt{s} - \alpha E_{vis})^2 - \alpha^2 p_{vis}^2} \end{aligned} \quad (7.3)$$

A missing mass distribution calculated using equation 7.3 is shown on Fig. 7.4 lower right.

The distributions of these twelve variables were found to be in good agreement with the simulation predictions at each centre-of-mass energy analysed. This is illustrated by Fig. 7.4, where the four most discriminant variables are shown after all preselection cuts had been applied using data and MC at 189 GeV centre-of-mass energy.

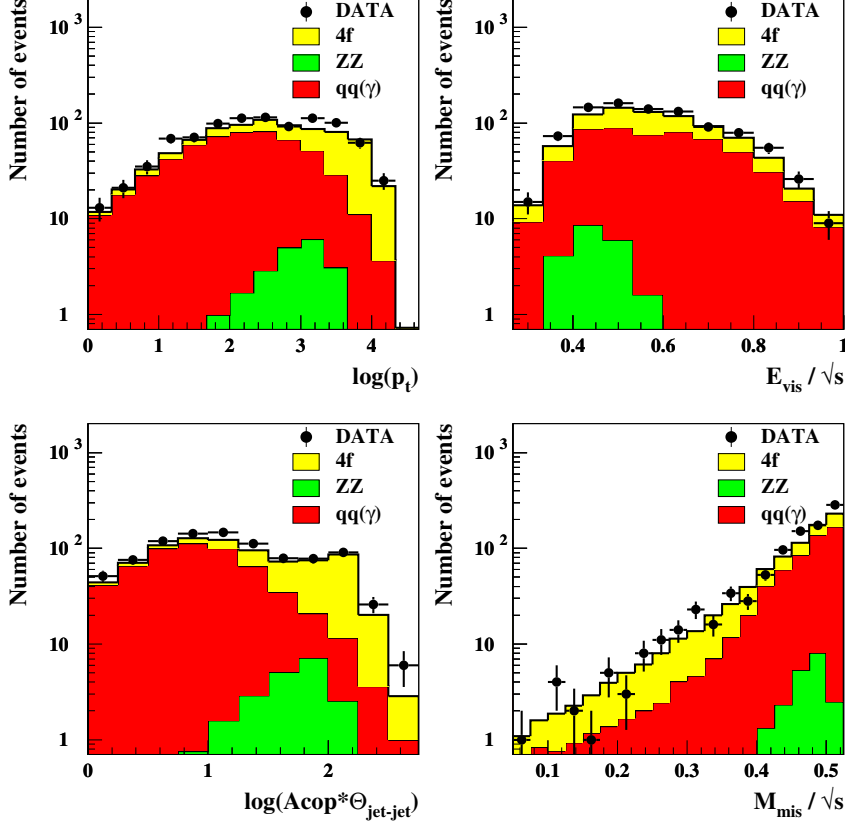


Figure 7.4: The four most discriminant input variables for the discriminant analysis at 189 GeV centre-of-mass energy. Illustrated are real data, the ZZ signal and the two most significant background channels: two-fermion and four-fermion final state processes.

7.4 The iterated discriminant analysis

After having applied all preselection cuts described in the previous sections, the twelve input variables were used to calculate the final discriminant variable according to the IDA technique described in detail in chapter 5.2.

In order to have an independent simulation sample to calculate the coefficients for the discriminant analysis, all simulation samples were split in two halves: the first part was used to derive the coefficients, while the second part was used to perform the analysis by predicting background and signal processes.

The output variable of the first iteration step is then used to further reduce

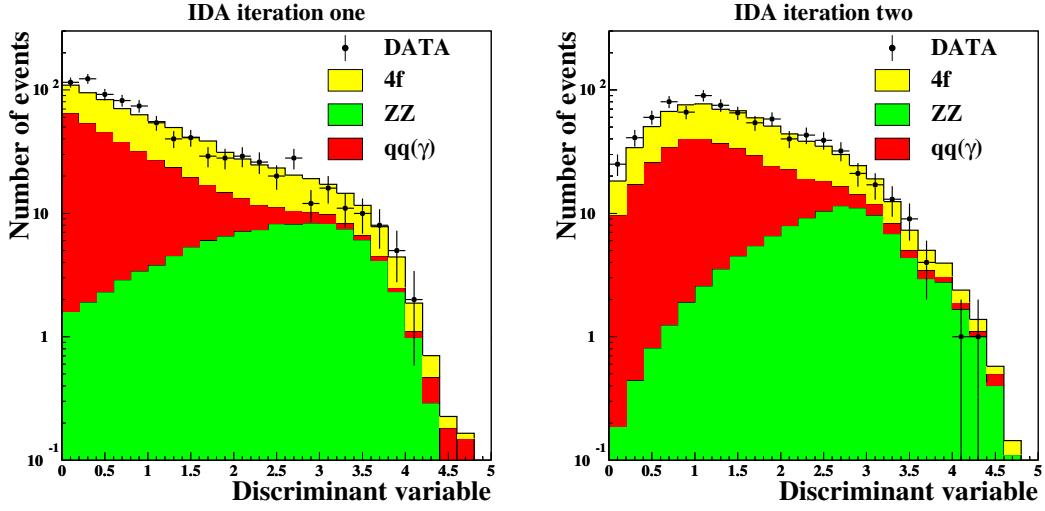


Figure 7.5: The two output distributions (183 GeV - 208 GeV) of the iterated discriminant analysis after each iteration step. Illustrated are real data, the ZZ signal and the two most significant background channels: two-fermion and four-fermion final state processes.

the amount of background events by placing a cut such that not more than 5% signal efficiency is lost. This cut results in a reduced background contamination and the coefficients are recalculated using the same twelve variables as input. This results in a new discriminant output distribution, which is used to further discriminate the background by applying another cut, which does not reduce the signal efficiency any further. Hence the cut on the output of this second and last iteration step only removes pure background events.

The output of each step of the iterated discriminant analysis combining all relevant energies (183 GeV – 208 GeV) are shown on Fig. 7.5, after each of the corresponding cuts had been applied. Both distributions show a good agreement of data and simulation, especially in the ZZ signal region. There is a slight data excess visible for the second iteration plot on the right hand side, but these four consecutive bins are in the non-signal region and hence do not perturb the extraction of the NC02 cross-section.

Performance curves showing the evolution of data and simulation agreement depending on the signal efficiency are shown in appendix A for all energies analysed.

The final discriminant output distributions were later used to extract the NC02 cross-section contribution for the channel $ZZ \rightarrow q\bar{q}\nu\bar{\nu}$ by performing a maximum Likelihood fit as described in section 5.4.

\sqrt{s} [GeV]	Systematic error from energy flow	Systematic error from MC cross-sections
183	$\pm 14.5\%$	$\pm 4.0\%$
189	$\pm 10.0\%$	$\pm 2.5\%$
192	$\pm 7.5\%$	$\pm 2.5\%$
196 – 208	$\pm 3.5\%$	$\pm 2.5\%$

Table 7.2: Expected effects from the fitted $ZZ \rightarrow q\bar{q}\nu\bar{\nu}$ cross-section from uncertainties in the energy flow reconstruction and predicted background cross-sections.

7.5 Systematic errors and working point

For this analysis two main sources for systematic errors were taken into account:

- simulation of the energy flow through the detector using the shaking technique
- uncertainties in MC generator cross-sections for the processes: WW , $W\ell\nu$ and $Z\gamma$

The systematic error from uncertainties in the energy flow reconstruction was extracted by applying the shaking technique to all relevant background simulation topologies separately (two-fermion samples, four-fermion samples, signal samples and the sum of the other topologies) and repeating the analysis each time using the full LEP II statistics relevant for this process (from 183 GeV up to 208 GeV). The main effect on the resulting cross-section was found to come from two-fermion final states processes, which was increased by about one third compared to the amount of expected events using unshaken simulation samples. Other topologies were affected in the same way, but much less. This can be understood from the fact that two-fermion events have a rather low signal affinity. Hence the analysis will only pick up two-fermion events that suffered a lot from a poor reconstruction, leading to some signal-likeness. Consequently, this topology is affected most by the shaking technique.

Given the conclusion of the chapter describing the shaking, the differences in the expected results from shaken and unshaken simulations were taken as conservative estimation of the systematic uncertainty. The total systematic uncertainty was constructed by adding each contribution in quadrature, assuming only negligible correlations between the different topologies.

Since the shaking corrections were always of the same sign, the resulting error was taken $\pm \frac{1}{2}$ the uncertainty, with the resulting cross-section being shifted by $\frac{1}{2}$ of the effect. This resulted in the energy dependent errors listed in Tab. 7.2 along

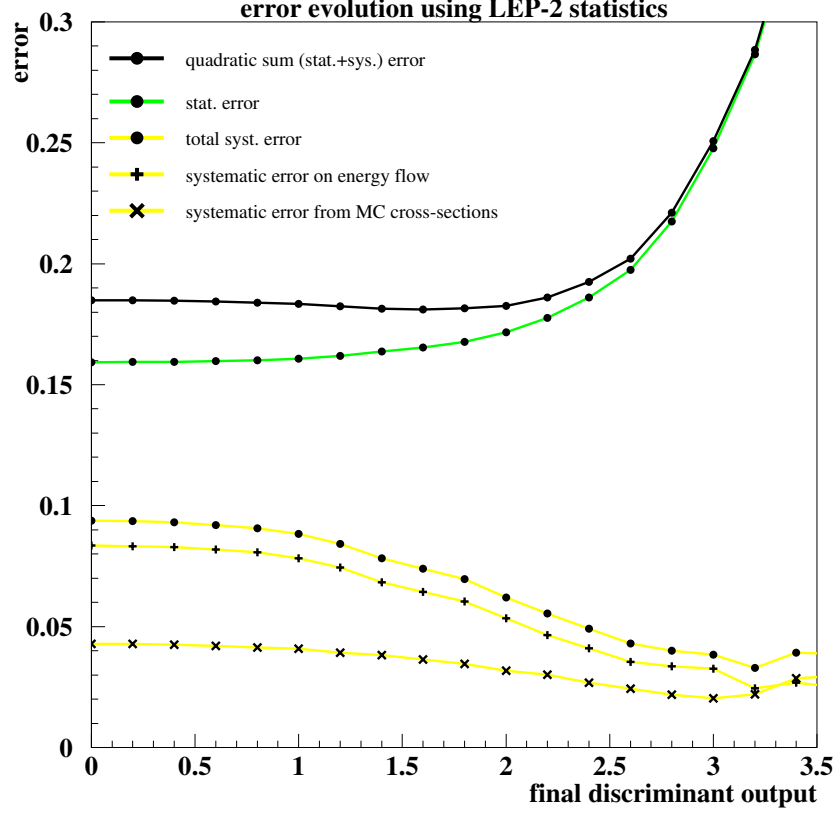


Figure 7.6: Overview of statistical and systematic errors in a $ZZ \rightarrow q\bar{q}\nu\bar{\nu}$ analysis. The lines with bullet symbols represent the total errors, while the lines with cross symbols show the two contributions to the total systematic error.

with the systematic errors resulting from simulation cross-section uncertainties. The latter have been deduced by rerunning the analysis with shifted simulation cross-sections, assuming the following uncertainties [A⁺00]:

- $WW : \pm 2\%$
- $W e \nu : \pm 5\%$
- $Z\gamma : \pm 2\%$

Clearly, the effect coming from the energy flow reconstruction is dominant. Since at low centre-of-mass energies (183 GeV and 189 GeV) two-fermion final state events tend to be more signal-like, they contribute much more to the final back-

ground composition and hence, lead to a higher systematic error compared to higher centre-of-mass energies (see Tab. 7.2).

Fig. 7.6 gives an overview of the two contributing systematic errors and the statistical error depending on the final discriminant variable output. This information was used to determine a working point for the $ZZ \rightarrow q\bar{q}\nu\bar{\nu}$ analysis by choosing an output value such that the quadratic sum of both errors (total systematic and statistical errors) is minimal. Since the evolution of the total error is very flat up to a discriminant output of **2.2**, this point was chosen as working point since it provides a high purity while not yet suffering from a big overall error.

7.6 The resulting cross-sections

For each centre-of-mass energy analysed, the final cross-section was extracted by performing a binned maximum Likelihood fit of the simulation expectation to data (see chapter 5.4). The resulting fit parameter a corresponds to a multiple of the Standard Model (SM) cross-section used for the MC simulation. It is hence very easy to extract the measured cross-section from the fit result:

$$\sigma_{fitted} = a * \sigma_{SM} \quad (7.4)$$

The fit was performed using all bins of the final discriminant output with values greater than the chosen working point. This lead to the cross-section results

\sqrt{s} [GeV]	lumi. [pb^{-1}]	backgr. only	total MC simulation	data	signal efficiency	cross-section [$pb \pm stat. \pm syst.$]
183	52.4	5.0	7.0	9	45.0 %	$0.05 \pm 0.13 \pm 0.01$
189	152.8	33.3	49.5	51	58.7 %	$0.12 \pm 0.07 \pm 0.02$
192	24.9	9.4	12.8	14	64.4 %	$0.08 \pm 0.24 \pm 0.02$
196	75.0	13.3	22.6	27	51.5 %	$0.38 \pm 0.15 \pm 0.01$
200	82.2	14.5	25.7	22	51.3 %	$0.18 \pm 0.13 \pm 0.01$
202	40.4	4.0	8.1	9	35.8 %	$0.37 \pm 0.24 \pm 0.01$
205	72.9	9.8	18.6	14	43.0 %	$0.21 \pm 0.14 \pm 0.01$
207	183.4	17.4	28.7	27	54.0 %	$0.29 \pm 0.11 \pm 0.01$
						$\sigma_{obs.}/\sigma_{SM}$
183 -207	639.0	106.7	173.0	173	–	$0.78 \pm 0.15 \pm 0.05$

Table 7.3: An overview of the results obtained at each energy for the $ZZ \rightarrow q\bar{q}\nu\bar{\nu}$ cross-section analysis. In case of the combination, the ratio of observed and expected cross-sections is presented along with the corresponding errors

ZZ to $q\bar{q}\nu\bar{\nu}$

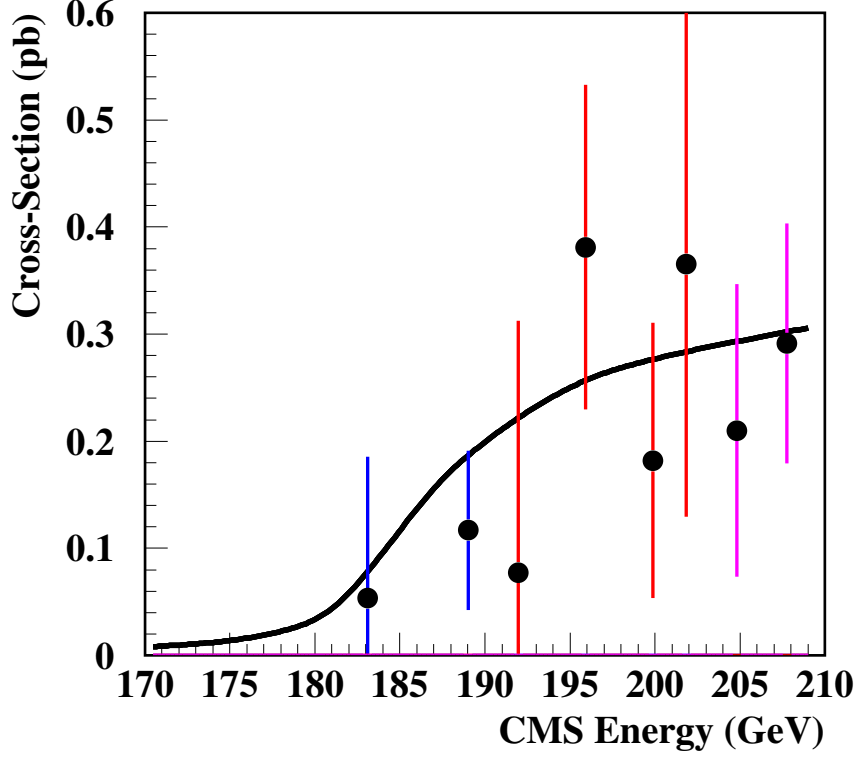


Figure 7.7: The obtained $ZZ \rightarrow q\bar{q}\nu\bar{\nu}$ cross-sections (NC02 * branching ratio) for each energy. The error bars represent the quadratic sum of statistical and systematic errors, while the solid line corresponds to the theoretical Standard Model expectation simulated with YFSZZ[SJW97].

presented in Table 7.3 including statistical and systematic errors. The effects from shifting the results due to one-sided systematic errors from uncertainties in the energy flow have been applied as well.

Table 7.3 clearly shows that the analysis is dominated by statistical uncertainties. The resulting cross-sections tend to be below the Standard Model expectation by approximately 1.4σ , which is still compatible with the expectation.

Fig. 7.7 illustrates the energy dependant evolution of the $ZZ \rightarrow q\bar{q}\nu\bar{\nu}$ cross-section. The measured data points follow the theoretical expectation and do agree well within their systematic and statistical uncertainties.

The results from this analysis were combined with the results from six further

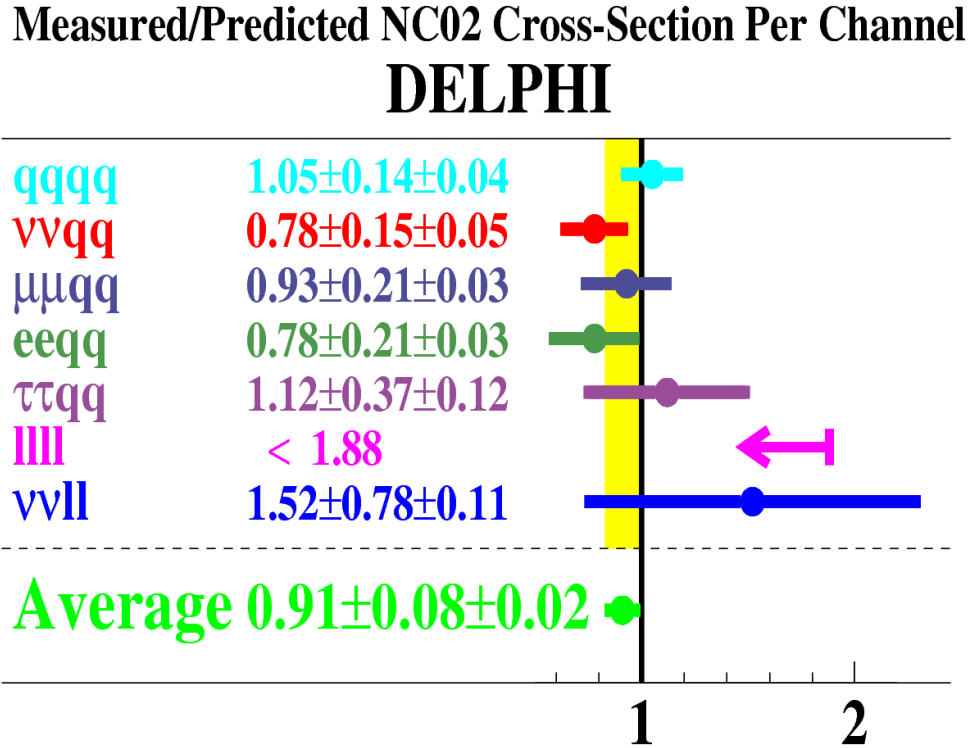


Figure 7.8: Overview of the results obtained in each of the channels analysed by DELPHI in order to measure the NC02 production cross-section. The numbers correspond to the ratio of measured to predicted cross-sections with the vertical band representing the total error on the combination [DEL03].

analyses concentrating on the different decay channels of the doubly resonant Z^0 pair production. A detailed description of each analyses and the corresponding results can be found in the DELPHI paper [DEL03] about the NC02 cross-section measurement. Fig. 7.8 was taken from this publication and gives a nice overview of the results obtained in each channel and their combination. It shows the ratio of observed and expected cross-sections, which do agree reasonably well with the Standard Model expectation.

Chapter 8

Search for bosonic Higgs decays

According to the Standard Model, bosons acquire their masses directly by coupling to the Higgs field, while fermions need an extra free parameter, the so-called Yukawa coupling (see chapter 2.5). Due to their high on-shell masses, Higgs decays to W^\pm and Z^0 bosons only have a rather low cross-section in the energy range accessible for LEP. That is why most searches focus on fermionic Higgs decays. Since the Yukawa coupling directly depends on the fermion masses, Higgs decays to a pair of heavy b-quarks are the most promising candidates.

However, the coupling of the Higgs to W^\pm and Z^0 bosons is very fundamental to the Higgs mechanism, since it allows to search for the Higgs bosons independently from the Yukawa coupling, which has to be adjusted manually in order to create a model consistent with observations. This renders the search for bosonic Higgs decays an interesting complement to the standard Higgs searches for fermionic decays.

At LEP, the Standard Model Higgs boson is mainly produced via the so-

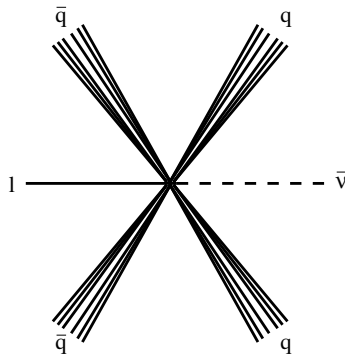


Figure 8.1: Schematic presentation of the process $ZWW \rightarrow qq\bar{q}\bar{q}l\bar{\nu}$ leading to two quark jets, one lepton and missing energy.

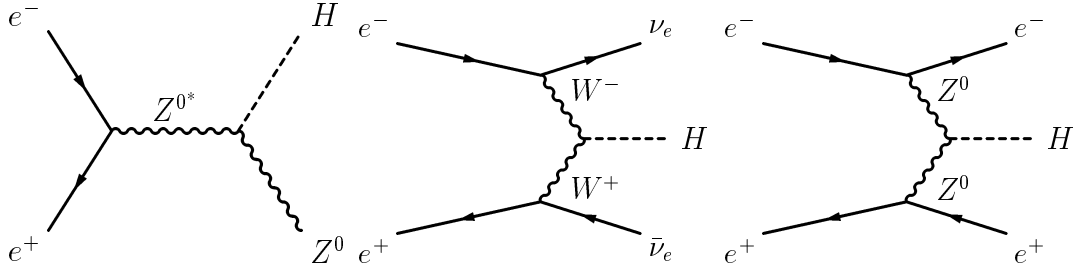


Figure 8.2: Higgs production via Higgs-Strahlung (left), W^+W^- fusion (middle) and Z^0Z^0 fusion (right) at LEP.

called Higgs-Strahlung process (see Fig. 8.2). Here the initial electron-positron pair annihilates and forms a highly off-shell Z^{0*} boson, which transforms into an on-shell Z^0 by radiating a Higgs boson. LEP provided centre-of-mass energies up to 208 GeV, which kinematically allows the production of Higgs bosons up to a mass of about 116 GeV using this production channel.

In addition to the dominant Higgs-Strahlung process, two further Higgs production channels via boson fusion are possible within an e^+e^- environment like LEP: W^+W^- fusion and Z^0Z^0 fusion (see Fig. 8.2). Up to its kinematic limit, the Higgs-Strahlung process is dominating the W^+W^- fusion cross-section by more than a magnitude. In the case of Z^0Z^0 fusion the resulting cross-section contribution is another magnitude smaller compared to W^+W^- fusion due to a smaller vertex factor. Beyond the kinematic limit, the remaining Higgs production is coming mainly from fusion processes, but the total cross-section is very small and dies off quickly [KKZ96].

In this thesis only Higgs decays to a pair of W bosons via the Higgs-Strahlung process are taken into account since these offer by far the most promising cross-sections.

Fig. 8.3 illustrates the Standard Model branching ratio of the Higgs boson to the different bosonic and fermionic final states depending on the Higgs mass. The dominance of $H \rightarrow b\bar{b}$ for Higgs masses below 100 GeV is clearly visible. However, between 100 GeV and the kinematic limit of about 116 GeV the decay $H \rightarrow W^+W^-$ quickly gains importance and reaches a branching fraction of about 8% assuming a Higgs mass of 116 GeV.

Bosonic Higgs decays are not only interesting with respect to the Standard Model, they also play an important role in extended models like the 2 Higgs Doublet Model (2HDM). In the so-called “Type I” 2HDM models one doublet couples to fermions only, while the other doublet couples exclusively to bosons. This results in five Higgs bosons: 2 charged Higgses H^\pm , one CP-odd A and two CP-even Higgs bosons H and h .

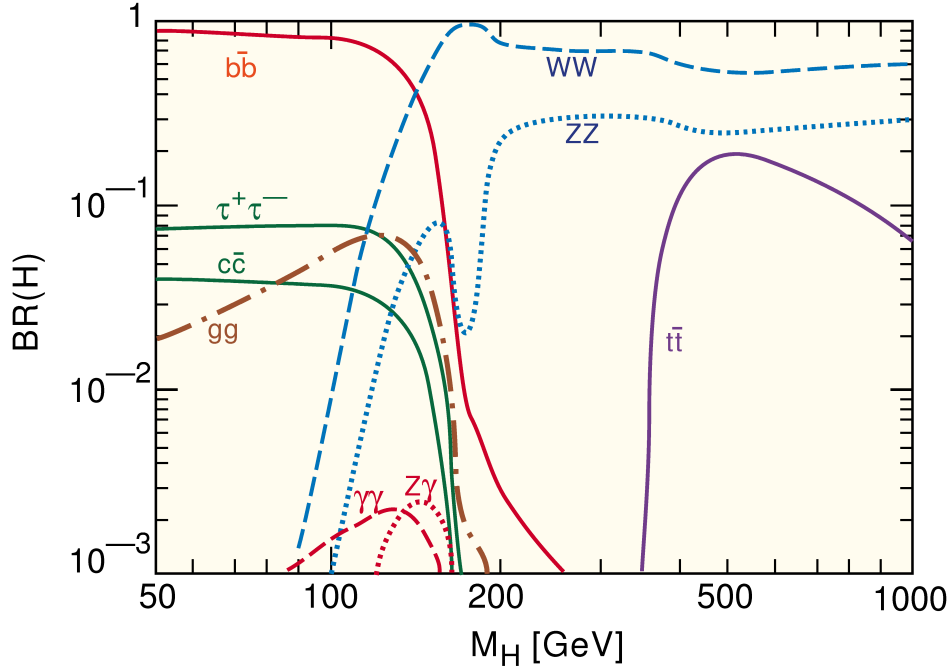


Figure 8.3: The branching ratio of SM Higgs boson decays to bosonic and fermionic final states, depending on the Higgs mass.

Typically, only the lightest of these Higgs bosons (h) is accessible with LEP energies in such scenarios. Since the light h is a linear combination of the two Higgs doublets, one can choose the mixing parameter such that h is made up of only one doublet: the one which couples exclusively to bosons. Consequently such a Higgs would exclusively decay to bosons and only an analysis searching for bosonically decaying Higgs bosons would be sensitive at all. A nice overview of these extended models and their role in the context of searches for bosonic Higgs decays is given in [Sta03].

8.1 Signal topologies

The bosonic Higgs decay to a pair of W bosons via Higgs–Strahlung offers a large amount of combinatoric signal topologies. Nevertheless, there are only few decay modes with sizable branching fractions:

- $Z^0 H \rightarrow Z^0 W^+ W^- \rightarrow q\bar{q}q\bar{q}q\bar{q}$: Fully hadronic final states with a branching ratio of **32 %**
- $Z^0 H \rightarrow Z^0 W^+ W^- \rightarrow q\bar{q}q\bar{q}l_{e,\mu}\bar{\nu}_{e,\mu}$: 4 hadronic jets accompanied by an electron or muon lepton and missing energy resulting in a branching of **20 %**

- $Z^0 H \rightarrow Z^0 W^+ W^- \rightarrow q\bar{q}q\bar{q}\tau\bar{\nu}_\tau$: 4 hadronic jets accompanied by a tau-lepton and missing energy resulting in a branching ratio of **10 %**
- $Z^0 H \rightarrow Z^0 W^+ W^- \rightarrow \nu\bar{\nu}q\bar{q}q\bar{q}$: 4 hadronic jets and missing energy resulting in a branching ratio of **9 %**

The channel $Z^0 H \rightarrow Z^0 W^+ W^- \rightarrow q\bar{q}q\bar{q}l_{e,\mu}\bar{\nu}_{e,\mu}$ with the second highest branchings fraction of approximately 20 % was studied in this thesis. Since kinematics forces one of the two W bosons to be highly virtual (off-shell), one has to distinguish between two different topologies for this semileptonic channel.

In the first case the off-shell W decays leptonically, while the remaining on-shell Z^0 and W^\pm bosons decay hadronically. This leads to four high energetic jets accompanied by a soft electron or muon and few missing energy. However, due to its low energy the lepton tends to get lost in neighbouring jets which makes it difficult to distinguish from especially di-boson background sources. Here mainly hadronically decaying W pairs contributed to the background sources. The corresponding decays from Z^0 pairs do also contribute, but their production cross-section is a factor of 20 smaller compared to W^+W^- .

In the second case however, the on-shell W boson is decaying leptonically with the Z^0 and the off-shell W leading to hadronic final states. Here typically two high energetic jets, an easy to identify electron or muon and a sizeable amount of missing energy together with a pair of soft jets are produced. The latter are usually not easy to identify, but the high energetic lepton is a key signature for identifying this signal topology. Main backgrounds arise from semileptonic W^+W^- decays.

For each of these two cases a separate simulation sample has been created in order to provide optimal background discrimination.

8.2 Data and simulation samples

Since the branching ratio of Higgs to bosonic final states rises quickly with the Higgs mass (see Fig. 8.3), the data analysed was chosen in order to provide a centre of mass energy such that the kinematics of the Higgs–Strahlung process allows a Higgs mass of at least 100 GeV. Therefore data samples ranging from 196 GeV taken in 1999 up to 208 GeV taken end of 2000 have been used, corresponding to a total luminosity of $408.9pb^{-1}$.

In order to isolate a possible Higgs signal from other processes a set of MC simulations was produced using different simulation packages optimised for each channel. The following programs were used for this analysis:

- KK2F[JWW00] generated the two-fermion final states processes including initial state radiation
- WPHACT[AB97] was used for all four-fermion like final state processes
- HZHA[Jan96] simulated the Higgs-Strahlungs processes with bosonic Higgs decays for the following Higgs masses: 95 GeV, 100 GeV, 102.5 GeV, 105 GeV, 107.5 GeV, 110 GeV, 112.5 GeV, 115 GeV and 120 GeV

Again, more than 100 times the statistics seen in data has been produced in order to assure only negligible statistical errors in the simulation samples.

8.3 Track selection and pre-selection

Track selection and data quality cuts were in common with the ZZ cross-section measurement analysis and can be looked up in section 7.2. Also the anti-two-photon and anti-Bhabha cuts were the same and resulted in a complete suppression of Bhabha events and in a 97% reduction of the two-photon background.

One additional quality criterium was imposed by asking for at least one identified lepton (electron or muon only).

8.3.1 Anti-two-fermion and anti-four-fermion cuts

Basically, two main sources of background processes remain at this level of the analysis, common for both signal topologies: two-fermion final state processes and four-fermion final state processes. The following set of cuts were applied sequentially in order to reduce the contamination from both background sources.

- **charged multiplicity** was required to be greater than 22 particles per event. This cut mainly discriminated two-fermion final state processes
- **$\ln y_{34}$** , the logarithm of the distance cut-off value y_{cut} where an event migrates from three-jets to four-jets using the DURHAM cluster algorithm. This value was required to be greater than -5.0 and helped in rejecting the two-fermion background and the semi-leptonic four-fermion background.
- the transverse energy E_t was asked to be greater than $0.35\sqrt{s}$
- the effective centre-of-mass energy $\sqrt{s'}$ was required to be greater than $0.6\sqrt{s}$ in order to veto two-fermion final state events with an initial state radiation signature.

reduction	two-fermion	WW like	ZZ like	signal
on-shell analysis	99 %	95 %	88 %	21 %
off-shell analysis	83 %	55 %	91 %	8 %

Table 8.1: The amount of background suppression for the three main background sources and the loss of signal efficiency for both Higgs decay channels.

- **energy of most energetic lepton** was used to distinguish between the two signal topologies by splitting all data and simulation samples into two analyses. Events with a most energetic lepton of more than $0.1\sqrt{s}$ were accepted in the case of the on-shell analysis¹, optimised for leptonic decays of the on-shell W . The corresponding off-shell analysis² required that no lepton had more energy than $0.1\sqrt{s}$. This assures, that no event overlap exists between the two analyses.
- the χ^2 of a kinematic fit to 4 four-vectors consisting of 2 hadronic jets, one lepton and missing energy/momentum. As constraints, energy and momentum conservation were required and the invariant masses of two four-vector pairs had to be compatible with the W on-shell mass. Since there are three combinatorial possibilities to pair the 4 four-vectors, only the pairing resulting in the lowest χ^2 was accepted. In case of the on-shell analysis the resulting minimal χ^2 value was used to veto semileptonic WW decays by removing all events with a χ^2 smaller than 25.

These cuts resulted in a strong background suppression for both analyses (see Tab. 8.1). The rather high loss of signal efficiency in case of the on-shell analysis is due to the requirement of a high energetic lepton, which can escape detection due to limitations of the lepton identification.

8.4 Channel with on-shell W decaying leptonically

This channel is characterised by a high energetic lepton, which leads to a rather easy to identify signal topology. Consequently, it is expected to provide a higher performance compared to the second bosonic Higgs decay channel analysed in this thesis.

¹ $ZH \rightarrow ZW^*W \rightarrow q\bar{q}(q\bar{q})^* l_{e,\mu}\bar{\nu}_{e,\mu}$

² $ZH \rightarrow ZWW^* \rightarrow q\bar{q}q\bar{q} (l_{e,\mu}\bar{\nu}_{e,\mu})^*$

8.4.1 Selection variables

The final step in the discrimination chain was performed by an iterated discriminant analysis (see chapter 5.2) using 9 input variables. Due to the cuts applied during preselection, it was not necessary to impose further tail cuts.

- **ln y_{34}** , the logarithm of the distance cut-off value y_{cut} , when an event migrates from three-jets to four-jets using the DURHAM cluster algorithm.
- **ln y_{45}** , the logarithm of the distance cut-off value y_{cut} , when an event migrates from four-jets to five-jets using the DURHAM cluster algorithm.
- **minimum interjet angle** forcing all events to four jets
- **reconstructed Higgs mass** using a kinematic fit with five constraints (energy, momentum and invariant mass of one jet pair compatible with m_Z) for a topology with four jets, one lepton and missing energy/momentum
- **visible mass** normalised to the the centre-of-mass energy (\sqrt{s})
- **logarithm of the acolinearity**
- **longitudinal momentum** with respect to the thrust axis, normalised to \sqrt{s}
- **energy of most energetic lepton** normalised to \sqrt{s}
- **charged multiplicity**

All nine input variables were found to describe data in a reasonable way at all centre-of-mass energies analysed. The distributions of the four most significant input variables are shown on Fig. 8.4 after all preselection cuts had been applied. They confirm a good agreement of data and simulation prescription. From these plots, one can conclude, that the ZZ like background contributes the most at this level of the analysis. The expected signal region was magnified by a factor of ten for better visualisation.

8.4.2 Iterated discriminant analysis

The nine input variables were used to calculate the final discriminant variable using the iterated discriminant analysis technique described in chapter 5.2. As for the ZZ cross-section measurement, the outcome of the first iteration step was used to discriminate the background contributions by imposing a cut such that only 5 % signal efficiency got lost. For the second iteration step, the resulting

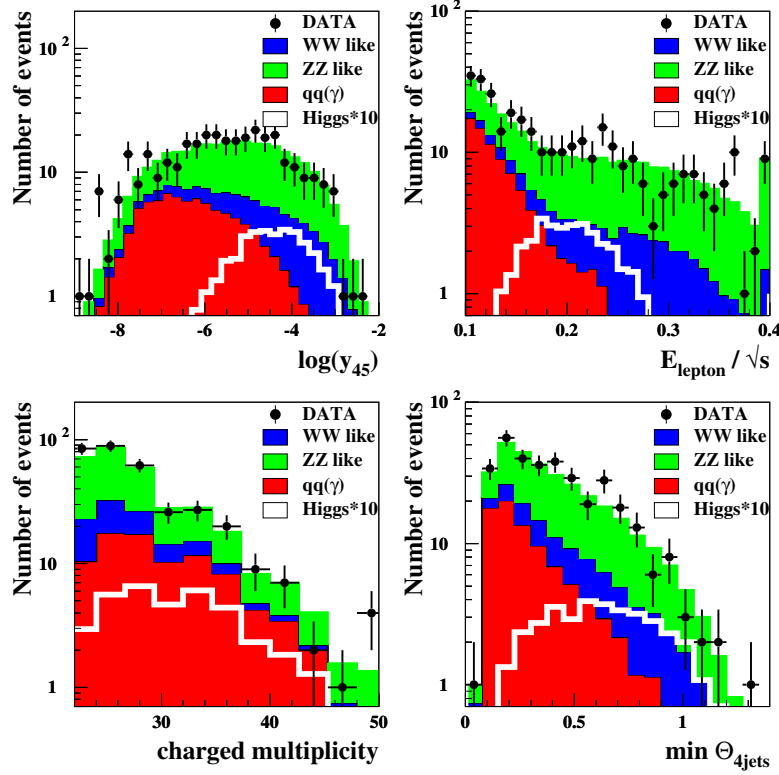


Figure 8.4: ZWW on-shell: The four most discriminant input variables for the discriminant analysis combining 196 – 207 GeV centre-of-mass energy. Illustrated are real data, the expected Higgs signal with a mass of 105 GeV (magnified by a factor 10 for better visualisation) and the three most significant background channels: two-fermion, WW like and ZZ like processes.

nine input variable distributions were used to calculate the second IDA output variable.

As a working point for both analyses an efficiency of 40 % was chosen, since the effect on the expected limit of the Higgs mass turned out to be rather independent from the working point imposed. The resulting IDA distribution at an efficiency of 40 % can be seen on the left hand side of Fig. 8.5, together with the reconstructed Higgs mass on the right hand side.

The background composition at the final level of the analysis is similar to what was observed at preselection level: ZZ like processes dominate the picture with some contribution from WW like processes. Although both distributions show

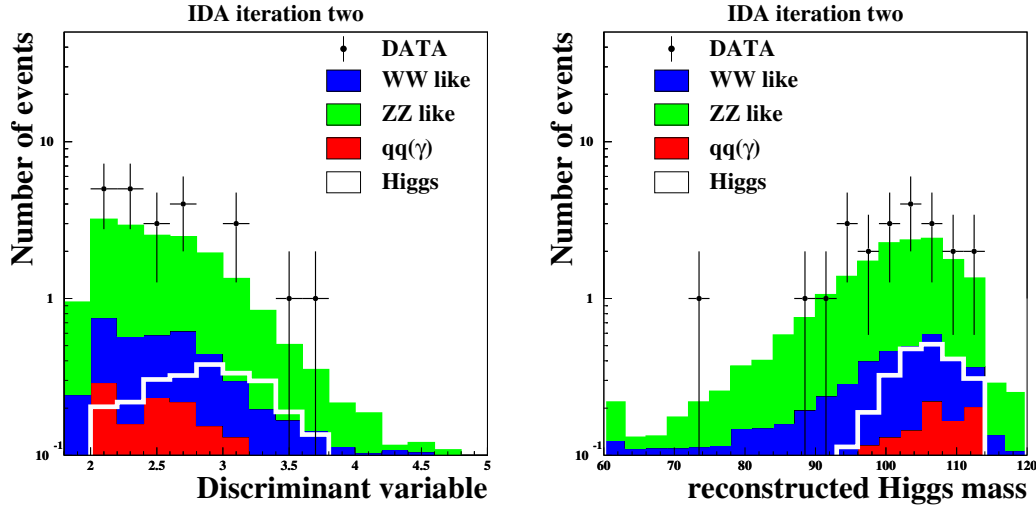


Figure 8.5: The final output distributions (196 GeV - 208 GeV) of the iterated discriminant analysis and the resulting Higgs mass reconstruction. Illustrated are real data, the expected Higgs signal with a simulated mass of 105 GeV and the three most significant background channels: two-fermion, WW like and ZZ like processes.

a reasonable agreement between data and the simulation, there are two events with a high IDA output value. Both were investigated closely with the DELPHI event visualisation program DELGRA[BCG⁺00] (see Fig. 8.13 and Fig. 8.14 at the end of this chapter) resulting in the following topological properties:

- one isolated high energetic muon (μ^+) pointing to the barrel region of the detector.
- a sizable amount of missing momentum pointing away from the muon.
- two jets resulting in an invariant mass compatible with a reconstructed on-shell Z^0 boson.
- two jets with a reconstructed invariant mass compatible with an off-shell W boson.

The kinematic properties of both events are summarised in the following table including the reconstructed masses of the three final bosons and the Higgs boson. These have been calculated from a five constraints kinematic fit, asking for momentum and energy conservation as well as an invariant mass of one jet-pair compatible with an on-shell Z^0 .

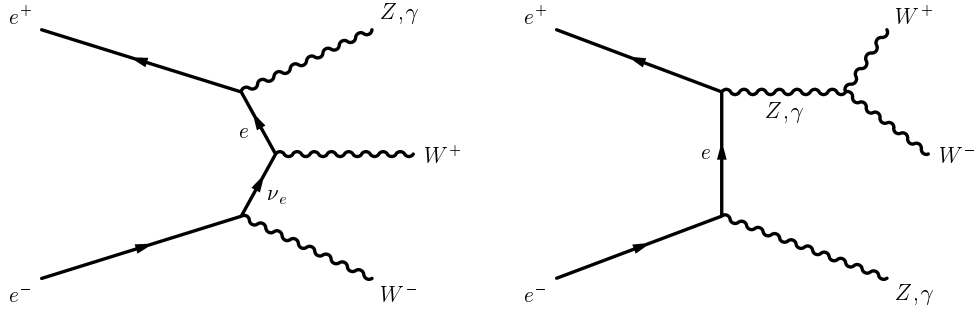


Figure 8.6: Two diagrams as examples for 6-fermion final state processes in the Standard Model.

	run: 110614 evt: 10043	run: 112557 evt: 2752
energy of muon	33.1 GeV	40.3 GeV
missing energy	43.5 GeV	55.0 GeV
mass of on-shell W^+	74.1 GeV	91.4 GeV
mass of on-shell Z^0	90.6 GeV	89.8 GeV
mass of off-shell W^-	35.2 GeV	9.2 GeV
mass of Higgs boson	113.1 GeV	105.8 GeV

This observation was found to be compatible with Standard Model processes leading to 6-fermion final states. Unfortunately no simulation samples were available to be tested with the analysis chain. A MC generator providing the possibility to generate these processes exists only since recently: LUSIFER[DR02]. Such processes are believed to form an irreducible background to searches for bosonic Higgs decays, since the topological signature is expected to be very signal-like (see Fig. 8.6).

Since no simulation samples were available, an estimate for the amount of events expected in each of the four main channels important to the bosonic Higgs decay $H \rightarrow W^+W^-$ was performed using LUSIFER:

\sqrt{s} [GeV]	$HZ \rightarrow q\bar{q}q\bar{q}q\bar{q}$		$HZ \rightarrow q\bar{q}q\bar{q}l\nu_l$		$HZ \rightarrow q\bar{q}q\bar{q}\nu\bar{\nu}$	
	σ	events	σ	events	σ	events
205.0	0.47 fb	0.04	27.28 fb	4.06	0.75 fb	0.06
206.5	0.50 fb	0.07	27.41 fb	7.72	0.73 fb	0.10

One clearly sees, that only in case of the leptonic channel a seizable amount of events is expected. This is due to the huge amount of Feynman graphs contributing (about 5000) to this final state. If one takes into account, that due to the signal-likeness of such events the efficiency will be similar to the 40 % signal efficiency, the total amount of expected events for this analysis is reduced to **2.4** events. This number confirms, that two events coming from 6-fermion final

state Standard Model background processes are indeed expected for the channel $HZ \rightarrow q\bar{q} l\nu_l(q\bar{q})^*$. Consequently these two events were judged as background contribution.

8.5 Channel with off-shell W decaying leptonically

The second Higgs channel analysed in this thesis has a significant four jets signature accompanied by a low energetic electron or muon, the latter having a high probability of getting lost in one of the high energetic jets. This signature is in general difficult to distinguish from hadronic di-boson decays and hence lead to a higher background contamination compared to the “on-shell” channel analysed in the last section at the same level of signal efficiency.

8.5.1 Selection variables

The final discrimination step was again performed by an iterated discriminant analysis, exploiting the kinematical and topological properties of 12 input variables.

- **energy of the most isolated particle** normalised to \sqrt{s}
- **$\ln y_{34}$** , the logarithm of the distance cut-off value y_{cut} , when an event migrates from three-jets to four-jets using the DURHAM cluster algorithm.
- **$\ln y_{45}$** , the logarithm of the distance cut-off value y_{cut} , when an event migrates from four-jets to five-jets using the DURHAM cluster algorithm.
- **minimum interjet angle** forcing all events to four jets
- **reconstructed Higgs mass** using a kinematic fit with five constraints (energy, momentum and one invariant jet pair mass compatible with m_Z) for a topology with five jets and missing energy/momentum
- **χ^2** resulting from a kinematic fit with six constraints (energy, momentum and two invariant jet pair masses being compatible with m_W) for a topology with 4 jets
- **logarithm of acoplanarity times interjet angle** forcing the event to two jets
- **logarithm of the acolinearity**

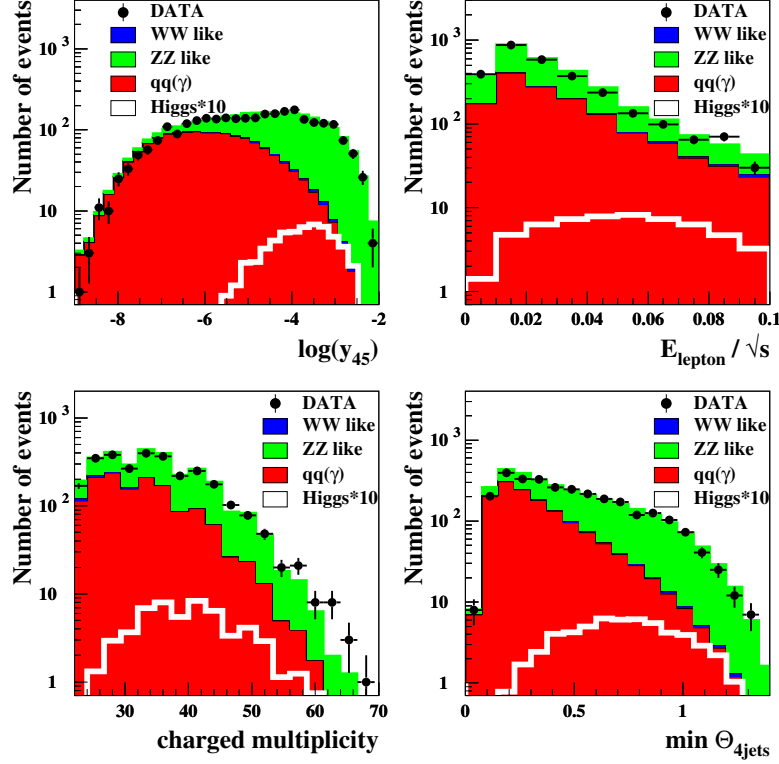


Figure 8.7: ZWW off-shell: The four most discriminant input variables for the discriminant analysis combining 196 – 207 GeV centre-of-mass energies. Illustrated are real data, the expected Higgs signal with a mass of 105 GeV (magnified by a factor 10 for better visualisation) and the three most significant background channels: two-fermion, WW like and ZZ like processes.

- **longitudinal momentum** with respect to the thrust axis, normalised to \sqrt{s}
- **sum of particle energies in a double cone** around the most isolated particle normalised to \sqrt{s}
- **energy of the most energetic lepton** normalised to \sqrt{s}
- **charged multiplicity**

All twelve input variables were found to describe data in a reasonable way at all energies analysed. The distributions of the four most significant input variables

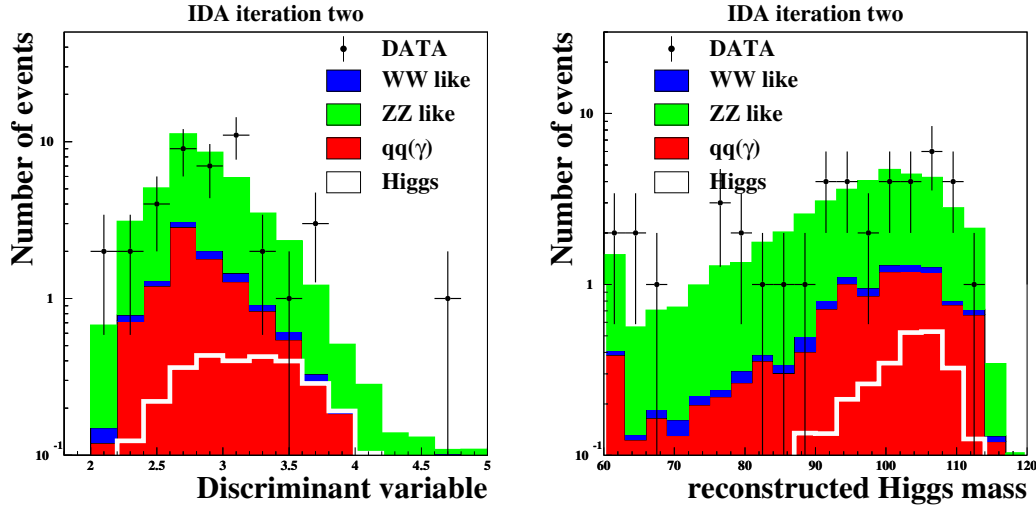


Figure 8.8: The final output distributions (196 GeV - 208 GeV) of the iterated discriminant analysis and the resulting Higgs mass reconstruction. Illustrated are real data, the expected Higgs signal with a simulated mass of 105 GeV and the three most significant background channels: two-fermion, WW like and ZZ like processes.

are shown on Fig. 8.7 after all preselection cuts had been applied. They confirm a good agreement of data and simulation prescription. From these plots one can conclude, that the ZZ like background together with the two-fermion final states processes contribute most at the preselection level of the analysis. The WW like contribution however got nearly completely vetoed. The expected signal region was magnified by a factor of ten for better visualisation.

8.5.2 Iterated discriminant analysis

The twelve input variables defined in the last section were used to perform the two step iterated discriminant analysis in the same way as for the “on-shell” case.

As a working point for both Higgs analyses, an efficiency of 40 % was chosen. The resulting IDA distribution can be seen on the left hand side of Fig. 8.8, together with the reconstructed Higgs mass on the right hand side.

Both distributions show a reasonable agreement between data and the simulated background expectation. The background composition at the final level of the analysis is similar to what was observed at preselection level: ZZ like and two-fermion final state processes dominate the picture with basically no contribution from WW like channels. Both distributions do not show an excess in the corresponding signal regions and consequently there is not hint to a bosonically

decaying Higgs boson in this channel.

8.6 Systematic errors

For both Higgs channels analysed in this thesis, four main sources of systematic errors were taken into account.

8.6.1 Luminosity

The luminosity measurement with DELPHI is believed to contribute with an error of $\pm 0.5\%$

8.6.2 Simulation cross-sections

Theoretical uncertainties in the cross-section calculation for two-fermion and four-fermion final states processes [A⁺00] result in the following systematic errors:

- two-fermion final states: $\pm 2\%$
- WW like processes (mainly CC03): $\pm 2\%$
- ZZ like processes (mainly NC02): $\pm 2\%$

This leads to a global relative uncertainty of $\pm 2\%$ for the simulation prediction by conservatively adding up the full error of each contributing simulation channel.

8.6.3 Description of gluon radiation at parton level

Uncertainties, coming from the choice of the model describing QCD corrections to the primary parton generation by gluon emission build another source for systematic uncertainties. Here typically, the Parton Shower Model (see section 4.1.2) is used. However, multijet events resulting from higher order corrections are known to get better described [Reh00] by the so-called Colour Dipole Model (see section 4.1.2). This model is implemented in ARIADNE [Lön92], providing a colour dipole extension to existing MC generators. Since both Higgs analyses are optimised for a signature with at least four jets, two-fermion final states processes get selected only, if higher order QCD corrections lead to a four jet signature by gluon emission. The Higgs channel with a low energetic lepton signature shows a much higher two-fermion final state background contamination compared to the

other channel with a high energetic lepton. Consequently such a channel is expected to be more sensitive to uncertainties in the modelling of gluon emissions. The impact of using the Colour Dipole Model instead of the standard Parton Shower Model was checked by redoing both analysis channels at 207 GeV using Ariadne for the simulation of two-fermion final state processes and for WW like processes. This results in a $\pm 1.6\%$ effect for the analysis with a high energetic lepton signature and a $\pm 5.3\%$ effect for the other channel, which confirms the expectation.

8.6.4 Energy flow reconstruction

Uncertainties coming from the energy flow through the detector were studied by applying the shaking technique to background MC simulations. The impact on the amount of selected background events can be used to derive the corresponding systematic error contribution. However, the interpretation has to be done with care, since this analysis is optimised to select events with an isolate particle signature.

	on-shell	off-shell
background MC	-5.2 %	+5.6 %

The resulting impact of the shaking is of a similar magnitude for both channels, but with opposite sign. Especially the channel with an on-shell W decaying leptonically is less suitable for the shaking technique due to its high energetic lepton. In order to obtain a conservative error estimate, the effect of the shaking was in this case interpreted as one standard deviation to each side of the value observed.

8.7 Results overview

The results obtained in both channels and the corresponding statistical and systematic errors are summarised on Tab. 8.2. The main uncertainty is clearly coming from statistical errors due to the limited amount of data available. Also systematic uncertainties play some role, especially for the channel with a leptonically decaying off-shell W . Statistical errors on the background simulation turned out to be negligible compared to other error sources and hence confirm the amount of simulated events being sufficiently high.

Comparing systematic and statistical errors with the amount of expected signal events leads to the conclusion, that both analyses on their own are not sensitive enough to confirm or exclude bosonic Higgs decays. Consequently, the

$ZH \rightarrow ZW^*W \rightarrow q\bar{q}(q\bar{q})^* l_{e,\mu} \bar{\nu}_{e,\mu}$				
\sqrt{s} [GeV]	Lumi [pb^{-1}]	background [$ev. \pm stat. \pm syst.$]	data [$ev. \pm stat.$]	expected signal
196	75.0	$4.00 \pm 0.11 \pm 0.23$	2 ± 1.41	0.15
200	82.2	$2.82 \pm 0.10 \pm 0.16$	3 ± 1.73	0.09
202	40.4	$1.33 \pm 0.05 \pm 0.08$	3 ± 1.73	0.30
205	72.9	$3.73 \pm 0.10 \pm 0.17$	3 ± 1.73	0.70
207	138.4	$7.56 \pm 0.20 \pm 0.35$	11 ± 3.32	1.35
Sum	408.9	$19.44 \pm 0.27 \pm 0.99$	22 ± 4.69	2.59
$ZH \rightarrow ZWW^* \rightarrow q\bar{q}q\bar{q} (l_{e,\mu} \bar{\nu}_{e,\mu})^*$				
\sqrt{s} [GeV]	Lumi [pb^{-1}]	background [$ev. \pm stat. \pm syst.$]	data [$ev. \pm stat.$]	expected signal
196	75.0	$8.30 \pm 0.18 \pm 0.66$	9 ± 3.00	0.15
200	82.2	$8.20 \pm 0.19 \pm 0.66$	6 ± 2.45	0.09
202	40.4	$3.99 \pm 0.09 \pm 0.32$	4 ± 2.00	0.30
205	72.9	$7.81 \pm 0.17 \pm 0.62$	12 ± 3.46	0.70
207	138.4	$14.59 \pm 0.32 \pm 1.17$	11 ± 3.32	1.35
Sum	408.9	$42.89 \pm 0.46 \pm 3.43$	42 ± 6.48	2.59

Table 8.2: Statistical overview of the results obtained at each energy for both Higgs analyses. As working point, an efficiency of 40 % was chosen. The expected amount of signal events were calculated assuming $m_H = 105$ GeV and a 100 % branching of Higgs to WW .

results from these two channels were merged with two further analyses, studying the following decay signatures:

- fully hadronic final states $Z^0 H \rightarrow Z^0 W^+ W^- \rightarrow q\bar{q}q\bar{q}q\bar{q}$ performed by *Marcel Stanitzki*[Sta03]
- four hadronic jets and missing energy $Z^0 H \rightarrow Z^0 W^+ W^- \rightarrow \nu\bar{\nu}q\bar{q}q\bar{q}$ performed by *Jörgen Dalmau*[Dal03]

Results from all four analyses were combined to derive confidence limits for bosonic Higgs decays, which is discussed in detail in the following section.

8.8 Confidence limits on bosonic Higgs decays

Even if an analysis cannot confirm new physics, the results obtained can still be used to set limits on unknown parameters. In case of the Higgs boson, one is

interested in limits on its mass and its production cross-section. The latter can be deduced from the linear dependency of the event rate on the cross-section.

In order to set a limit, one first needs to know, to what degree of confidence one can confirm a certain hypothesis. Such a measure is called confidence level (CL_H) and it is determined from a suitable test statistics X , constructed to increase monotonically for increasing signal likeness. Suitable variables would be neural net outputs, discriminant analysis outputs or Likelihood ratios. X is distributed according to its pdf³ $f(X|H)$ and corresponds to the probability of finding $X \leq X_{obs}$ given a certain hypothesis H :

$$CL_H = P(X \leq X_{obs}) = \int_0^{X_{obs}} f(X|H) dx \quad (8.1)$$

When searching for a specific effect like Higgs boson decays, one has to deal with two hypothesis: the background hypothesis (b) and the signal hypothesis (s). Since a CL only stands for a probability, there is automatically a risk of misjudging an observation as signal, although it is part of some background process. Such an error is called *error of the first kind* and should be limited to small values in case of a signal observation in data, since it corresponds to making a false discovery. The corresponding case of misidentifying a signal event as background contribution is called *error of the second kind*. The probability of making an error of the second kind is used in absence of a signal observation to set an exclusion limit, by defining a cut probability CL_{cut} :

$$1 - CL_s \geq CL_{cut} \quad (8.2)$$

For this thesis a CL_{cut} of 95 % was chosen. This limits the probability of making an error of the second kind to 5 % and allows to set exclusion limits at 95 % confidence on the Higgs mass.

The determination of CL_s requires knowledge of the signal pdf under the assumption of no background. However, real experiments in high energy physics result in background contaminated observations. One possibility to correct data for the presence of background is a simple background subtraction. This method however bears drawbacks especially in the case of small signal rates. The MFLR⁴ method, which is used in this thesis to calculate the Higgs limits, chooses the *modified frequentist* approach to determine (approximately) CL_s :

$$CL_s = \frac{CL_{s+b}}{CL_b} \quad (8.3)$$

This procedure is simply the ratio of the confidence level under the assumption of a *background + signal* hypothesis and the confidence level with respect to a

³probability density function

⁴Modified **F**requentist **L**ikelihood **R**atio

background only hypothesis. Since CL_s is not a confidence level, but a ratio of two confidence levels, equation 8.3 only gives a conservative approximation for CL_s .

A test statistic, which minimises errors of the second kind and hence allows to set optimal exclusion limits is given with the Likelihood Ratio Q (Neyman–Pearson lemma)[Rea97], which consists of the Likelihoods for the signal + background and the background only hypotheses:

$$Q = \frac{\mathcal{L}_{s+b}}{\mathcal{L}_b} \quad (8.4)$$

Given a high enough sample statistics, the pdfs resulting from the Likelihood ratio can be used to form a $\Delta\chi^2$ -distributed test statistics and hence confidence levels can be easily determined. Such a test statistics X is derived from Q in the following way:

$$X = -2 \ln Q \quad (8.5)$$

The Likelihood ratio used for the MFLR approach is constructed from a Poisson probability to observe n_i events per channel taken into account times a weight factor for each event:

$$Q(m_H) = \frac{\prod_{i=1}^{N_{chan}} \frac{e^{-(s_i+b_i)} (s_i+b_i)^{n_i}}{n_i!} \prod_{j=1}^{n_i} \frac{(s_i S_i(m_H, x_j^{dis}) + b_i B_i(x_j^{dis}))}{s_i + b_i}}{\prod_{i=1}^{N_{chan}} \frac{e^{-b_i} b_i^{n_i}}{n_i!} \prod_{j=1}^{n_i} B_i(x_j^{dis})} \quad (8.6)$$

In equation 8.6 N_{chan} is the number of channels taken into account, s_i and b_i represent the signal and background rates per channel, while $S_i(m_H, x_i^{dis})$ and $B_i(x_i^{dis})$ correspond to the value of pdfs per channel of the discriminant variable x_i^{dis} for signal and background respectively. The resulting Likelihood ratio depends on the Higgs mass imposed for the signal. Equation 8.6 can be simplified to

$$Q(m_H) = e^{-s_{tot}} \prod_{i=1}^{N_{chan}} \prod_{j=1}^{n_i} \left(1 + \frac{s_i S_i(m_H, x_j^{dis})}{b_i B_i(x_j^{dis})} \right) \quad (8.7)$$

where s_{tot} is the total signal rate integrated over all channels. In order to determine CL_{s+b} and CL_b from a test statistics X one has two possibilities:

- solving the integral of equation 8.1, which requires knowledge of the analytic form of $f(X|H)$
- making a MC experiment to determine the probability $P(X \leq X_{obs})$ from the fraction of experiments satisfying the condition $X \leq X_{obs}$

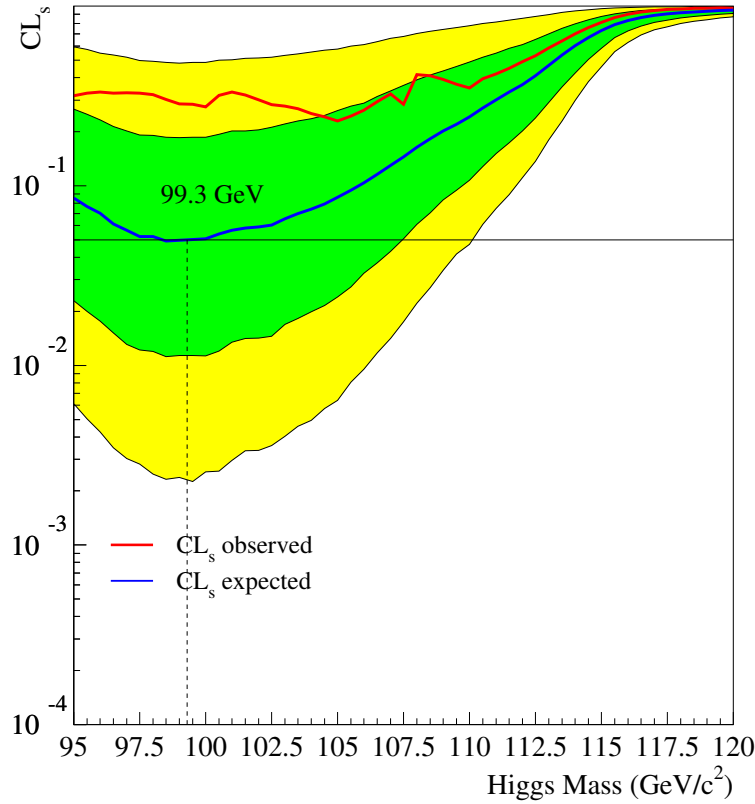


Figure 8.9: Combined limit plot showing CL_s expected and observed. Only an expected limit could be set. The dark grey area corresponds to the 1σ band, while the light grey area represents the 2σ band.

Due to the weight factors, which depend on the form of the used discriminant output variables, it is not possible to find an analytic description of $f(X|H)$. Hence, CL_{s+b} and CL_b are constructed by MC simulations using a Poisson probability for the number of events per channel n_i and simulating a weight for each event based on the pdfs of the discriminant output variables. This procedure is performed for both hypothesis: *signal + background* and *background only* resulting in CL_{s+b} and CL_b respectively.

It is shown in [Rea97], that from equation 8.7 one can deduce the classical “counting experiment”, which is the method described in the PDG for the determination of CL_s . However, the counting experiment approach does not take into account the shape of the discriminant variable and is hence very sensitive to fluctuations in the non-signal like regions of the discriminant distribution. This is one of its major drawbacks compared to the MFLR method used in this thesis.

8.8.1 Limits on the Higgs mass

Higgs mass limits were derived by requiring $CL_s(m_H)$ to be smaller than 5 %, which was calculated by the MFLR method already introduced. The evolution of expected and observed CL_s with respect to the Higgs mass hypothesis is shown on Fig. 8.9, with the horizontal black line indicating the 5 % cut.

From this plot an expected mass limit of 99.3 GeV can be deduced, but no observed limit was found, due to an excess in data. In order to investigate the source of this excess, the corresponding CL_b plots for each of the four analyses was plotted (see Fig. 8.10). From pure background processes one would expect $CL_b = 0.5$. For the purely hadronic channel and for both leptonic channels the observed CL_b is perfectly compatible with the background only expectation within one standard deviation. However, the analysis searching for events with the Z^0 boson decaying invisibly shows an excess for Higgs masses below 100 GeV and hence prevents the combined observed CL_s from falling below the 5 % cut level.

This effect is fortified by the high expected sensitivity of this channel compared to the other three analyses (see expected CL_s on Fig. 8.11). Clearly, the analysis searching for missing energy and four hadronic jets is most sensitive in the Higgs mass region below 105 GeV.

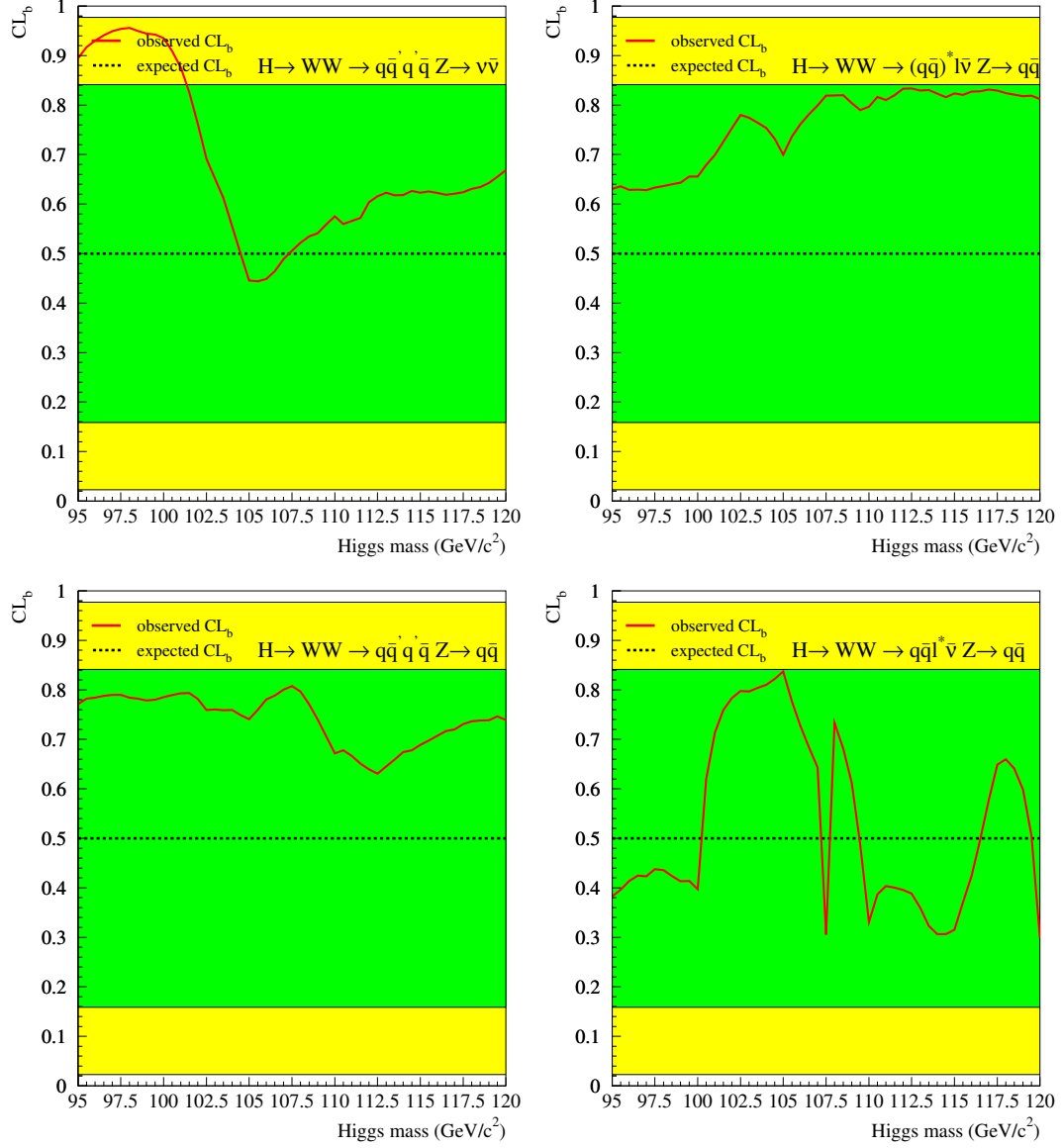


Figure 8.10: CL_b of the four $ZH \rightarrow ZWW$ analyses used for the combination. From upper left to lower right: $q\bar{q}q\bar{q}\nu\bar{\nu}$, $q\bar{q}(q\bar{q})^*l_{e,\mu}\bar{\nu}_{e,\mu}$, $q\bar{q}q\bar{q}q\bar{q}$ and $q\bar{q}q\bar{q}(l_{e,\mu}\bar{\nu}_{e,\mu})^*$. The dark grey area corresponds to the 1σ band, while the light grey area represents the 2σ band.

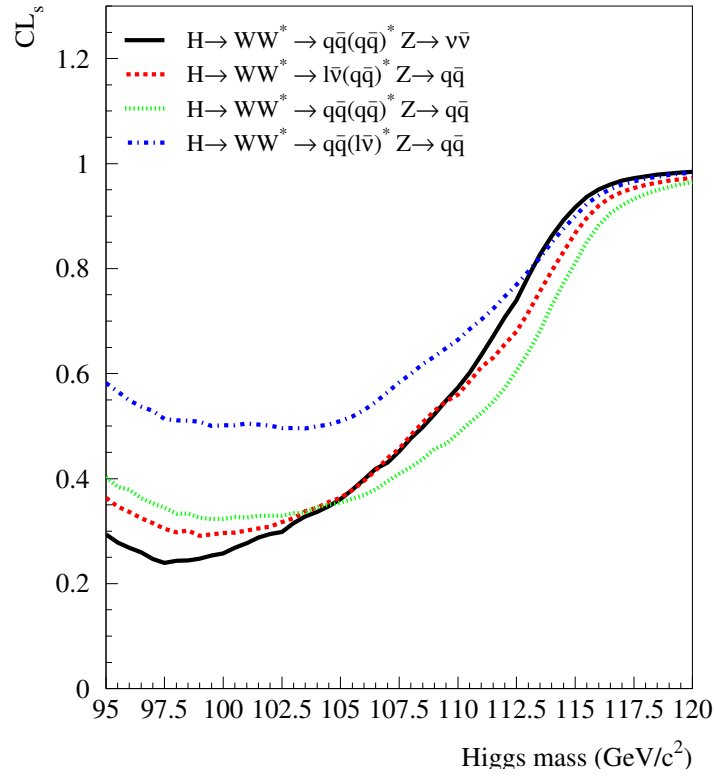


Figure 8.11: Expected CL_s per channel to judge the sensitivity of each analysis.

8.8.2 Cross-section limits

In order to get a more general exclusion, the results obtained can be also interpreted as limit on the production cross-section for $e^+e^- \rightarrow HZ \rightarrow ZWW$. Such a limit allows to exclude extended models with production cross-sections different from the Standard Model.

The left hand side of Fig 8.12 shows the combined expected and observed cross-section limits together with the Standard Model cross-section (assuming a branching $H \rightarrow WW$ of 100 %) as a function of the Higgs mass. The expected limit crosses the Standard Model value at a mass of 99.3 GeV, reflecting the result already obtained from the mass limits. The excess, which prevented an observed mass limit leads to a reduced exclusion area here.

Another representation for cross-section limits is the interpretation as suppression factor with respect to the Standard Model cross-section:

$$\xi = \frac{\sigma_{limit}}{\sigma_{SM}} \quad (8.8)$$

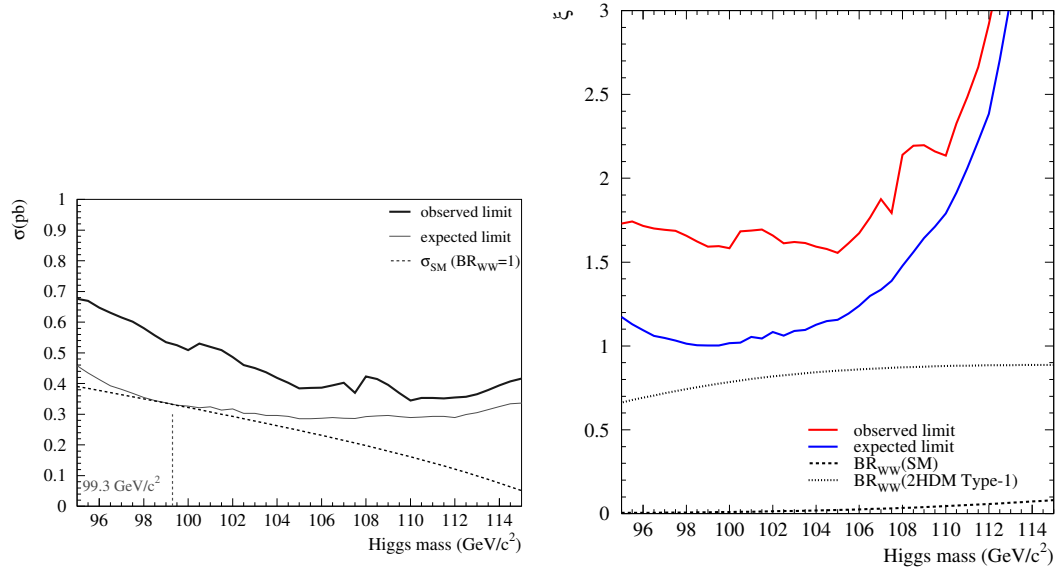


Figure 8.12: Combined cross-section limit (left hand side) and its interpretation as Standard Model suppression factor ξ (right hand side). The area above each limit curve is excluded at 95 % confidence.

A corresponding plot can be seen on the right hand side of Fig 8.12 for expected and observed limits. The expectation using the Standard Model cross-section is split up into two parts: One graph assumes the SM branching of $H \rightarrow WW$, while the second graph assumes a branching favoured by a type I 2HDM model. With the present sensitivity and channel coverage, both scenarios cannot be excluded.

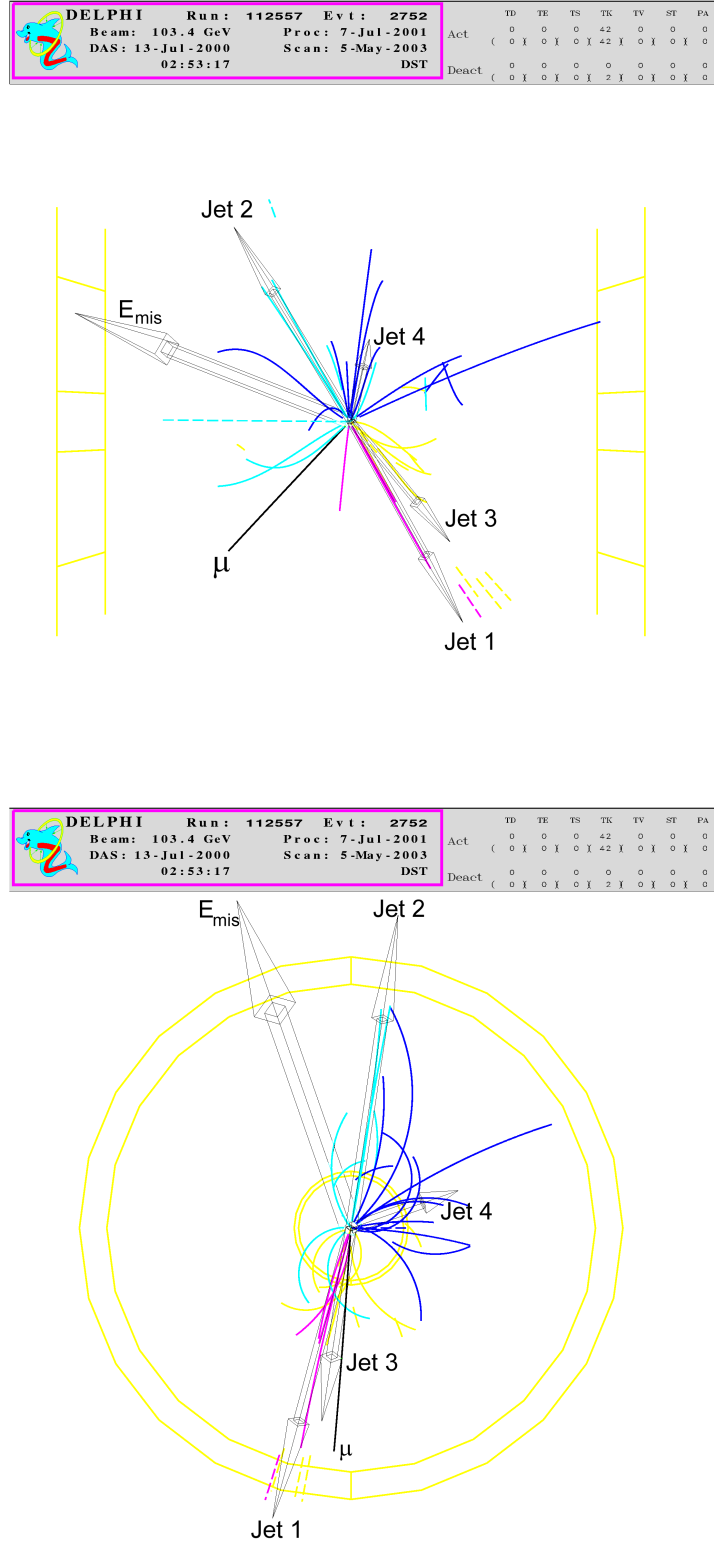


Figure 8.13: The first signal-like candidate selected by the analysis searching for bosonic Higgs decays with a high energetic lepton. The event is characterised by one high energetic lepton candidate, two high energetic jets and two low energetic jets. Such a signature is also compatible with Standard Model 6-fermion final state processes.

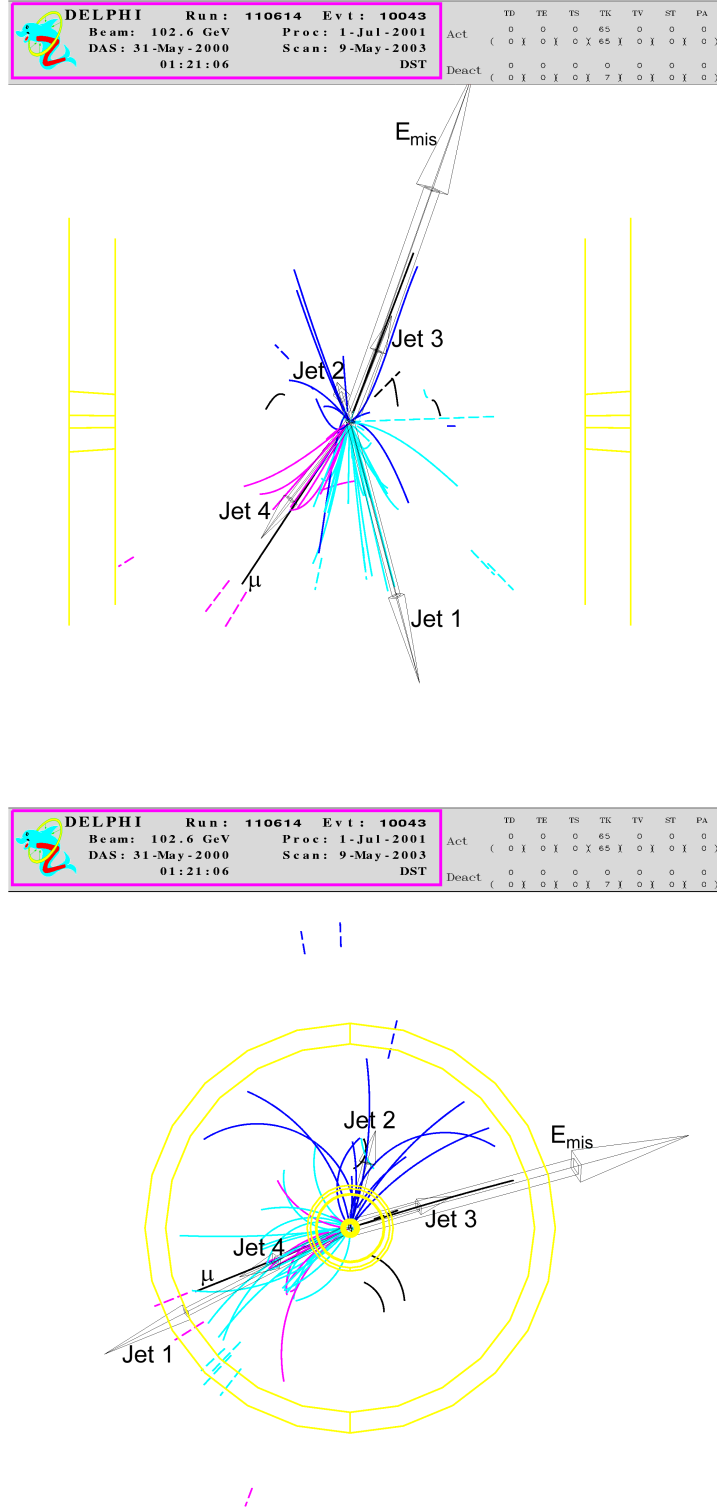


Figure 8.14: The second signal-like candidate selected by the analysis searching for bosonic Higgs decays with a high energetic lepton. The event is characterised by one high energetic lepton candidate, two high energetic jets and two low energetic jets. Such a signature is also compatible with Standard Model 6-fermion final state processes.

Chapter 9

Summary and outlook

In this thesis, three analyses have been carried out: a cross-section measurement of $e^+e^- \rightarrow ZZ$ and a search for bosonic Higgs decays in two different channels. Additionally, a tool to judge systematic uncertainties coming from the energy reconstruction was developed, which provided an important contribution to the systematic error determination of all three analyses.

9.1 Cross-section measurement of doubly resonant Z^0 pairs

In the years from 1997 until the end of 2000 a total luminosity of 665.3 pb^{-1} was accumulated by the DELPHI experiment. This data was taken at centre-of-mass energies above the kinematic threshold for Z^0 boson pair production, providing the possibility to measure the corresponding NC02 cross-sections.

In this thesis, the decay channel $ZZ \rightarrow q\bar{q}\nu\bar{\nu}$ was investigated by performing an iterated discriminant analysis. The distributions of the resulting test statistics was used as input for a binned maximum Likelihood fit of the simulation expectation to data. By combining all energies starting with 183 GeV up to 207 GeV, a total of **173** events was found in data, while **106.7** background events and **66.3** signal events were expected from MC simulations. The combined cross-section resulting from the binned maximum Likelihood fit yielded

$$[0.78 \pm 0.15 \text{ (stat.)} \pm 0.05 \text{ (syst.)}] * \sigma_{\text{SM}}$$

with respect to the Standard Model. This result agrees within 1.4σ with the expectation and points out the limitation of this measurement by statistical errors. The cross-section evolution with energy was also found to be in good agreement

with the Standard Model. A combination of this analysis with the other channels analysed by DELPHI can be found in [DEL03].

9.2 Search for bosonic Higgs decays

The second part of this thesis dealt with a search for bosonically decaying Higgs bosons in two channels with different topological signatures. Such bosonic decays are possible in the Standard Model, but they are also interesting for the type I subset of the 2 Higgs doublet models, since here a complete suppression of all fermionic couplings are possible.

For this analysis data taken in the years from 1999 until the end of 2000 were used, providing a centre-of-mass energy of 196 GeV up to 207 GeV. This corresponds to an integrated luminosity of 408.9 pb^{-1} .

9.2.1 Channel with on-shell W decaying leptonically

The topological signature is characterised by two hard jets, two soft jets and one high energetic lepton accompanied by missing energy and momentum. By combining all energies a total of

22 data events with **19.44** events expected from background estimates

were observed. Among these 22 data events, two signal-like candidates were observed. Both candidates were classified as Standard Model processes with 6-fermion final states, which are expected to contribute **2.4** highly signal-like background events to this channel.

9.2.2 Channel with off-shell W decaying leptonically

The second channel, analysed in the context of bosonic Higgs decays, has a typical four jets signature plus one low energetic electron or muon. Such a topology is much easier to mimic by non-signal processes compared to the on-shell case. Hence performance and signal sensitivity were inferior to the other channel. The combination of all energies yielded a total of

42 data events with **42.89** events expected from background simulations.

This result and also the analysis output distribution shows a perfect agreement between data and the simulation of Standard Model background processes. Hence no signal or signal like events were observed in this channel.

Finally, limits on the Higgs mass and the production cross-section were derived by combining both analyses with two further channels:

- fully hadronic final states $Z^0 H \rightarrow Z^0 W^+ W^- \rightarrow q\bar{q}q\bar{q}q\bar{q}$ by *Marcel Stanitzki*[Sta03],
- four hadronic jets and missing energy $Z^0 H \rightarrow Z^0 W^+ W^- \rightarrow \nu\bar{\nu}q\bar{q}q\bar{q}$ by *Jörgen Dalmau*[Dal03].

This combination resulted in an expected limit of **99.3 GeV** on the Higgs mass assuming Standard Model cross-sections and a branching ratio of 100 % for $H \rightarrow W^+ W^-$. Due to a slight excess in data, observed in the analysis $Z^0 H \rightarrow Z^0 W^+ W^- \rightarrow \nu\bar{\nu}q\bar{q}q\bar{q}$, **no** observed limit was found.

Bibliography

- [A⁺91] P. Arnio et al., *The DELPHI detector at LEP*, Nucl. Instr. and Meth., A303:233, 1991.
- [A⁺96] P. Abreu et al., *Performance of the DELPHI detector*, Nucl. Instr. and Meth., A378:57, 1996.
- [A⁺00] E. Accomando et al., *Four-fermion productions in electron-positron collisions: Reports of the working groups on precision calculations for LEP2 Physics*, Technical Report 2000-009, CERN, 2000.
- [AB97] E. Accomando and A. Ballestrero, *WPHACT 1.0: A program for WW, Higgs and four-fermion physics at e^+e^- colliders*, Comput. Phys. Commun., 99:270–296, 1997.
- [BCG⁺00] D. Bertrand, F. Carena, F. Giacomini, J.-C. Marin, L. Pape and M. Witek, *DELGRA, DELPHI Graphics for Interactive Event Viewing*, 2000.
- [BDK86] F. A. Berends, P. H. Daverveldt and R. Kleiss, *Monte Carlo simulation of two photon processes*, Comput. Phys. Commun., 40, 1986.
- [BiG99] P. S. Bambade and S. M. ì Garcia, 1999, private discussion.
- [BPK95] F. A. Berends, R. Pittau and R. Kleiss, *Excalibur: A Monte Carlo program to evaluate all four fermion processes at LEP-200 and beyond*, Comput. Phys. Commun., 85:437–452, 1995.
- [Cos00] F. Cossutti, 2000, routine to calculate matrix elements from MC four-vectors.
- [Cow98] G. Cowan, *Statistical data analysis*, Oxford University Press, 1998.
- [Dal03] J. Dalmau, *Search for the neutral Higgs boson in the $bb\nu\nu$ final state with DELPHI at LEP*, Ph.D. thesis, Fysikum, Stockholm, 2003, in preparation.

- [dB94] W. de Boer, *Grand unified theories and supersymmetry in particle physics and cosmology*, Prog. Part. Nucl. Phys., 33:201–302, 1994.
- [DEL89] DELPHI Collaboration, *DELPHI event generation and detector simulation – reference manual*, 1989.
- [DEL03] DELPHI Collaboration, *ZZ production in e^+e^- interactions at $\sqrt{s} = 183 - 209$ GeV*, (CERN-EP/2003-009), 2003, to be submitted to Eur.Phys.J.C.
- [DHJ⁺03] J. Dalmau, K. Hultqvist, E. Johansson, C. Mariotti, R. Nicolaidou and V. Ruhlmann-Kleider, 2003, in preparation.
- [DR02] S. Dittmaier and M. Roth, *Lusifer: a LUCid approach to SIZ-FERMion production*, 2002, hep-ph/0206070.
- [DY⁺91] S. C. Dokshitzer, L. Yu et al., *New clustering algorithm for multijet cross sections in e^+e^- annihilation*, Phys. Lett., B269:432–438, 1991.
- [F⁺97] J. Fujimoto et al., *GRC4F v1.1: a four-fermion event generator for e^+e^- collisions*, Comput. Phys. Commun., 100:128–156, 1997.
- [Fei01] M. Feindt, *NeuroBayes – a neural Bayesian estimator for conditional probability densities*, 2001.
- [Fis36] R. A. Fisher, *The use of multiple measurements in taxonomic problems*, Annals Eugen., 7:179–188, 1936.
- [Gla61] S. Glashow, *Partial symmetries of weak interactions*, Nucl. Phys., 22:579, 1961.
- [Gri87] D. J. Griffiths, *Introduction to elementary particles*, John Wiley & Sons, 1987.
- [Heb92] T. Hebbeker, *Tests of quantum chromodynamics in hadronic decays of Z^0 bosons produced in e^+e^- annihilation*, Phys. Rep., 217:69, 1992.
- [Hol93] W. Hollik, *Status of the electroweak standard model*, XVI international symposium on lepton and photon interactions, Ithaca NY, 1993.
- [Jam94] F. James, *Minuit – Function minimization and error analysis*, CERN, 1994.
- [Jan96] P. Janot, *Event generators for discovery physics – HZHA*, Report 96-01, CERN, 1996.

- [JB⁺86] JADE Collaboration, W. Bartel et al., *Experimental studies on multi-jet production in e^+e^- annihilation at PETRA energies*, Zeitr. Phys., C33:23, 1986.
- [JPW97] S. Jadach, W. Placzek and B. F. L. Ward, *BHWIDE 1.00: $O(\alpha)$ YFS exponentiated Monte Carlo for Bhabha scattering at wide angles for LEP1/SLC and LEP2*, Phys. Lett., B390:298–308, 1997.
- [JWW93] S. Jadach, B. Ward and Z. Was, *The Monte Carlo program KORALZ, Version 4.0, for the lepton or quark pair production at LEP/SLC energies*, CERN-TH 7075/93, 1993.
- [JWW00] S. Jadach, B. F. L. Ward and Z. Was, *The precision Monte Carlo event generator KK for two-fermion final states in e^+e^- collisions*, Comput. Phys. Commun., 130:260–325, 2000.
- [KKZ96] W. Kilian, M. Kramer and P. M. Zerwas, *Higgs-strahlung and WW fusion in e^+e^- collisions*, Phys. Lett., B373:135–140, 1996.
- [KM91] N. Kjaer and R. Moeller, *Invariant mass determination in multijet events*, DELPHI Note 91-17 PHYS 88, DELPHI, 1991.
- [Kup98] A. Kupco, *Cluster hadronization in HERWIG 5.9*, 1998, hep-ph/9906412.
- [Lön92] L. Lönnblad, *ARIADNE version 4.08 program and manual*, Comput. Phys. Commun., 71:15, 1992.
- [Lyo86] L. Lyons, *Statistics for nuclear and particle physicists*, Cambridge University Press, 1986.
- [M⁺96] G. Marchesini et al., *HERWIG version 5.9: A Monte Carlo event generator*, 1996, hep-ph/9607393.
- [MB62] G. Möllenstedt and W. Bayh, *Kontinuierliche Phasenverschiebung von Elektronenwellen im kraftfeldfreien Raum durch das magnetische Vektorpotential eines Solenoids*, phys. Blätter, 18:299, 1962.
- [NOT90] S. Nova, A. Olchevski and T. Todorov, *Monte-Carlo event generator for two photon physics*, DELPHI Note 90-35 PROG 152, DELPHI, 1990.
- [Par00] Particle Data Group, *Review of Particle Physics*, volume 3, Springer, 2000.
- [Rea97] A. L. Read, *Optimal statistical analysis of search results based on the Likelihood ratio and its application to the search for the MSM Higgs boson at $\sqrt{s} = 161$ and 172 GeV*, DELPHI Note 97-158 PHYS 737, DELPHI, 1997.

- [Reh00] J. Rehn, *Studie zum QCD Untergrund bei der Higgs Suche am LEP*, Diplomarbeit, Fakultät für Physik, Universität Karlsruhe, <http://www-ekp.physik.uni-karlsruhe.de/pub/web/thesis/rehn.ps.gz>, 2000.
- [Sac94] Y. Sacquin, *Description of the DELPHI DST content*, note 94-161 PROG 210, DELPHI, 1994.
- [Sch93] D. Schaile, *Test of the electroweak theory at LEP*, CERN-Bericht PPE/93-213, CERN, 1993.
- [Sch95] P. Schmüser, *Feynman-Graphen und Eichtheorien für Experimentalphysiker*, Springer, 1995.
- [Sjö83] T. Sjöstrand, *Comp. Phys. Comm.*, 28:227, 1983.
- [Sjö93] T. Sjöstrand, *PYTHIA 5.7 and JETSET 7.4 physics and manual*, CERN-TH.7112/93, 1993.
- [SJW97] W. P. S. Jadach and B. F. L. Ward, *Phys. Rev.*, D56, 1997.
- [Spa97] T. Spasoff, *DELPHI Extended Short DST content v1.06*, note 97-147 PROG 222, DELPHI, 1997.
- [SS97] T. Spasoff and N. Smirnov, *SKELANA - skeleton analysis program*, DELPHI technical manual, 1997.
- [Sta03] M. Stanitzki, *Searches for visible and invisible Higgs decays with the DELPHI detector at LEP2*, Ph.D. thesis, Fakultät für Physik, Universität Karlsruhe, http://www-ekp.physik.uni-karlsruhe.de/pub/web/thesis/phd_stanitzki.ps.gz, 2003.
- [Sva68] N. Svartholm, editor, *Elementary particle theory*, 8th nobel symposium, Almquist and Wiskell, Stockholm, 1968.
- [UA185] UA1 Collaboration, *Evidence for W/Z decay into jets at the CERN p anti- p collider*, 1985, in *Les Arcs, Proceedings, QCD and beyond* 305-310.
- [Vol99] C. F. Vollmer, *Suche nach Higgsbosonen in unsichtbaren Zerfallsenergien am DELPHI-Detektor bei LEP2-Energien*, Diplomarbeit, Fakultät für Physik, Universität Karlsruhe, <http://www-ekp.physik.uni-karlsruhe.de/pub/web/thesis/vollmer.ps.gz>, 1999.
- [Wei67] S. Weinberg, *A model of leptons*, *Phys. Rev. Lett.*, 19:1264–1266, 1967.
- [Wu57] S. Wu, *Experimental test of parity conservation in beta decay*, *Phys. Rev.*, 105:1413, 1957.
- [YM54] C. N. Yang and R. L. Mills, *Phys. Rev.*, 96:191, 1954.

Appendix A

Performance plots ZZ cross-section analysis

On the following pages, the performance plots illustrating the evolution of data and simulation agreement depending on the signal efficiency is shown.

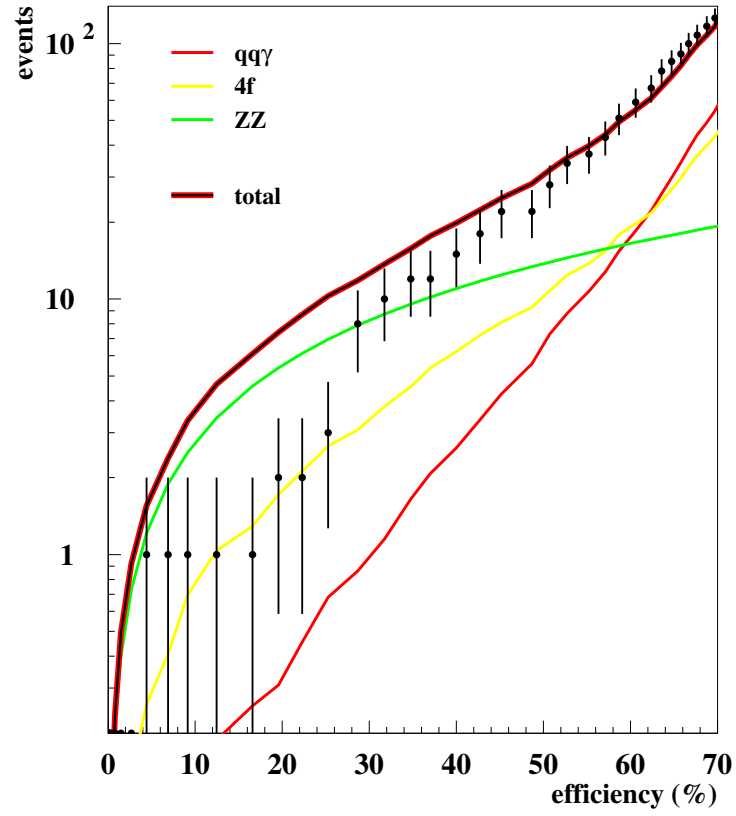
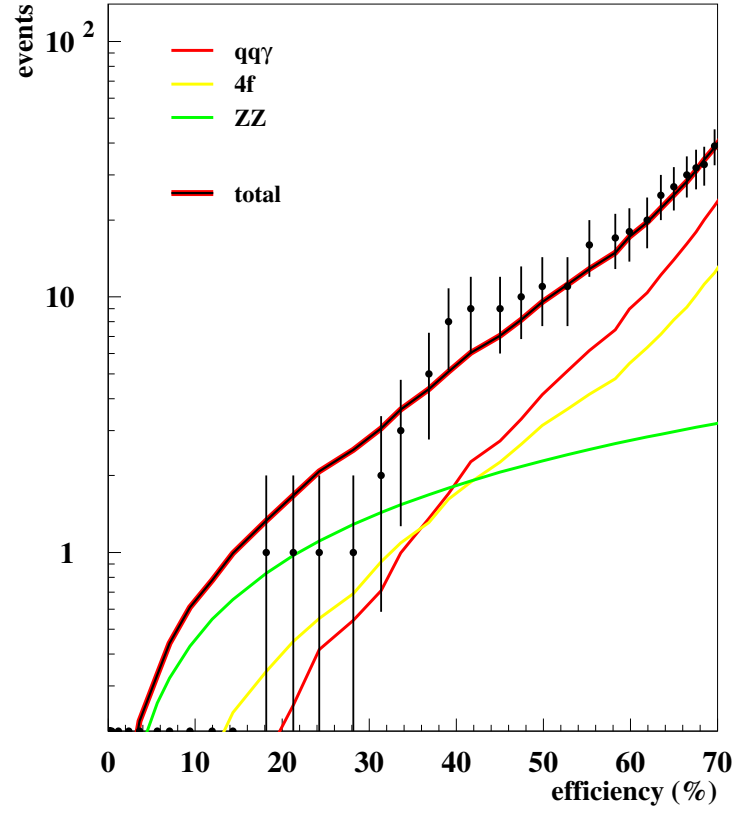


Figure A.1: performance plot at 183 GeV (upper plot) and 186 GeV (lower plot)

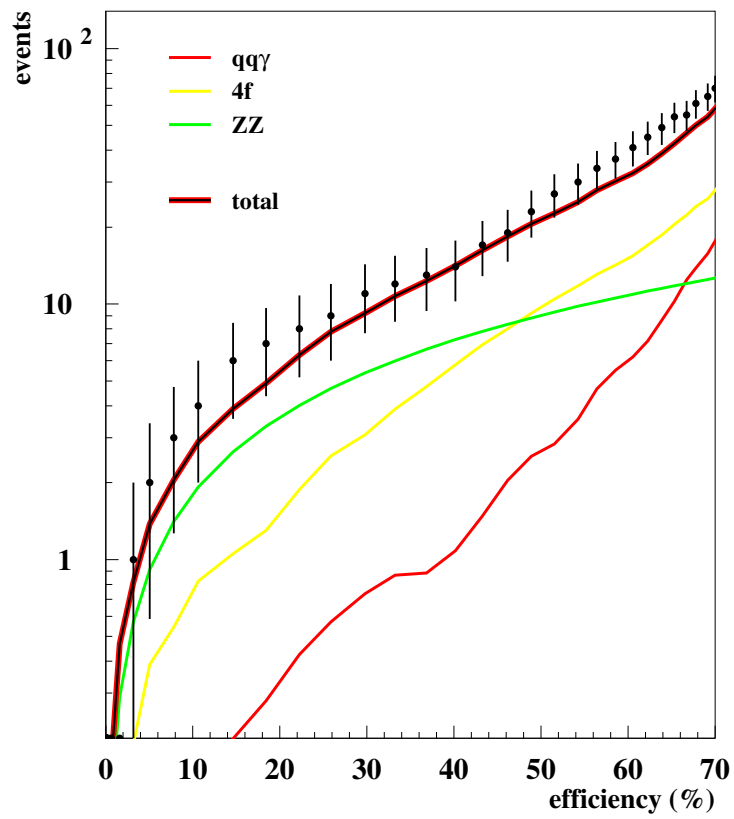
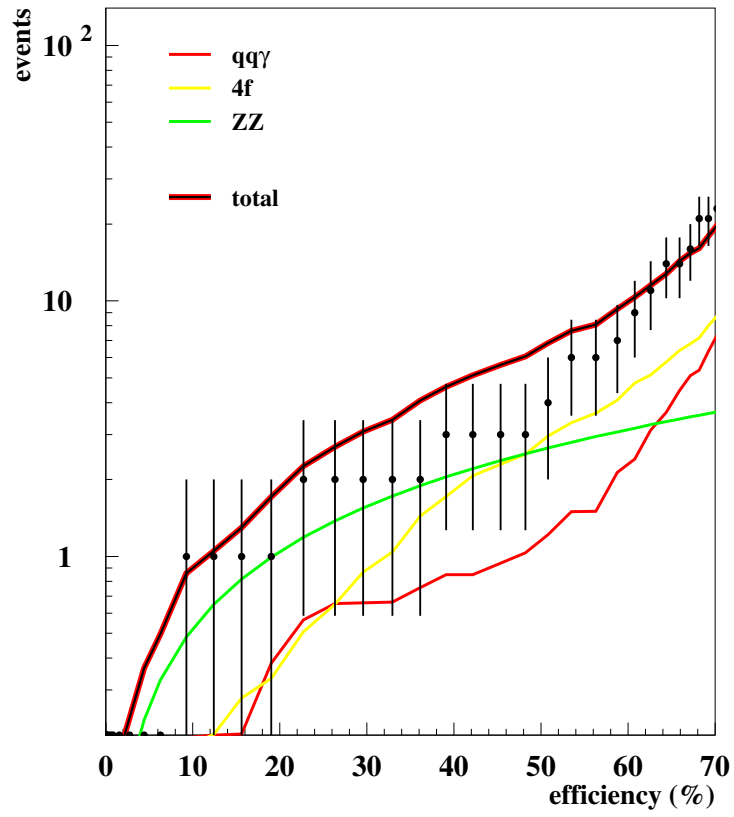


Figure A.2: performance plot at 192 GeV (upper plot) and 196 GeV (lower plot)

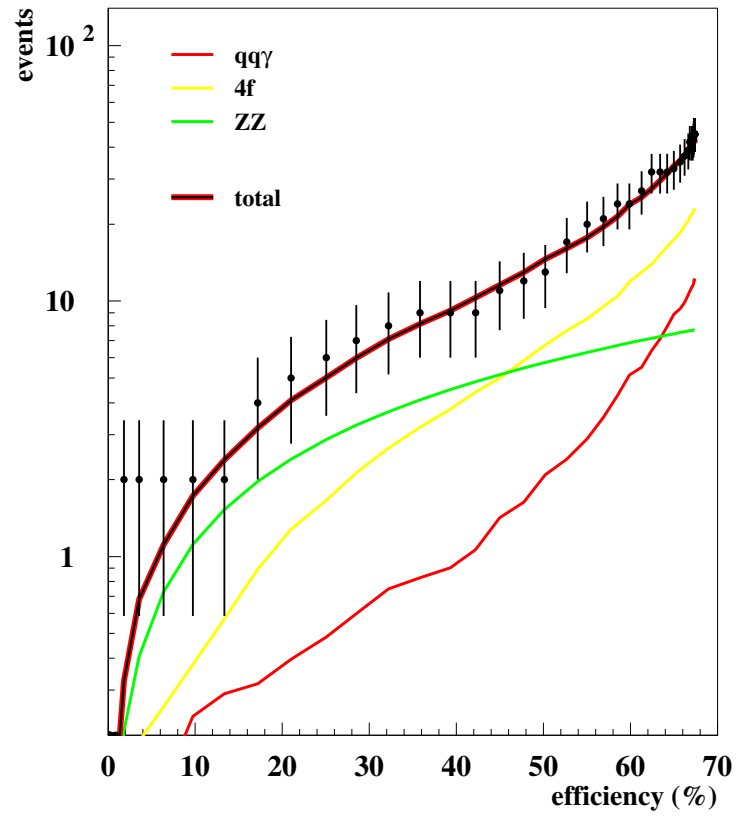
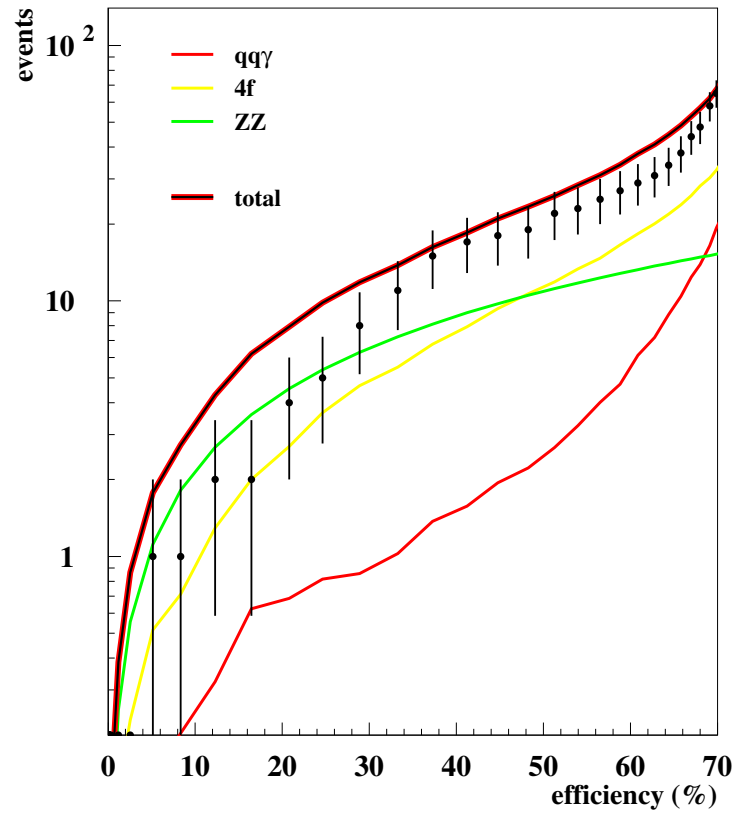


Figure A.3: performance plot at 200 GeV (upper plot) and 202 GeV (lower plot)

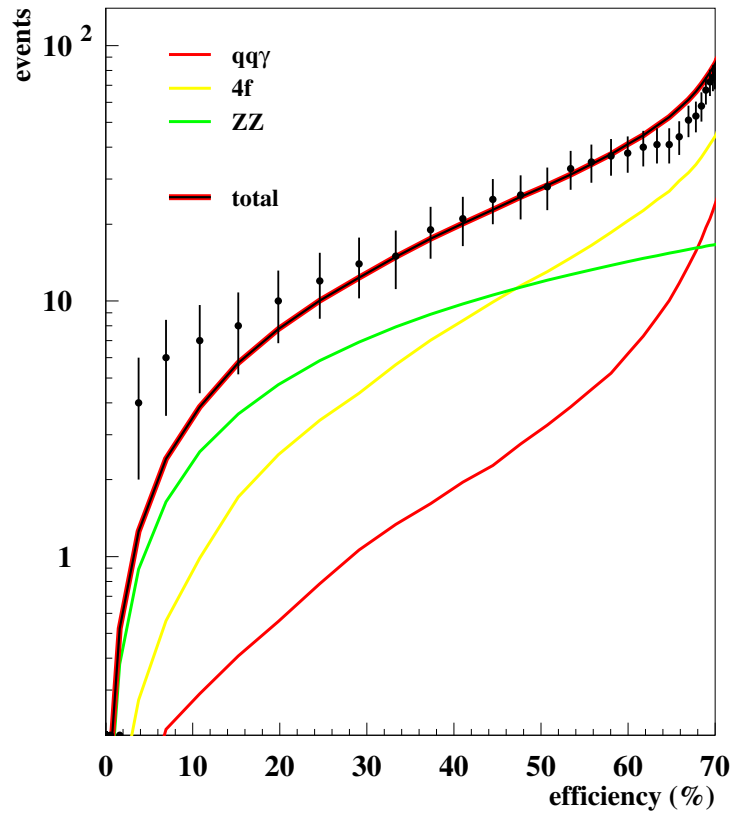
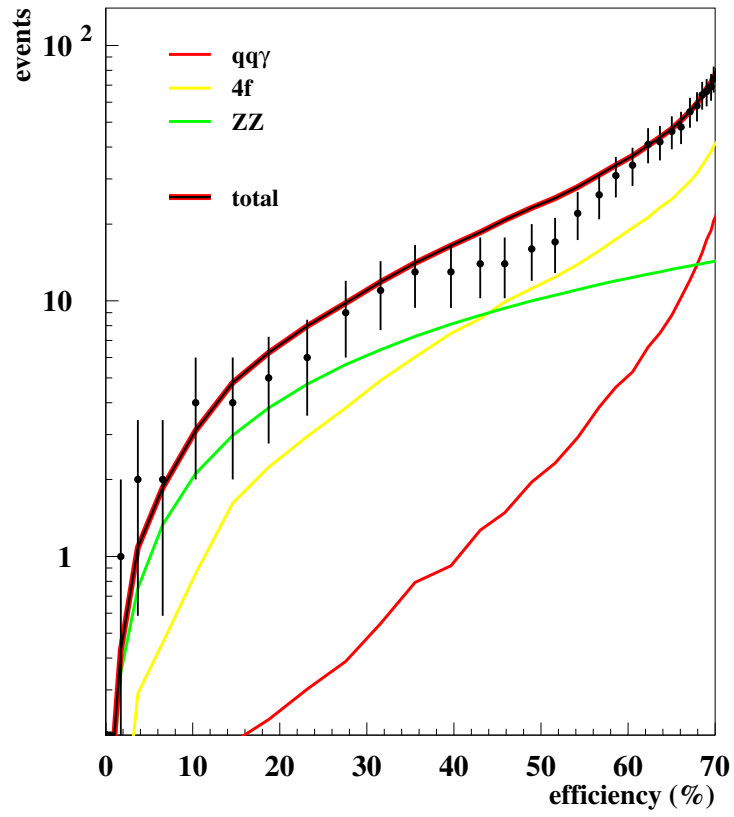


Figure A.4: performance plot at 205 GeV (upper plot) and 207 GeV (lower plot)

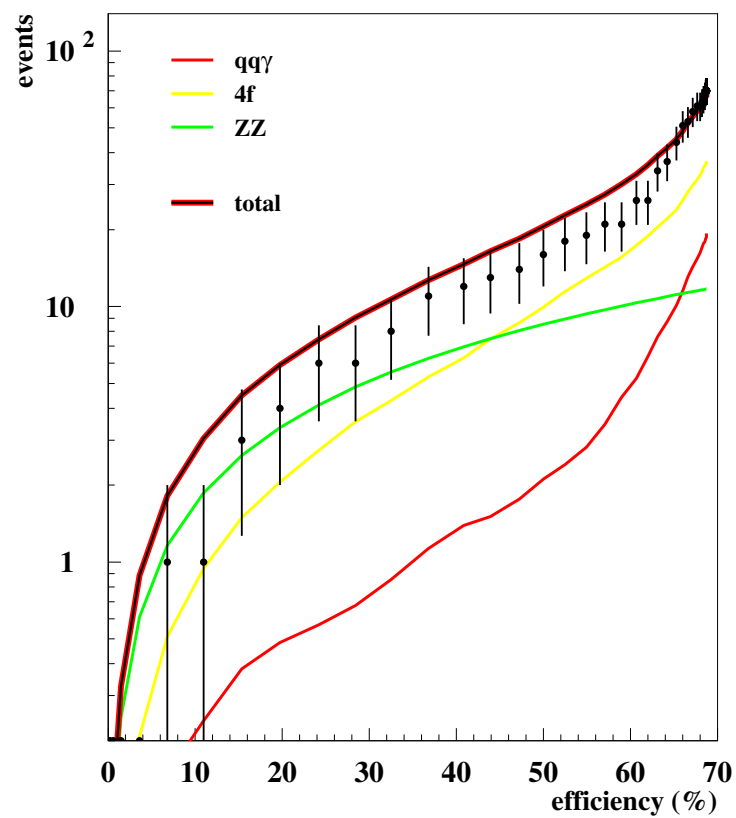


Figure A.5: performance plot at 207 GeV during the period with partially damaged main tracking chamber (S6)

Acknowledgements

I would like to express my gratitude to the following persons, who helped or supported me in one or the other way:

- *Prof. W. de Boer* for giving me the opportunity to stay at CERN for half a year and to participate in the data taking process. I also thank him for giving me the freedom to choose the topic of my thesis, the opportunities to present my work on national and international conferences and for his support and guidance during the last three years.
- *Prof. G. Quast* for many fruitful discussions on physics or computer related topics and for being “Korreferent”.
- *P. Bambade (LAL/Orsay)* for providing an endless stream of ideas and suggestions, leading to very fruitful discussions. Part of the analyses and checks performed in this thesis are a direct result of these discussions.
- *Marcel Stanitzki* for being a good friend and a very reliable colleague since the beginning of our common studies. I also thank him for the great fun we had during this time and for the good teamwork, especially during the last three years.
- *Jörgen Dalmau (Fysikum/Stockholm)* for the fruitful teamwork on the ZWW Higgs analysis and for his hospitality, which made several very enjoyable visits to Stockholm possible.
- *Markus Moch* for very carefully reading the manuscript and for extending the daily coffee breaks....
- *Claudia Lecci* for sharing the office with me and for providing delicious cookies (which spoiled my diet...).
- *Patrick Schemitz* for keeping our computer cluster in perfect shape and for lot's of discussions about computer and Linux related topics.
- *Ulrich Schwickerath* for providing **sjob2**, which simplified the ntuple generation for DELPHI analyses a lot.

- *Christian Haag, Hannes Bol and Levin Jungermann* for the funny time we had during the last eight years of our studies here in Karlsruhe.
- *Frau Weissmann and Frau Haas* for their support in fighting administrative obstacles and German bureaucracy.
- *The so far unnamed rest of the IEKP* for the very nice atmosphere and the birthday cake parties.
- *The Landesgraduiertenförderung Baden-Württemberg, the Graduiertenkolleg “Elementarteilchenphysik an Beschleunigern” and the Graduiertenkolleg “Hochenergiephysik und Teilchenastrophysik”* for financially supporting this thesis by stipends.
- *my parents and grand-parents*, who supported me in many ways during my study. They provided the financial support and guidance necessary to finalise this work.